A wide-field view at single molecules and single particles

Lusitani, Filippo

A mamma e papa'

Filippo Lusitani

A Wide-Field View at Single Molecules and Single Particles

A Wide-Field View at Single Molecules and Single Particles
Filippo Lusitani
PhD thesis
University of Groningen, The Netherlands

Zernike Institute PhD thesis series 2011-20
ISSN 1570-1530
ISBN 978-90-367-5120-9
ISBN 978-90-367-5121-6 (digital version)

University of Groningen
Zernike Institute
for Advanced Materials

The work described in this thesis was performed in Optical Condensed Matter Physics research group of the Zernike Institute for Advanced Materials at the University of Groningen in the Netherlands.

RIJKSUNIVERSITEIT GRONINGEN

A Wide-Field View at Single Molecules and Single Particles

Proefschrift

ter verkrijging van het doctoraat in de
Wiskunde en Natuurwetenschappen
aan de Rijksuniversiteit Groningen
op gezag van de
Rector Magnificus, dr. E. Sterken,
in het openbaar te verdedigen op
vrijdag 21 oktober 2011
om 12:45 uur

door

Filippo Lusitani

geboren op 9 maart 1975
te Piacenza, Italië

Promotor:	Prof.dr.ir. P.H.M. van Loosdrecht
Copromotor:	Dr. M.S. Pchenitchnikov
Beoordelingscommissie:	Prof. dr. A.M. van Oijen Prof. dr. J. Hofkens Prof. dr. J.T.M. de Hosson

Chapter 1
Introduction

1.1 Prologue

The intimate relationship between technological innovation and scientific research is a reciprocal one. Technological progress provides modern science the necessary tools to look beyond the current horizon. In return, science yields new insights and principles which are applied to advance current technology. Modern Fluorescence Microscopy is a prime example of this symbiotic relationship between science and technology. Over the past two decades technological developments have extended the sensitivity of optical microscopy down to the single molecule level[1] leading to many breakthroughs in biology[2-4], chemistry[5, 6], and materials science[7, 8], which, in turn has led[9] and will lead to new technological innovations. The work presented in this thesis relies on the technological innovations in fluorescent microscopy techniques and aims to even add a modest contribution to this development as well. The advance of science and technology often generates new interest into "well-known" phenomena. One example of this process is the random motion small particles, for instance a suspension, undergo as a result of the frequent collisions between the particles and the suspending medium (Brownian motion). This type of motion plays a crucial role in our efforts to control the motion of nanoparticles, as will be discussed in this thesis (see chapter 3). Another example is the response function of an optical microscope, the so-called point spread function. With the current resolution of fluorescent microscopy it is nowadays possible to reach a spatial resolution better than the Abbe limit[10, 11] and, beyond that, even determine the orientation of the emitting molecule being imaged (see chapter 5). Additionally, photophysical properties of single molecules are exploited to unravel long controversial issues in biology (see chapter 4).

The remainder of this introduction will introduce some relevant aspects of the field of microscopy and put the work presented in the various chapters of this thesis into a historical perspective.

1.2 Microscopy and contents of the thesis: links between past and present

What is microscopy and which are its applications? Most probably an entire book will be required to answer this question. An optical microscope is fundamentally an array of one or more lenses designed to achieve a magnified image of small objects; this holds for the early microscopes as well as for the modern ones. The very first microscopes, by the Dutch spectacles maker Zacharias Janssen (1595) and later by Galileo Galilei (1623)[12], consist mainly of a single metallic tube with 2 or more lenses. The very name microscope comes from the description of Galileo's instrument by his fellow academy member Giovanni Faber. Literary microscope means "to look at the small". Nowadays, a modern high numerical aperture objective (as used in this thesis), though similar in the concept, possesses a much more complicated structure incorporating more elaborated optical elements. Still, the basic idea is the same.

However, plain magnification of the object under investigation is not enough. One other important ingredient is the enhancement of the contrast between the background and the object under investigation. An elegant method to enhance the contrast, phase contrast microscopy[13, 14], was proposed by the Dutch physicist Frits Zernike. It exploits the interference between light passed through the specimen of interest and a reference. The larger the phase shift between these, the larger is the amplitude of the interference and thus of the contrast. Zernike was awarded the Nobel prize in 1953 for the invention and development of this technique.

Where Zernike made use of the phase of the light to enhance the contrast, a different route was taken by Albert Coons[15, 16], who attacked the contrast problem through strong enhancement of the amplitude of the light coming from the object making use of fluorescent sources. This work can be marked as the birth of fluorescence microscopy. Fluorescence microscopy produces images with bright objects and dark background contrary to the classical bright field microscope where the objects are dark and the background is bright. The essence of modern fluorescence microscopy is introduced and discussed in chapter 2 together with a detailed characterization of the various constituents of a modern set up. It also addresses the software needed for the proper analysis of the digital images presented throughout.

Certainly, the developments in microscopy during 4 centuries are enormous and some of the achieved results surely can be listed among the breakthroughs of science. For example, in 1827 the botanist Robert Brown first scientifically documented the essence of the erratic motion of small particles in water, named after him: Brownian motion. By observing small pollen grains immersed in water through an optical microscope, he noticed and studied the incessant motion of the imaged particles. Nevertheless, he failed in understanding the causes of the motion; he thought the particles were alive. For more than 80 years the theoretical puzzle of the random motion had been matter of discussion. Only in 1905 Albert Einstein[17]

succeeded to understand this erratic motion, followed one year later by the independent work of the Polish physicist Marian Smoluchowski. The implications concerning the very nature of matter that both scientists highlighted were huge. In fact, the observation of the Brownian motion obtained by the use of a microscope is the very first experimental evidence of the corpuscular nature of matter. The collisions with the molecules of the liquid, in which the suspended particles are diffusing, are the only cause of the motion. Today it might sound trivial, but at the beginning of the 20th century the atomistic hypothesis of the discrete essence of matter was far from being universally accepted.

Brownian motion in particular, even if fully characterized experimentally and theoretically long time ago, still holds a certain interest for the scientific community, especially in the field of nanotechnology. One of the more interesting challenges for nanotechnology is the design and implementation of the so-called "lab-on-a-chip" concept. A successful implementation of this concept needs control over transport of matter on the nano-scale, usually in a liquid environment. At the microscale there are already several examples of self-propelling systems which have been shown to be effective transporters[18-20]. In this thesis (chapter 3) we will investigate if these propelling mechanisms, successful at the microscale, are also able to propel objects at the nanoscale. The motion of nanoparticles performing the same processes driving the self-propulsion at the microscale is tracked and analyzed to reveal possible deviations from the purely Brownian diffusion. Single particle tracking technique is applied to investigate the laws describing the motion of particles. The same fact that the motion of particles of ~ 100 nm size diffusing in a liquid environment can be tracked and analyzed at the single particle level proves the achieved sensitivity of the microscopy technique.

The very example represented by the Brownian motion offers the possibility to introduce the field in which, arguably, microscopy has shown its greatest impact. In fact, the experiment of Brown concerning the observation of pollen grains diffusing in water was performed and focused on a purely biological sample. Biology has strongly benefitted from the remarkable achievements in optical microscopy. It enabled scientists to unravel the complex structure of biological systems in great detail. In 1665 Robert Hooke in his publication "Micrographia"[21] coins the term cells to name structures he observed in cork bark. The implications of the observation and documentation of living cells for biology parallel the implications of the discovery of the corpuscular nature of matter for physics. The intimate relationship existing between biology and optical microscopy is, if possible, even stronger in the 21st century. The non-invasive nature of light makes microscopy the tool of choice for the study of *in vivo* biological systems and their inner constituents; nowadays even at the subcellular level.

As mentioned at the beginning, throughout the centuries the improvements to the technique has provided scientists with more powerful tools. The most recent breakthrough is without doubt the achievement of single molecule sensitivity. It enables scientists to investigate biological systems at a level of detail considered

unthinkable only 20 years ago. The single molecule sensitivity has sparked an immense amount of new research in biology, and often gave answers to strongly debated and controversial issues.

A living cell needs to perform many functions that are necessary for life. One of them deals with the secretion or the insertion of proteins from and into the cell membrane. The importance of the matter is highlighted by the fact that in all the three domains of life the function is achieved by the use of analogue protein conducting channels. In bacteria, the secretion and membrane insertion of protein from the cytoplasm of the cell occurs through the protein conducting channel named SecYEG. Though widely investigated, the issue still lacks a certain and final answer to a long lasting question: how many SecYEG proteins are required for the translocation of a single protein? Nowadays two major models are discussed in literature; the first one says that only a single SecYEG is necessary and the second one argues that two are required. Chapter 4 presents the first steps of a new approach that is expected to eventually resolve this issue. The proposed idea is based on a well-known photophysical process, named photobleaching, occurring in fluorescence emitters. The emission of an ensemble of fluorescent emitters decays exponentially with time upon constant excitation. If only a few molecules are involved than this exponential decay will proceed in a quantized manner. The time dependence of the emission intensity will show a photobleaching event as a step-like decrease in the emission, eventually down to zero emission. Therefore, by labeling each SecYEG protein with a single fluorescent molecules (daily work in today's laboratories) and following the time dependence of the emission it becomes possible to literary count the number of SecYEG molecules in the ensemble.

The above example shows how the exploitation of new features concerning the photophysical properties of single emitting molecules allows development of new approaches in the investigation of matter. This is possible thanks to the achieved single molecule sensitivity. But this is not the end of the story. The direct observation of a single emitter light source one or two orders of magnitude smaller than the emitted wavelength yields new possibilities to extract information on the emitting source. In 1835 George Biddell Airy[22] solved the diffraction equation describing the distribution of light transmitted through a circular aperture. It is the mathematical definition of the so-called Point Spread Function (PSF) that determines the ultimate resolving power of a microscope. The image, following the circular geometry of the aperture, consists of a central disk, named Airy disk, surrounded by secondary rings (see chapter 5). A few years later (1860's) Ernst Abbe formulated the sine equation (Abbe's sine equation) representing a breakthrough for the design of microscopes. This is a perfect example on how scientific discoveries and technological improvements are strictly connected and influencing each other. Abbe is also known for the experimental resolution limit of optical imaging, called Abbe's limit (1874)[23]: The resolution of the microscope is proportional to the wavelength of the light emitted by the source and inversely proportional to the extent of the aperture, and coincides with the Airy disk.

The concept of resolution of a microscope is treated more in detail in chapter 5; here it is enough to mention that a microscope cannot provide details smaller than its resolution. It is a fundamental limit. Still, the ever growing demands in terms of details in the study of systems at small length scales have challenged and pushed scientists to bypass Abbe's limit. In fact, using the *a priori* knowledge of the mathematical description of the photons distributed in the Airy disk allows to determine the position of the emitting source with two orders of magnitude higher accuracy, at least as long as the imaged source is not overlapping with another source. In chapter 5, the position of fluorescent beads is measured with 1 nm accuracy; in the case of single fluorescent molecule the accuracy achieved is about 2 nm (due to lower signal-to-noise ratio).

The growing demands in terms of level of detail and achievable information have pushed the development of the aforementioned determination of the position of the light source with few nanometer accuracy. At the same time one is also interested in the orientation of single molecules. This orientation is relevant for physical processes like Förster Resonant Energy Transfer (FRET), which efficiency is strongly dependent not only to the inverse of the donor/acceptor distance (it is actually the distance to the power six), but also to the relative orientation of the two dipoles. To determine this orientation one can use the fact that single light absorbing/emitting molecule are in fact dipole emitters. The classical theory of Airy did not take this into account in any detail. However, the dipole nature is easily observed by looking at a slightly (~ 1μm) defocused image which allows extraction of the orientation of the emitting dipoles[24]. A disadvantage of defocusing is that the accuracy in the position of the molecules decreases substantially. Chapter 5 discusses a novel method to resolve both the position of the emitter with a high accuracy as well as the orientation of the emitter. The approach used is based on the theoretical work presented in 1959 by Richards and Wolf[25], who solved the same diffraction problem as Airy, this time taking the effects of polarization more properly into account, to arrive at an elliptical PSF. The high resolution images presented in the final chapter of this thesis show that one can indeed use the elliptical shape of the PSF to determine both the position and orientation of a single molecule from a single image.

Bibliography

1. Nie S; Zare R.N. *Annu. Rev. Biophys. Biomol. Struct.* **1997,** 26, 567 - 596.
2. B. Schuler; E. A. Lipman; W. A. Eaton. *Nature* **2002,** 419, 747-747.
3. H. Noji; R. Yasuda; M. Yoshida; K. Kinosita Jr. *Nature* **1997,** 386, 299-302.
4. J.B. Lee; R.K. Hite; S.M. Hamdan; X.S. Xie; C.C. Richardson; A.M. van Oijen. *Nature* **2006,** 439, 621-624.
5. K. Blank; G. De Cremer; J. Hofkens. *Biotech. J.* **2009,** 4, 465-479.

6. G. De Cremer; Y. Antoku; M. B. J. Roeffaers; M. Sliwa; J. Van Noyen; S. Smout; J. Hofkens; D. E. De Vos; B. F. Sels; T. Vosch. *Angew. Chem. Int. Ed.* **2008,** 47, 2813-2816.
7. P. Dedecker; B. Muls; A. Deres; H. Uji-i; J. Hotta; M. Sliwa; J.-P. Soumillion; K. Müllen; J. Enderlein; Hofkens, J. *Advanced Materials* **2009,** 21, (10-11), 1079-1090.
8. M. B.J. Roeffaers; R. Ameloot; M. Baruah; H. Uji-I; M. Bulut; G. De Cremer; U. Müller; P. A. Jacobs; J. Hofkens; B. F. Sels; Vos, D. E. D. *J. Am. Chem. Soc.* **2008,** 130, 5763-5772.
9. Dedecker P.; Hofkens J.; et. al. *J. Am. Chem. Soc.* **2007,** 129, 16132 - 16141.
10. A. Yildiz; J. N. Forkey ; S. A. McKinney; T. Ha; Y. E. Goldman; Selvin, P. R. *Science* **2003,** 300, 2061-2065.
11. E. Betzig; et. al. *Science* **2006,** 313, 1642-1645.
12. Drake; Stillman, *Galileo at Work*. University of Chicago Press: Chicago, 1978.
13. F. Zernike. *Physica* **1942,** 9, 974 - 986.
14. F. Zernike. *Physica* **1942,** 9, 686 - 698.
15. A. H. Coons; M. H. Kaplan. *J. Exp. MEd.* **1950,** 91, 1 - 13.
16. A. H. Coons; Kaplan., M. H. *Fed Proc* **1951,** 10, 558 - 559.
17. A. Einstein. *Ann. Phys.* **1905,** 17, 549 - 560.
18. Paxton, W. F.; Kistler, K. C.; Olmeda, C. C.; Sen, A.; St Angelo, S. K.; Cao, Y. Y.; Mallouk, T. E.; Lammert, P. E.; Crespi, V. H. *J. Am. Chem. Soc.* **2004,** 126, 13424-13431.
19. Sololev A. A.; Schmidt O. G.; et. al. *Small* **2009,** 5, (14), 1688 - 1692.
20. Heureux, N.; Lusitani, F.; Browne, W. R.; Pshenichnikov, M. S.; van Loosdrecht, P. H. M.; Feringa, B. L. *Small* **2008,** 4, (4), 476-480.
21. R. Hooke, *Micrographia: or, Some physiological description of minute bodies made by magnifying glasses*. J. Martyn and J. Allestry: London, 1665.
22. G. B. Airy. *Trans. Cambr. Philos. Soc.* **1835,** 5, 283 - 291.
23. E. Abbe. *Proc. Bris. Nat. Soc.* **1874,** 1, 200 - 261.
24. Bohmer M.; Enderlein J. *J. Opt. Soc. Am. B* **2003,** 20, (3), 554 - 559.
25. Richards B.; Wolf E. *Proc. Roy. Soc. Lon.* **1959,** 253, (1274), 358 - 379.

Chapter 2
Wide Field Fluorescence Microscopy

This chapter is devoted to the description of the experimental setup and the various applications of the Wide Field Fluorescence Microscopy technique as used throughout this thesis.

A short introduction sketches the principles of single molecule microscopy and its applications, in particular concerning the wide field configuration. Applications such as super resolution imaging, single particle tracking, polarization-dependent fluorescence studies and quantitative analysis at the single molecule level are introduced and discussed. Experimental results, discussed in detail in the various other chapters in this thesis, will be used to illustrate this introductory part.

2.1 History of fluorescence microscopy and single molecule techniques

The obvious purpose of a microscope is to make small things appear larger. Pure magnification, however, is not the only demand of microscopy. Access to the world of small length scales usually also requires an enhancement of the contrast between the object and the background. Bright field microscopy presents the simplest and oldest illumination technique. White light is used to illuminate the sample which absorption decreases the transmitted signal generating the contrast. Generally the sample is illuminated from below and observed from above. Images consist of a white and bright background while the imaged objects appear darker. Even if very simple to realize, bright field microscopy is strongly limited by its low contrast when applied to poorly absorbing specimens. This calls for the implementation of new approaches to strongly boost the performance of microscopy techniques.

Unlike bright field microscopy, modern fluorescence microscopy aims at the enhancement of the contrast by imaging bright objects in a dark background. The investigated objects become themselves the source of the optical signal. In 1852 Sir George Stokes[1] observed that some materials were able to emit light at a wavelength red-shifted relative to the excitation wavelength (the Stokes shift). By attaching via chemical bonds (labeling) fluorescent molecules to the systems under investigation, one can have access to a much higher degree of accuracy gaining more detailed images if compared to bright field microscopy. Nowadays the

fluorescent emission, or simply fluorescence, is extensively used in modern microscopy, and the most exploited one in the case of nanosystems.

There are two major aspects which yield high contrast boosting the use of fluorescence in microcopy rather than direct illumination:

1) The red shift between excitation and emission wavelength of a specimen allows to spectrally separate the fluorescent signal from the illumination thereby strongly enhancing the contrast, and hence the signal-to-noise ratio of the image.

2) The object under investigation becomes itself the source of the emitted light. Therefore, one can spectrally separate various parts of a more complex system when labeled with dyes emitting at different wavelengths.

Often materials under investigation are not fluorescent by themselves and therefore they cannot be imaged directly. In order to overcome this problem one may label the objects of interest with fluorescent molecules. The possibility to image a system by labeling it with fluorescent dyes has been adopted already since almost a century[2]. Since then a large progress has been made in both the labeling capabilities as well as in the synthesis of new fluorescent molecules.

The labeling is obtained by chemically attaching selected dye molecules (or fluorophores) to the objects at specific sites. By choosing different fluorescent molecules which absorb and emit at different wavelengths one can then label different parts of a system with different colors enabling simultaneous imaging of the various functional parts[3, 4]. In biological cells one might for instance label a protein with a fluorophore emitting in the red part of the spectrum, and label the DNA inside the nucleus with a green emitting one, thereby yielding a large contrast between different parts of the cell. Enormous is the number of images of sub-cellular systems obtained with fluorescent microscopy; it might be worth just typing on internet fluorescent microscopy and check the beautifully colorful images proposed.

Today a large variety of dyes are commercially available offering a wide range of photo physical and chemical possibilities. The last are of primary importance since the fluorescence emission can be affected (emission spectral shift or quenching) by possible interactions between fluorescent molecules and environment molecules[5]. Besides, chemical properties govern, for instance, the solubility in a specific solution/ environment, i.e. Alexa Fluor organic dyes series are more water soluble then others organic dyes[6]. Additionally, the chemical bonding could differ from system to system[5].

Together with the wide choice of absorption/emission spectra, there has been an enormous progress in the development of labeling techniques. Labeling single proteins, single DNA chains, a single base pair in a DNA chain and even single molecules are now routine procedures in the fluorescent microscopy field. Apart from designing dye molecules with specific wavelengths, great effort has also been spent to enhance the luminescent efficiency as well as in the designing more

versatile emitters[7, 8]. One of the major breakthroughs, in particular for the field of biology, was the discovery and development of the green fluorescent proteins (GFP) for which Osamu Shimomura, Martin Chalfie and Roger Tsien received the Nobel Prize in Chemestry in 2008[9]. All these developments have broadened the successful application of fluorescent microscopy into a large variety of disciplines, including biology[10-12], chemistry[13, 14], medicine[15-17], material science[18, 19] and physics[20-22].

One of the most important properties of the luminescent molecules is the efficiency with which they emit light after the absorption of a photon. This may be quantified by the so called quantum yield (QY) which is defined as the ratio of the number of emitted photons over the number of the absorbed photons. Non radiative decay events and energy transfer processes with neighbor molecules reduce the intensity of the fluorescent emission thus lowering the QY[5] and the overall brightness. Today several fluorescent molecules are commercially available offering an extremely high brightness (such as Alexa Fluor 488)[23]. The possibility to work with extremely bright molecules together with the developments in CCD (charge coupled device) detectors and laser technology has provided scientists with the tools to perform microscopy down to the level of a single molecule[24-26].

Although other microscopy techniques such as atomic force microscopy (AFM) and scanning tunneling microscopy (STM) offer a resolution down to the atomic scale, often the requirements of these techniques are not compatible (too invasive) with the systems one would like to study, for instance in biological materials. The non invasive use of light to probe systems at the single molecule level of resolution has promoted and propelled the applicability and eventually the performances of fluorescence microscopy. Single molecule microscopy pertains literally the possibility to image single molecule. In a way it is amazing that this is possible since the optical fluorescent signal emitted by a single molecule must be very weak and difficult to detect. In fact it is. As mentioned earlier, great effort has been used to develop fluorescent molecules with high quantum yield. Today are commercially available molecules able to emit such amount of photons per second to be visible with naked eyes. One can observe them directly from the eyepieces of a microscope. This is possible if the laser excitation light is spectrally separated from fluorescence enhancing the contrast between the dark background and the optical signal. Development in optics has made possible to well separate the fluorescence (signal) from the excitation, thus lowering the background (noise) which results in a highly enhanced signal-to-noise ratio (contrast). Besides, the improved capability to gather photons with the use of specific objectives has substantially increased the performance of single molecule microscopy.

Nevertheless, not all fluorescent molecules offer high QY. Here, the breakthrough has been provided by the technological development and the improvements of highly sensitive detectors such as CCD cameras. Today, they are

extensively used in fluorescent microscopy providing sensitivity down to single photon level.

The results obtained in the design of new and more efficient fluorescent molecules and the developments in technology have offered scientists a tool to actually investigate nature at a level unthinkable only 25 years ago. Single molecule fluorescence microscopy not only opened up a previously inaccessible world, but, in a way, also changed our vision on matter. Single molecule studies have highlighted the strongly heterogeneous behavior of molecules. Even if an ensemble of molecules of the same species dissolved in a solution experiences on average the same conditions, at single molecule level the strong interaction with the solvent's molecules differs from molecule to molecule. The interaction of the molecules under investigation with the environment molecules might affect the performance of the molecule substantially[27]. For example, Ref. 27 by Xie and Lu presents a single molecule study on chemical reaction kinetics occurring between cresyl violet molecules and an indium tin oxide (ITO) substrate. The work reveals the physical origin of the multiexponential kinetics of electron transfer in the system is the inhomogeneity of molecular interactions between cresyl molecules and the substrate. Cresyl molecules, though identical to each other, experiences different interactions with the substrate molecules; this leads to the heterogeneous behavior.

Rather than yielding merely the average value of a physical property, the single molecule approach is capable of providing a detailed insight into the distribution of that property, which is often needed for a detailed understanding.

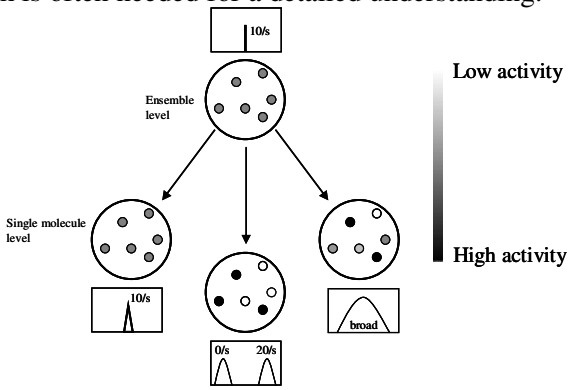

Figure 2.1: Sketch illustrating the limited insight on the activity of a group of molecules offered by bulk measurements. Single molecule approach reveals that the molecules might behave differently[27].

Figure 2.1 sketches the fundamental limitation of the averaged result obtained in bulk measurements if compared to single molecule sensitivity. The average value represents the molecules as working all at the same rate. A single molecule approach, instead, might reveal the heterogeneous behavior of the various

molecules. The molecules might all work at the same rate, as resulting from the bulk experiment, or present broader distribution of values as well as two wholly separated working rates which average coincides with the bulk value.

Apart the aforementioned sensitivity to heterogeneities, single molecule approach offers other advantages: no temporal synchronization requirements, sensitivity to rare events, super-resolution microscopy.

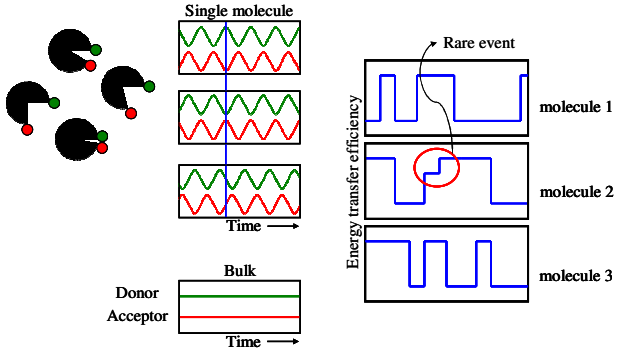

Figure 2.2: Sketches illustrating the mentioned advantages offered by the single molecule sensitivity. On the left, the signal from a donor-acceptor system varies according to its intrinsic dynamics (oscillating signals), while if measured in bulk presents constant average value. On the right, the energy transfer efficiency could unravel rare events.

Figure 2.2 illustrates the advantages offered by single molecule sensitivity. The dynamics of a group of four proteins (black objects) are studied by measuring the intensity of the signal from the donor-acceptor system labeling each protein. If they "open" the signal from the acceptor weakens since the energy transfer process between donor and acceptor depends on the relative distance. The signal is enhanced when the "protein" closes. Even if the "opening" and the "closing" occur with about the same rate (reflecting the protein dynamics under investigation), each individual proteins is in a different configuration in a specific time instant. If the investigation is performed simultaneously over all the proteins the donor-acceptor signal is averaged and its value will correspond to the average donor-acceptor distance. The lack of synchronization between proteins results in the presence of many (all if great number of proteins is involved) possible configurations in any time instant. Differently, single molecule approach provides the time behavior of the signal intensity from each individual protein, as depicted in Figure 2.2, unraveling the dynamics of the protein's configuration.

At the same time, the analysis of the signal from a single protein (single donor-acceptor couple) might reveal rare events involved which will escape notice in a bulk measurement. In Figure 2.2, the sketch concerning the energy transfer efficiency underlines the occurring of such events. The dynamics of the protein might involve sub-processes that happen with low probability or rate. The access to

such detailed understanding of the investigated system, prevented in bulk experiment, is otherwise promoted at single molecule level.

In addition, advances in optical microscopy and spectroscopy techniques have offered the possibility not only to image single molecules, but to investigate their dynamical processes on very fast time scales (picoseconds)[28, 29].

2.2 Wide Field Fluorescence Microscopy: Experimental setup

Fluorescence microscopy has two main modes of operation related to the method to excite the sample: Wide field and Confocal microscopy. In the wide field approach a wide area (larger than the diffraction limited spot, typically of the order of hundreds of μm^2) is irradiated and all emitters are excited simultaneously, see Figure 2.3 (left). The excitation laser light is defocused in order to create this wide excitation area. The advantages of this configuration are exploited in several techniques. Examples are Total Internal Reflection Fluorescence microscopy (TIRF)[30, 31] and Photo Activated Light Microscopy (PALM)[32-34]. TIRF makes use of the evanescent wave obtained when the defocused laser beam is incident to the glass cover slide at an angle equal to or larger than the critical angle so that 100 % of the light is reflected. Nevertheless, the electro-magnetic field propagates into the glass (evanescent wave) resulting in a very thin (~ 100 nm) layer at the coverslip/specimen interface where excitation takes place. The fact that the evanescent wave excites the fluorescence emission only in a very thin layer leads to a dramatic reduction of the background signals, and thereby to a strongly enhanced contrast. In addition, there is a very high depth resolution since this microscopy is only imaging the actual interface. A very high lateral resolution can be obtained by using PALM. This single molecule technique provides images not affected (and limited) by light diffraction, but determined by the localization precision of the single emitters. Thousands of diffraction limited images of single photoswitchable molecules are collected. Afterwards images are analyzed and the position of each molecule is determined with accuracy beyond the diffraction limit. In the final image, individual molecules in the sample are represented as localization accuracy limited spot, one or even two orders of magnitude smaller than the diffraction limited PSF. If on one hand PALM microscopy offers highly resolved images, on the other its design prevents the study of the dynamics of the investigated system.

In contrast to the wide field configuration, confocal techniques work with a diffraction limited focused excitation beam which is scanned over a sample to obtain a complete survey of the sample (see Figure 2.3 (right)). Additionally, a pinhole is placed at the location of a secondary focus before the detector to eliminate the out of focus light allowing only the fluorescence emitted in the focal spot to be detected therefore enhancing the contrast. The name confocal comes

from the fact that the pinhole and the focal point of the lens are conjugated (conjugated planes). Confocal imaging allows the three dimensional investigation of the sample. The excitation/detection spot can perform scans of the sample along x, y and z axis.

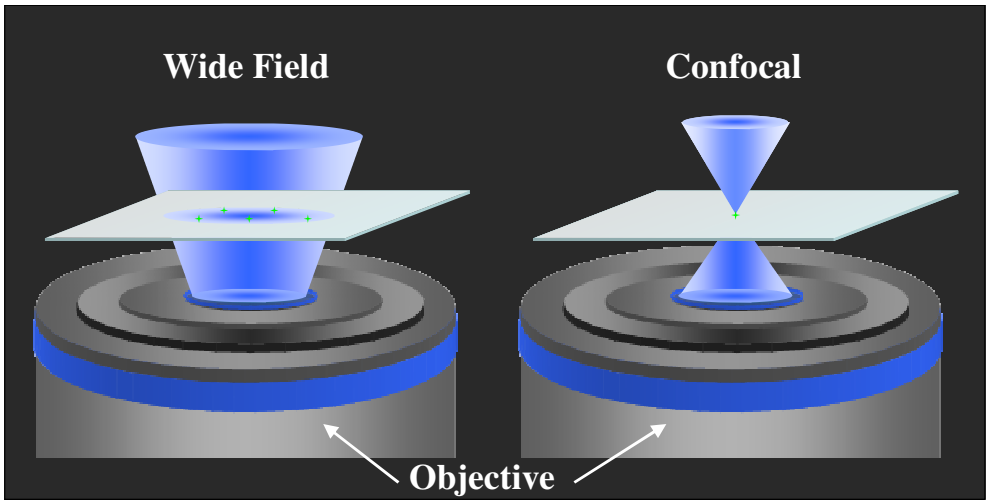

Figure 2.3: Schematic representing the Wide Field and the Confocal microscopy illumination. The coverslide top-surface (sample's position) is placed at the focal distance of the objective in both configuration.

In principle the resolution of normal confocal imaging is determined by diffraction limit. Stimulated Emission Depletion microscopy (STED)[35-37] overcomes this diffraction limit by selectively inhibiting the fluorescence emission from the outer part of the spot, thereby creating an excitation area smaller than the diffraction limit and thus strongly enhancing the image resolution.

In the remainder of this section we will present some of the more technical aspects of wide field microscopy, while the remaining sections of this chapter will focus on some of the issues important for the analysis of the images obtained.

2.2.1 Set up

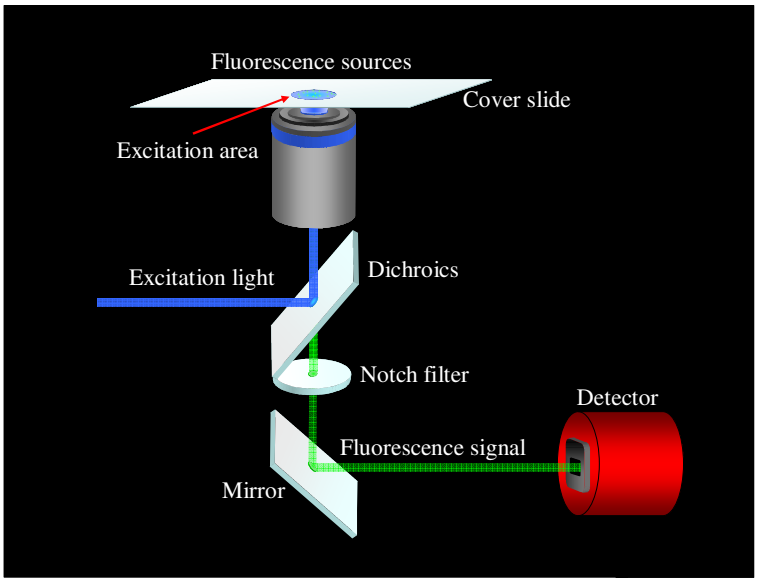

Figure 2.4: Schematic of the wide field fluorescence microscopy set up.

Figure 2.4 presents a schematic of the wide field fluorescence microscope used in this thesis. The excitation laser light is reflected into the microscope path by using a dichroic beam splitter. The alignment is such to provide a divergent beam from the objective lens to irradiate a wide area (disk radius ~ 50 µm) on the samples. The divergent beam is obtained by the use of a telescope in combination with a single lens positioned at the entrance port of the microscope. Fluorescent molecules present in the illuminated area absorb the excitation light and emit the fluorescence signal. The emission is collected by the objective. The collected photons are then separated from the back scattered excitation light by the dichroic beam splitter and by an additional notch filter, selected according to the excitation wavelength. In this way only the wanted fluorescence enters the remaining optics of the microscope (not shown) and is directed to the detector (CCD camera). The CCD chip transforms incident photons into electronic signal which is later processed by a computer.

The instrument used throughout this thesis is based on an inverted microscope (Axiovert 135, Zeiss) equipped with a 100x, 1.4-NA oil-immersion objective (Plan-Apochromat, Zeiss). Various lasers at different wavelengths have been used as excitation source depending on the specific sample. The excitation at the wavelength of 488 nm was provided by a linearly polarized beam of an Ar^+-laser (Innova 300, Coherent). For near ultraviolet wavelength (340-389) the second harmonic of a pulsed Ti:Shappire (730 nm, 76 MHz, 120 fs) (MIRA, Coherent) has

been used, and a He-Ne laser for excitation at 633 nm. The beam splitter and the notch filter are chosen specifically for the used excitation wavelength. The image is recorded using a high sensitivity EMCCD camera (Photonmax 512B, Princeton Instruments) having a CCD chip consisting of 512x512 pixels with 2^{12} dynamical range. To reduce the electronic thermal noise the detector is air cooled at -70°C. The detector, in particular, is crucial for single molecules techniques. The high quantum yield and low background and readout noise of the CCD camera determines the detection limit for ultra-low light signals. An on-chip electron multiplication (EM) gain technology provides a pre-amplification of the signal (photoelectrons) in each single pixel in order to overcome the read out noise of the camera (electronic noise). The microscope is supplied with X-Y piezo stage (P-517, PI) with sub-nanometer resolution, and the objective is mounted on a Z piezo stage (P-721, PI) to provide high 3-dimensional accuracy and resolution in the positioning and imaging of the sample.

2.2.2 Efficiency of the set up

In general, the efficiency is the key parameter that determines the performance of a set up. Any optical technique consists in the implementation of many parts each having their own efficiency. For optics (filters or mirrors) the efficiency regards, for instance, the reflection or the transmission efficiency. In the case of detectors such as the CCD camera, the efficiency is called quantum efficiency and gives the efficiency to generate an electron/hole pair from a single photon, therefore transforming the optical signal into electronic one. The efficiency, to some extent, tells how far the real element is from the ideal case. A mirror with 50% reflection efficiency will reflect only 50 % of incident photons, while the other 50 % will be transmitted or absorbed. The efficiency of each element of the set up determines the total efficiency. In the following we will go over the efficiency of the critical components of the microscope, yielding eventually the total efficiency of the system.

2.2.2.1 Objective

The efficiency of the objective is given by the product of the photon collection efficiency and the transmittance efficiency. The collection efficiency is determined by the collection angle. A fluorescence source presents isotropic (4π solid angle) emission in space; the objective lens can collect only those photons which are incident on the objective. The Numerical Aperture (NA) of the objective is defined as N.A. = $n \cdot \sin \alpha$, where n is the refractive index of the medium in which photons travels, and α is the semi-angle of collection of the lens. It is possible by using media (water or low-fluorescent oil) with n higher than air to achieve NA >1. High N.A. objectives, such as the one used here (NA = 1.4), improve the collection angle. For N.A. = 1.4 the collection semi-angle is > 67° (n_{oil} ~ 1.52), providing a

collection efficiency of ~30% (ratio between the collection solid angle and the total solid angle). The collected photons travel through all the optical elements in the objective consequently reducing further the number of detectable photons. The transmittance efficiency of the objective (in the spectral window between 500 nm and 700 nm) is 75%. The total efficiency of the optics inside the objective is therefore ~23%.

2.2.2.2 Dichroic beam splitter and notch filter

The filter set must be chosen according to the absorption/emission spectra of the fluorescence source(s) present in the sample, and to the excitation wavelength. For experiments concerning Alexa Fluor 488 (peak of emission 520 nm) the efficiency of the filter set is about 85%.

2.2.2.3 Detector

The high sensitive EMCCD camera offers quantum efficiency around 95% between 500 nm and 700 nm.

The total quantum efficiency of the microscope set up is ~ 18% in agreement with experimental tests performed (~17%).

2.3 Software analysis

2.3.1 Background removal or signal-to-noise ratio enhancement

The analysis of collected images is performed by home-developed software. Depending on the nature of the experiment/sample and on the variable under investigation, the software performs calculations specifically designed and developed.

Generally images first undergo a “filtering” process to reduce, if not completely eliminate, the background signal arising from the substrate (Raman or fluorescence) and from the environment (fluorescence) where the sample is studied. This process could be obtained by subtracting or dividing (to normalize the emission of single emitters) in the image the Gaussian profile (2-D Gaussian function) of the background fluorescence signal. Auto-fluorescence of the substrate is promoted by the excitation laser and follows the Gaussian profile of beam.

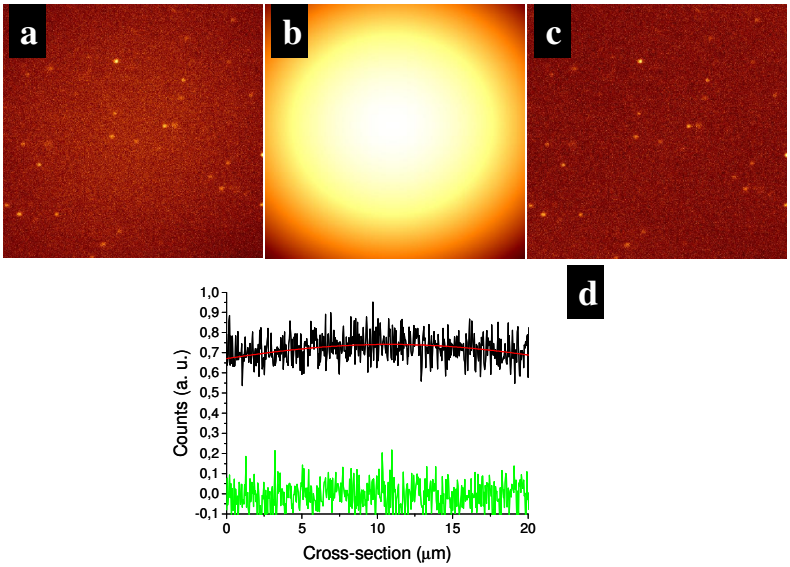

Figure 2.5: Single molecules imaged on the glass coverslide (a). The Gaussian pattern of the background is fitted with a 2-D Gaussian function (b), and removed from the image (c). Panel d shows the cross-sections of the images a (black) and c (green).

Figure 2.5 illustrates the removing of the Gaussian background from an image obtained with fluorescent microscope. Panel a shows the image of a sample consisting of single molecules on a glass substrate after the illumination with laser excitation light. The fluorescence background, following the 2-D Gaussian profile of the laser beam, is observable from panel d (black curve) that represents the cross-section of the sample. By fitting with a 2-D Gaussian function the excitation profile (panel b) it is possible to model it (red curve in panel d) and to subtract from the initial image. The resulting image of the sample (panel c) will result background "free" as visible from panel d green curve and red fit.

An alternative approach to "clean" the image applies a high-pass filter to remove the background and a low-pass filter to reduce the noise. In particular, this second filtering procedure is a pre-manipulation of the actual image that might mislead the correct estimation of certain values such as the noise or the photon count. Therefore, it is preferable to apply it only in certain conditions; for instance with very low signal-to-noise ratio and when the process under investigation is independent from the real photon count. In this thesis, it has been applied in chapter 3 with bright field images of diffusing gold nanoparticles, and in chapter 4.

2.3.2 Fitting functions (Point Spread Function)

Some of the results presented in the thesis concern the characterization of the Point Spread Function (PSF) that is the in-focus image generated by a point-like source. The PSF is a very crucial parameter for any microscopy set up; in fact it identifies the optical resolution of the microscope. The PSF, classically described by the Airy formula[38], can also be approximated by the use of 2-dimensional Gaussian function[39, 40]. A third model, described by Wolf[41], is used under specific conditions as discussed in Chapter 3.

Despite all three formulas have been tested, the 2-D Gaussian function has been applied in this thesis. In particular, the 2-D Gaussian function used in chapter 3 has 7 independent variables (usual 6 plus angle) and takes the form:

$$F(x,y) = H \cdot \exp\left(-4\ln 2\left(\frac{\Delta x^2}{FWHM_{major}^2} + \frac{\Delta y^2}{FWHM_{\min or}^2}\right)\right) + B$$

where (distances from the center):

$$\Delta x = \sin\left(2\pi\frac{\alpha}{360} + \frac{\pi}{2}\right)(x - x_0) - \cos\left(2\pi\frac{\alpha}{360} + \frac{\pi}{2}\right)(y - y_0)$$

$$\Delta y = \sin\left(2\pi\frac{\alpha}{360}\right)(x - x_0) - \cos\left(2\pi\frac{\alpha}{360}\right)(y - y_0)$$

The 7 fit parameters are: H (height), B (baseline), α (angle), X_0 (central position along X-axis), Y_0 (central position along Y-axis), $FWHM_{major}$ and $FWHM_{minor}$. Together with the usual terms height, baseline, X_0 position and Y_0 position, $FWHM_{major}$, $FWHM_{minor}$ and α have been introduced to investigate the anisotropic shape of the PSF and its orientation with respect the X-axis. As it is discussed in chapter 3, under certain conditions the PSF could have elliptical shape. By independently analyze the width of the ellipse along the two axes and the in-plane orientation of the ellipse it is possible to measure the ellipse axis and orientation. Therefore, the fitting procedure provides the values for: amplitude, baseline, central position (X_0 and Y_0), width of the curve in both the directions (FWHMs of the Gaussian, $FWHM_{major}$ and $FWHM_{minor}$), and the angle between long axis (ellipse) and the X-axis.

The calculation of the best fit could be achieved with a monte carlo method or with a standard Levenberg-Marquardt method[42]. In particular this analysis has been adopted in the characterization of the PSF described in the following paragraphs, and in all the experiments where the PSF is involved.

2.3.3 Single particle tracking

In chapter 4, Brownian diffusion of micro- and nanoparticles in various liquid solutions is studied and compared to the motion promoted by chemically-driven self-propulsion acting on the same particles. The nanoparticle motion is quantified using home-developed single-particle tracking[43, 44] software. First, for each frame the slowly-varying fluorescence background that mainly followed the excitation beam profile is subtracted. Second, the xy-position of a selected particle is determined by fitting its fluorescence image with a 2-D Gaussian function.

Such a procedure provides a ±15–nm accuracy (as concluded from tests on surface-immobilized nanoparticles), which is consistent with the theoretically-estimated sem[45, 46] value of 10-15 nm.

For the subsequent frame, an additional condition is applied. The position of the selected particle has to be within a preset range (typically, <800 nm) from the previous frame to allow automated assignment of the particle.

This procedure is continued until either the particle falls out off focal plane in the z-direction or two particles collide and therefore become indistinguishable.

Finally, the mean square displacement (MSD) is calculated and averaged amongst all tracked particles, and the stepsize distribution, consisting of the sum of all the steps of tracked particles, is calculated and displayed.

2.3.4 Quantitative analysis

Quantitative analysis of the photons collected by a single PSF discussed in chapter 5 could provide information about the number of single emitters forming the PSF and therefore not optically resolvable. An area, centered at the position of the PSF, is selected and the sum of the counts from the included pixels is calculated. If images are collected in an array of subsequent frames (movie), the photon count time-dependence is calculated and displayed.

2.4 Experimental details

2.4.1 Point Spread Function characterization

In order to gain access to a more detailed characterization of the PSF, a sample consisting of single fluorescent dipole emitters (Alexa Fluor 488) dispersed in a polymer glassy matrix thin film (~ 100 nm) was prepared. A solution containing Alexa Fluor 488 and Poly(methyl methacrylate) (PMMA) molecules dispersed in chloroform was spin coated onto a glass microscope slide (170 μm thick). PMMA was chosen because of its high glass transition temperature (~ 100° C)[47], and Alexa Fluor 488 because of its high quantum efficiency (~ 95%) at 488 nm wavelength used as excitation. The resulting sample consists of a thin film with well spatially

separated single dipoles of fixed orientation that, when imaged through a high NA objective, present elliptical PSFs.

Images of several distinct single emitters were obtained at 2 Hz frame rate in areas of ~ 21 x 21 μm. Measurements have been performed by using laser excitation from the Ar^+ laser at 488 nm and in two different orientations (X- and Y-axes) of the linear polarization. The "horizontal" linear polarization (along X-axis of the image) has been obtained from the "vertical" linear polarization (along Y-axis) of the laser by using a λ/4 plate and a polarizer.

Individual PSFs have been analyzed by using a two-dimensional Gaussian function with the two axes of the ellipse and the angle between the long axis and the X-axis as free parameters.

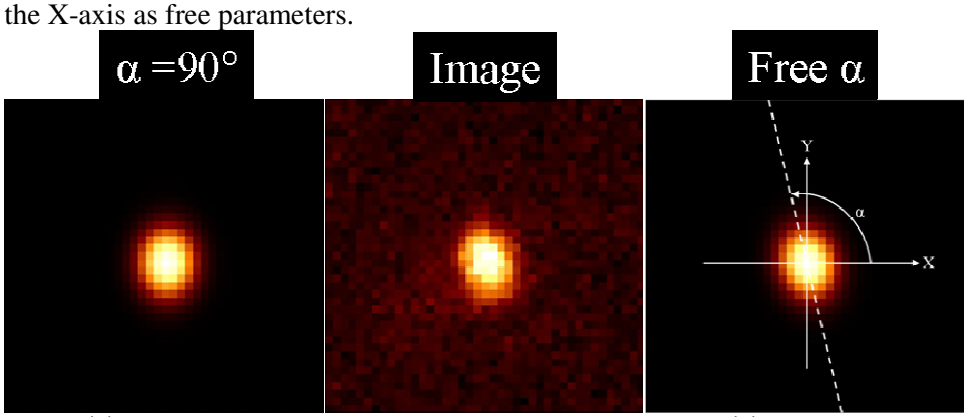

Figure 2.6: Real image of an elliptical PSF of a single dipole and two fitting functions. By keeping the angle fixed it is possible solely to achieve resolution beyond the Abbe's limit. If in the function is added a term describing the angle of the long axis of the ellipse, the in-plane orientation of the dipole is gained.

Figure 2.6 sketches one of the main results obtained. If a single dipole with fixed orientation is imaged, its PSF assumes an anisotropic shape and from circular (Airy formula)[38] becomes elliptical[41]. This further enhances the information achievable beyond the Abbe's limit. To the super resolution accuracy in the position of the dipole, often reported in literature, the in-plane orientation of the dipole is added.

2.4.2 Single particle tracking

In single particle experiments, see chapter 4, the motion of nanoparticles is measured and characterized in liquid solutions. To measure pure Brownian diffusion demands the liquid to be fully confined in order to prevent drift motion or evaporation of the solution.

The sample is placed in a cell consisting of two standard cover glass slides (thickness of 0.17 mm) separated by a microscope slide (thickness of 1 mm) with a 3-mm diameter hole in it. This arrangement prevents evaporation of the solvent and therefore allows maintaining a constant H_2O_2 concentration.

The motion of the nanoparticles is measured in solutions of ethanol and water, to which H_2O_2 is added at different concentrations: 1% in the experiment involving bi-functionalized silica nanoparticles (radius ~290 nm) and 25 % for gold nanoparticles (~45 nm).

Because of the linear dependence of the diffusion coefficient (D) with the radius of the diffusing object, movies recorded have been taken at different frame rate. Silica nanoparticles have been imaged with 20 Hz frame rate, gold spheres at 33 Hz (25 % H_2O_2) and at 40 Hz (no H_2O_2).

In order to avoid possible influence on the Brownian diffusion from the substrate, the focal plane of the objective has been set at 100 μm above the substrate surface.

2.4.3 Quantitative analysis

The access to single molecule emitters gives access, thank to their photo-physical features, to quantitative characterization of the number of emitters in a single PSF. As mentioned already, the details inside the PSF are optically irresolvable. Nevertheless, it is possible to take advantage of the stochastic behavior of the emission from a single florescent molecule. In the same condition (same intensity of light, same class of molecule, same environment) blinking and bleaching events might happen at different times[48]. Usually such events happen on time scales much faster than the frame rate at which molecules are imaged.

By imaging a single molecule one can observe the molecule emitting fluorescence and suddenly disappear. Such events, only observable at single molecule level, will be described in more details in chapter 5.

If a PSF consisting of several single emitters is imaged for long enough time will show a decreasing intensity-time trace till the complete bleach. If the number of emitters in the PSF is <10 the intensity time trace will vary not linearly or exponentially, but through steps of about homogeneous amplitude. Each step in the intensity curve represents the sudden emission bleach/quench of a single molecule. By integrating the counts in all pixels in an area surrounding the PSF it is possible to measure the emission intensity time trace[49-51].

Figure 2.7 introduces an example of application of the quantitative analysis. A batch of single molecule is attached to a quartz slide and irradiated for fluorescence imaging.

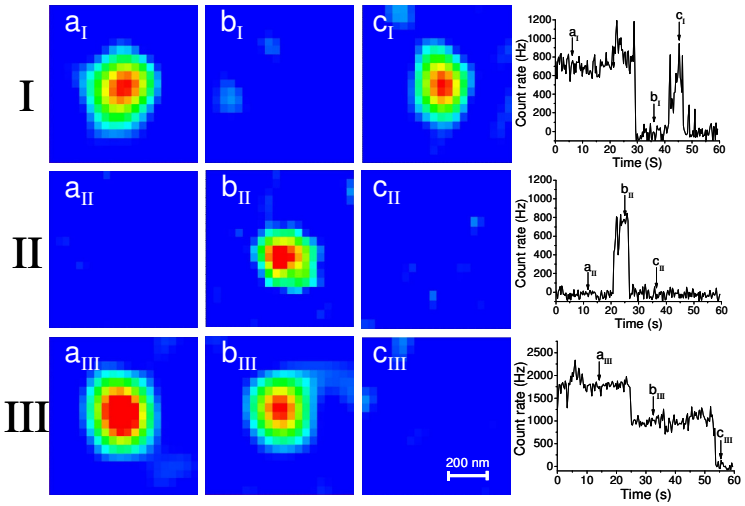

Figure 2.7: Fluorescence images of molecules grafted to a quartz slide at three different locations (I, II, and III) and times (a, b, c). The integrated fluorescence signal at each location is shown at the right panel as a function of time. The on/off blinking behavior of I and II is consistent with the characteristic emission by a single molecule. The time trace of object III suggests that the signal originates from two unresolved single molecules.

Quantitative characterization of the imaged PSF allows determining whether consisting of single molecules (PSFs I and II) or two spatially irresolvable emitters (PSF III). The fluorescence signal from an area of radius 240 nm around individual PSFs is integrated and presented as a function of time.

PSF labeled I and II show intensity time traces typical from single emitters. The fluorescence signal varies from high signal (fluorescence) to zero signal (background signal) and the sudden variations happen within a single frame and in a single step.

Diversely, the trace relative to PSF III presents an intermediate step between high signal to no-signal. Two steps are observable having about the same amplitude. The point spread function III consists of two single emitters not resolvable spatially.

Quantitative analysis has been performed on a different system, described in chapter 5. The aim of the study is to estimate the number of the protein secYEG embedded into a membrane (proteoliposome). A single proteoliposome consists of water-filled spherical membrane. Each protein is labeled with a single molecule of Alexa Fluor 488. By counting the number of fluorescent molecules it is possible to evaluate the number of proteins in a single proteoliposome. The large size of the spheres (radius > 100 nm) allows the contemporary presence of several proteins.

2.5 Conclusions

The Wide Field Fluorescence Microscope set up is described and characterized in all its constituents. A brief introduction is used to highlight the developments and achievements a modern microscope should provide. The most significant aspects characterizing the wide field configuration are introduced and compared to other fluorescent microscopy techniques based on confocal microscopy.

Furthermore the experimental procedures and data analysis are presented for several investigated systems. Characterization of the PSF, super-resolution microscopy, single particle tracking and quantitative analysis at single molecule level are introduced and support the achieved competitive performances of the technique. For instance, the measured super resolution accuracy of 1 nm and the quantitative analysis of the intensity of a single PSF, consisting of 6/7 molecules, represent valuable achievements.

The direct observation of the ellipticity of the PSF of a single dipole while imaged through high NA objective might result in a much wider matter of discussion and provide eventual applications.

The broad spectrum of topics treated in the thesis (pure optics, nanotechnology, biology, and chemistry) emphasizes the potential and the versatility of modern fluorescence microscopy.

Bibliography

1. Stokes, G. G. *Philosophical Transactions of the Royal Society of London* **1852,** 142, 463-562.
2. Coons A. H., C. H. J., Jones R.N.,. *Proc. Soc. Exp. Biol. Med.* **1941,** 47, 200-202.
3. J. Ellenberg, J. L.-S., and J. F. Presley. *trends in CELL Biology* **1999,** 9, 52-56.
4. R. Rizzuto, M. B., F. De Giorgi, R. Rossi, R. Heim, R. Y. Tsien, T. Pozzan. *Curr. Bio* **1996,** 6, (2), 183-188.
5. Lakowicz J. R., *Principles of Fluorescence Spectroscopy*. 3 ed.; Springer: 2006.
6. Pawley, J. B., *Handbook of Biological Confocal Microscopy*. Third ed.; 2006.
7. R. Ando, H. M., A. Miyawaki. *Science* **2004,** 306, 1370-1373.
8. S. Habuchi, R. A., P. Dedecker, W. Verheijen, H. Mizuno, A. Miyawaki, J. Hopkins. *Proc. Nat. Am. Soc.* **2005,** 102, (27), 9511-9516.
9. J. K. M. Sanders, S. E. J. *Chem. Soc. Rev.* **2009,** 38, 2821-2822.
10. B. Schuler, E. A. L., W. A. Eaton. *nature* **202,** 419, 747-747.
11. H. Noji, R. Y., M. Yoshida, K. Kinosita Jr. *nature* **1997,** 386, 299-302.
12. J.B. Lee, R. K. H., S.M. Hamdan, X.S. Xie, C.C. Richardson, A.M. van Oijen. *nature* **2006,** 439, 621-624.
13. K. Blank, G. D. C., J. Hofkens. *Biotech. J.* **2009,** 4, 465-479.
14. G. De Cremer, Y. A., M. B. J. Roeffaers, M. Sliwa, J. Van Noyen, S. Smout, J. Hofkens, D. E. De Vos, B. F. Sels, T. Vosch. *Angew. Chem. Int. Ed.* **2008,** 47, 2813-2816.

15. T. Oltersdorf, e. a. *nature* **2005,** 435, 677-681.
16. A. Tafvizi, F. H., J.S. Leith, A.R. Fersht, L.A. Mirny, A.M. van Oijen. *Biophys. J.* **2008,** 95.
17. D.L. Floyd, J. R., J.J. Skehel, S.C. Harrison, A.M. van Oijen. *Proc. Natl. Acad. Sci. USA* **2008,** 105, (40), 15382-15387.
18. P. Dedecker, B. M., A. Deres, H. Uji-i, J. Hotta, M. Sliwa, J.-P. Soumillion, K. Müllen, J. Enderlein, J. Hofkens. *Advanced Materials* **2009,** 21, (10-11), 1079-1090.
19. M. B.J. Roeffaers, R. A., M. Baruah, H. Uji-I, M. Bulut, G. De Cremer, U. Müller, P. A. Jacobs, J. Hofkens, B. F. Sels, D. E. De Vos. *J. Am. Chem. Soc.* **2008,** 130, 5763-5772.
20. Ruei-Yu He, Y.-D. S., Keng-Chi Cho, Chun-Yun Lin, Nan-Shan Chang, Chih-Han Chang, and Shean-Jen Chen *Opt. EXpr.* **2009,** 17, (8), 5987-5997.
21. Euiheon Chung, Y.-H. K., Wai Teng Tang, Colin J. R.; Sheppard, a. P. T. C. S. *Opt. Lett.* **2009,** 34, 2366-2368.
22. Jörg Enderlein, E. T., Paul R. Selvin. *Opt. Expr.* **2006,** 14, (18).
23. N. Panchuk–Voloshina, R. P. H., J. Bishop–Stewart, M. K. Bhalgat,; P. J. Millard, F. M., Wai-Yee Leung, and R. P. Haugland. *J. Histochem. & Cytochem* **1999,** 47, (9), 1179-1188.
24. N. J. Dovichi, J. C. M., J. H. Jett, M. Trkula, R. A. Keller. *Anal. Chem.* **1984,** 56, 348-354.
25. W.E. Moerner, L. K. *Phys. Rev. Lett.* **1989,** 62, (21).
26. M. Orrit, J. B. *Phys. Rev. Lett.* **1990,** 65, (21).
27. H. P. Lu; X. S. Xie. *J.Phys. Chem. B* **1997,** 101, 2753-2757.
28. X. S. Xie; Dunn, R. C. *Science* **1994,** 265, 361-364.
29. Roeffaers, M. B. J.; Cremer, G. D.; ...; Hofkens, J. *Proc. Nat. Am. Soc.* **2007,** 104, (31), 12603-12609.
30. D. Axelrod, N. L. T., T. P. Burghardt. *J. Micro. Oxf.* **1983,** 129, 19-28.
31. S. Hamdan, J. L., M. Takahashi, C. Richardson, A. van Oijen. *Nature* **2009,** 457.
32. S. T. Hess, T. P. K. G., M. D. Mason. *Biophys. J.* **2006,** 91, 4258-4272.
33. E. Betzig, e. a. *Science* **2006,** 313, 1642-1645.
34. M. J. R. Rust, B. B., X. Z. Zhuang. *Nat. Methods* **2006,** 3, 793-796.
35. S. W. Hell, J. W. *Opt. Lett.* **1994,** 19, (11).
36. T. A. Klar, S. J., M. Dyba, A. Egner, S. W. Hell. *Proc. Nat. Am. Soc.* **2000,** 97, (15).
37. C. Eggeling, e. a. *Nature* **2009,** 457.
38. Airy, G. B. *Trans. Cambr. Philos. Soc.* **1835,** 5, 283-291.
39. C. M. Anderson, G. N. G., I. E. Morrison, G. V. Stevenson, R. J. Cherry. *J. Cell. Sci.* **1992,** 101, 415-425.
40. M. K. Cheezum, W. F. W., W. H. Guilford. *Biophys. J.* **2001,** 81, 2378-2388.
41. B. Richards E. Wolf. *Proc. R. Soc. London* **1959,** 253, (1274), 358-379.
42. W. H. Press, S. A. T., W. T. Vetterling, B.P. Flannery, *Numerical recipes in C*. Cambr. Univ. P.: 1996; Vol. 2, p 683.
43. Saxton, M. J.; Jacobson, K. *Annual Review of Biophysics and Biomolecular Structure* **1997,** 26, 373-399.
44. Hellriegel, C.; Kirstein, J.; Brauchle, C. *N. J. Phys.* **2005,** 7.
45. A. Yildiz, J. N. F., S. A. McKinney, T. Ha, Y. E. Goldman, P. R. Selvin. *Science* **2003,** 300, 2061-2065.
46. R. E. Thompson, D. R. L., W. W. Webb. *Biophys. J.* **2002,** 82, 2775 - 2783.

47. K. Wondraczek, J. A., J. Fuhrmann. *Macromol. Chem. Phys.* **2004,** 205, 1858-1862.
48. M.P. Gordon, T. H., P. R. Selvin. *Proc. Nat. Am. Soc.* **2004,** 101, (17), 6462-6465.
49. Bopp M. A.; Hochstrasser R. M.; et al. *Proc. Nat. Acad. Sci. USA* **1997,** 94, 10630 - 10635.
50. Gordon M. P.; Ha T.; Selvin P. R. *Proc. Nat. Acad. Sci. USA* **2004,** 101, (17), 6462 - 6465.
51. Nakajo K.; Isacoff E. Y.; et al. *Proc. Nat. Acad. Sci. USA* **2010**, 1 - 6.

Chapter 3
Motion of catalytically active nanoparticles

3.1 Introduction

Nanotechnology aims at gaining control over matter at the nanoscale in order to imitate functions well known from our daily life at the macroscopic length scale. One of the important issues confronting nanotechnology is the capability to create, in synthetic micro- and nanoscale structures, delivery systems of objects in fluid environments [1-5]. Nano-cars[6, 7], nano-rotors[8, 9], and molecular shuttles[10, 11], are but a few of the new approaches to tackle a diversity of nano-engineering challenges[12-14].

Despite recent improvements[15], conventional approaches to transport objects at small scales, such as optical trapping, electro-[16] and magnetophoresis[17, 18], have intrinsic limitations. On the one hand optical trapping methods can control the position of individual particles (or small groups thereof) quite accurately; on the other hand, the use of fields severely limits the needed flexibility for transporting objects independently. An efficient and flexible delivery system should be able to transport each individual element of the ensemble independently with a high degree of accuracy.

A promising attempt to obtain motility of individual objects independently from external fields is based on the concept of self-propulsion, that is, on the ability of each of the individual objects to perform independent motion. In order to do that, it is necessary to gain control over the direction of the motion, a task that may prove difficult to accomplish since different materials (cargos) might require different sorts of control. The latter might be achieved by using external fields (see Ref. 25) or by generating a kind of attractive driving force (charge, concentration) between the single cargos and the destination. Another challenge is to drop off the cargo. A recent work[19] has reported the successful use of photochemical stimuli to achieve this. In any case, attaining controlled motion first concerns the motion itself, preferably in an induced manner.

Over the last years, several examples of catalytically-driven self-locomotion of objects, ranging in size from centimeters down to micrometers, have been

documented[20-26]. Studies on these systems have focused on the method of chemical to mechanical energy conversion as well as on different models describing the propulsion mechanism. It has been shown, for instance, that the process of catalytic conversion of chemical energy into motion depends strongly on the size of the objects[27]. In systems bigger than a few μm, motion is due to the formation/emission of gaseous bubbles, whereas in objects of a few μm propulsion occurs without bubbles. The current understanding obtained at the microscale might or might not be relevant at the nanoscale. What happens if the self-propelling structures are further reduced in size? Can we simply use existing microscale knowledge? Does self-propelling still work at the nanoscale? Can we still visualize this? These and other questions are the main focus of the present chapter.

The step from micro to nano is not straightforward. One of the most critical aspects is the influence of the environment; the nanoscale world is dominated by thermal forces such as the Brownian force, and it is a world where viscous and surface forces prevail over inertial and body forces. The pursuit of self-propulsion of nano-objects faces two main issues:

- Is propelled motion achievable?
- How to separate it from the incessant action of Brownian motion?

This chapter presents a study of the motion of nanoparticles performing the same catalytic activity as used at the microscale. The behavior of particles is first investigated in case of pure Brownian diffusion, after which it is compared to the motion when the catalytic reaction is occurring.

In order to achieve a quantitative characterization of Brownian motion features, a single particle tracking technique has been applied[28, 29]. Fluorescence and bright field microscopy gives access to the time dependent position traces, r(t), of individual particles. Information such as step size at given time-lag and mean square displacement are extracted and analyzed to discriminate the effects of Brownian random force from the propelling force.

It is shown that the catalytic activity occurring on the surface of noble metal nanoparticles (gold and platinum) as well as on silica nanoparticles functionalized by molecular complexes (catalytic molecular motors) is unable to generate a propelling force strong enough to overcome, or even influence the purely Brownian motion.

The present chapter introduces the various examples and aspects through an extensive literature overview so to list, describe and underline the various aspects concerning the problem of chemically-driven self-propulsion. Following, a detailed characterization of the concept of Brownian motion is given. Which are the main features of the random motion and how to recognize it will result central for the pursuit of self-locomotion at nano-scale. Afterwards, a wide range of experimental results is presented and discussed.

3.2 Literature overview on catalytic propulsion

The first challenging demand in the quest for self-propulsion is to provide energy to individual objects in order to gain autonomous motion. Biological systems such as motile bacteria move independently of external fields and independently of one another by consuming chemical energy that is available in their environment. Similarly, a nano machine requires an "engine" to generate propulsion by transforming a fuel harnessed directly from the environment into mechanical motion. The high energy scale involved in chemical processes is very attractive in the pursuit of self-propulsion. An addition advantage is that chemical fuel may often be harnessed directly from the immediate environment.

One of the earliest examples of the conversion of chemical energy into mechanical motion is the movement of a camphor disk immersed in water due to the chemical reaction occurring on its surface[30, 31]. In this case, however, the chemical reaction dissipates the disk. The dissipative nature of this process obviously limits its applicability, and there is a need for non-dissipative micro- and nano-machinery. Fortunately, there is also a class of chemical processes which leaves at least one of the components involved in the reaction unaltered: catalytic reactions. In these reactions one of the components, the catalyst, enhances the rate of a reaction without decomposition of the catalyst itself. An engine based on a catalytic reaction may therefore be an adequate solution to the problem of autonomous movement of nano- and micro-objects. It can virtually work *in perpetuum*, at least as long as the fuel is replenished.

In 2002, the Whitesides group was the first to report induced motion of an otherwise inanimate object using a platinum surface as its engine[20]. Chemical energy was converted into mechanical energy by the decomposition of hydrogen peroxide (the fuel), catalyzed by the platinum surface. Whiteside's idea of using metal as catalyst was followed and further developed by many other groups, providing insight into the wide spectrum of aspects governing chemically-driven autonomous motion, including collective effects of the ensemble of engines, asymmetrical distribution of reaction products, and theoretical models for the induced propulsion.

The present section introduces the importance and role of the aforementioned aspects. Examples presented show systems performing self-locomotion as the result of a collective effect from the large surfaces used as active material in the conversion of the chemical fuel into motion. For some machines the motion is promoted by the propelling action originated by the release of oxygen bubbles. This occurs when the active material is larger than a few micrometers. In self-propelled objects of a couple of μm the motion is obtained without bubble formation supporting the idea that a different mechanism is the cause of the observed motion. Even if different mechanisms of propulsion are observed in objects of different size they all present asymmetric release of the reaction products

(oxygen). Asymmetric shapes of the self-propelling objects appear to be crucial to attain propulsion.

The first group of examples concern objects having size from centimeters down to tens of micrometers, while the second group focuses on micrometer-sized objects.

3.2.1 First group (size: cm - tens of μm)

3.2.1.1 Hemicylindrical plates

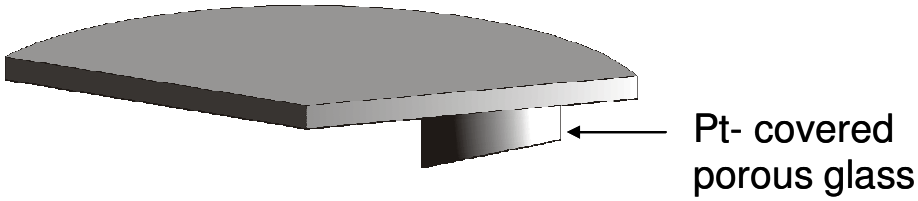

Figure 3.1**:** Schematic of the self-propelling object from Ref. [20].

The first device based on a catalytic engine was proposed by the group of Whitesides[20]. Figure 3.1 shows the schematic of the self-propelling object having a size of about 1 cm. They have developed machines capable of autonomous motion to investigate the influence of the collective behavior in the self-assembly process of the moving plates. Hemicylindrical plates, having a small platinum surface, are placed at the liquid-air interface of a 1-3% aqueous solution of H2O2. The decomposition of hydrogen peroxide catalyzed by Pt into water and oxygen (2 H2O2 (l) → O2 (g) + 2 H2O (l)) transforms chemical energy into motion through the release of gaseous oxygen. The observed rotational motion is caused by the asymmetric distribution of the catalytic material, indicated by the bar, as shown in the Figure 3.2. The same motion was reproduced by 20 plates.

The mechanical energy is generated by the recoil of the liquid as the bubbles burst on the liquid-air interface. The propelled objects move away from the region with high concentration of products (oxygen) as represented in Figure 3.2.

Oxygen bubble formation is promoted by the amount of oxygen released in the chemical reaction. The oxygen produced in the vicinity of the catalyst diffuses away in the solvent, but if the production rate is sufficiently high, molecules of oxygen can nucleate forming bubbles. Platinum surface generates a collective effect, arising from the activity of single active Pt atoms, able to generate oxygen molecules at such concentration to allow the nucleation of bubbles.

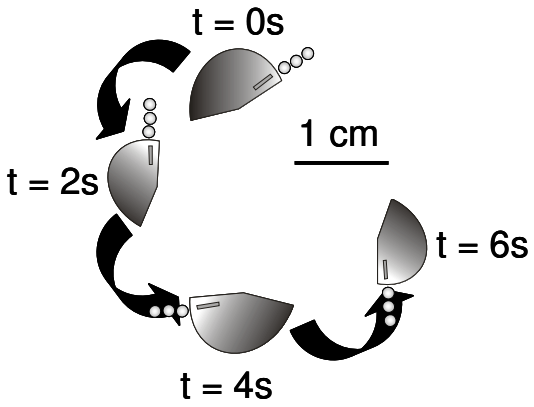

Figure 3.2**:** Schematic of the motion performed as reported in Ref. [21].

3.2.1.2 Multi-metallic tubes

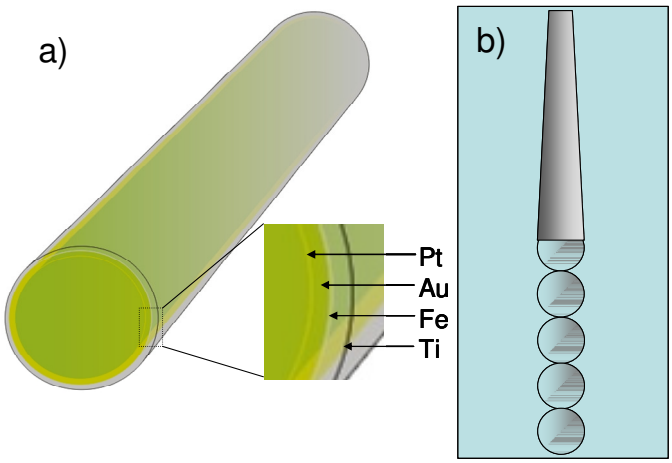

Figure 3.3: Schematic representation of the rolled-up microtube described in Ref. [25] (a). Schematic of the micro-bubbles tails visualizing trajectories (b).

A different method of propulsion, reminiscent of a jet engine, has been proposed by Sololev *et al.*[24]. They studied multiwalled metallic microtubes in which the inner wall was platinum (see Figure 3.3). Figure 3.3 shows the scheme of the rolled-up microtube (length 20-30 μm) having an inner catalytic surface (Pt)[24]. The inset of Figure 3.3a shows the microtubes consisting of Pt/Au/Fe/Ti multilayers. The decomposition of H_2O_2 by the inner active layer generates oxygen bubbles.

Figure 3.3b illustrates bubbles being created inside the tube and then expelled. Bubbles collect the gas released in the catalytic reaction, and while expanding they

move towards the larger opening of the tube, thrusting it forward upon ejection. The direction of the motion is affected by the tube shape-asymmetry along the axis (Figure 3.3b), since the bubbles are expelled from only one side of the tube. An additional magnetic layer is inserted into the wall to gain remote control of the direction of the motion with the use of a rotating magnetic field[24].

The microtube system differs profoundly from the previously described example. Here, the diffusion of the reaction products (oxygen) in the surrounding liquid, which mainly effects the nucleation of bubbles, is inhibited by the wall facilitating the bubbles formation. The question the authors wanted to address using this design is how the size and ejection rate of the bubbles influence the tube velocity. It has been found that this velocity is proportional to the product of the radius and ejection frequency of the bubbles, where the frequency is proportional to the H_2O_2 concentration.

3.2.2 Second group (size: a few μm)

3.2.2.1 Bimetallic rod-shaped micro-particles

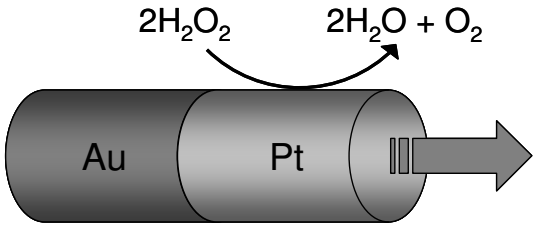

Figure 3.4**:** Schematic of the asymmetric Pt-Au micro-rod driven by the catalytic reaction as reported in Ref. [22].

Both previous examples showed propulsion driven by bubble formation. When the objects become smaller, the total rate of oxygen production decreases eventually leading to the absence of bubble formation. That also in this case one can still have chemically driven propulsion has been shown by the group of Paxton[21]. They considered the motion of micrometer sized bi-metallic rods. The schematic of the rod-like shaped particles is presented in Figure 3.4. Rods are 370 nm in diameter and consist of two 1 μm-long segments of platinum and gold.

Self-propulsion has been reported through the observation of movement of such rods in a 2-3% aqueous solution of hydrogen peroxide. Results have shown particles to move predominantly along their long axis, in the direction of the Pt-end, and without the nucleation of bubbles. Platinum's catalytic activity (two orders of magnitude higher than that of gold) allows one to consider gold as a virtually inactive element of this system[32]. The authors suggest that the driving force, estimated to be of the order of 10^{-14} N, is generated by an oxygen concentration gradient established along the longitudinal axis of the rods.

Similar results have been obtained by Ozin and Manners using nickel-gold rods[22].

3.2.3 Proposed mechanisms of propulsion

3.2.3.1 Bubble propulsion model

Bubble nucleation at the catalytic site occurs when the production of oxygen is such that its concentration enables the clustering of molecules into a bubble. Oxygen molecules released in the reaction diffuse away from the reaction site with a diffusion coefficient that in water at 25°C is about $2x10^3$ $\mu m^2/s$[33]. It has been demonstrated that a gas bubble in a liquid is an unstable system. The exchange of gaseous molecules with the surrounding liquid determines the lifetime of the bubble. In water, a very small oxygen bubble of for instance radius ~ 100 nm, has a lifetime < 0.1 ms, whereas a bubble of 1 mm radius could last for more than 80 days[34].

The number of oxygen molecules, determining the concentration and the size of the bubble, linearly depends on the number of active sites and on the reaction rate. Considering a catalyst, i.e. Pt, at a given concentration of hydrogen peroxide the reaction rate can be (to some extent) assumed constant, making the number of active sites (platinum atoms) the key parameter. Although trivial, the latter is a crucial factor in the study of propulsion mechanism. In the described examples, propelled motion via bubble formation has been observed in objects having dimensions above few micrometers. The mechanism of bubble propulsion is applicable only to objects that have dimensions sufficiently large to favor the nucleation of bubbles.

Once bubbles are formed, the propelling action is promoted by the recoil force as the bubbles move away in the liquid or as the bubbles burst, if the object is close to the liquid-air interface. The overall effect of the bubbles' action must provide a net force. If two bubbles having the same size are created at the two opposite ends of the particle, it will not move. This is because the net recoil force in that case is zero. Homogenously distributed nucleation of bubbles on the particle surface will not generate propelling action unless asymmetry is introduced.

The system consisting of microtubes is more complex. Here, the inner catalytic wall is used not only for the reaction itself, but also as gas-collecting cavity. Microtubes work like rockets, since bubbles are ejected out of the tube by the increased pressure inside the tube. Each single ejected bubble causes the tube to move in the opposite direction with a step approximately equal to the size of the bubble[24]. The larger the bubble, the bigger this step will be. At the same time, the ejection rate determines the velocity (velocity ~ bubble size x ejection rate).

3.2.3.2 Interfacial tension gradient propulsion model

Particles having a size of a few μm, as in the case of the bi-metallic rods described in section 3.2.2, exhibit propelled motion without bubble formation. The main difference with systems propelled by bubbles is the reduced size; this might suggest that the laws governing the motion could be different at smaller scale.

The motion of micro- and nanometer-sized objects in a liquid belongs to a class of objects that in fluid dynamics are described by low Reynolds numbers[2, 35]. The Reynolds number (Re) is a dimensionless quantity that measures the ratio of inertial forces to viscous force. For low Re number the motion is governed by viscous forces rather than inertial forces. In this regime, the viscous drag forces tend to cancel any momentum-based motion of micro- and nano-objects. The motion at a particular instant in time is entirely determined by the force at that particular moment and it is not influenced by the past history. For example[2], a 'micro-swimmer' of about 1 μm size is pushed to a speed of 30 μm/s in water. If the pushing force is suddenly stopped, the swimmer will drift for only another 0.1 Å, being stopped within 0.6 μs.

Objects of small dimensions present a marked increase in surface to volume ratio which favors surface forces vs body forces (i. e. drag force vs inertial force). It has been suggested by Paxton and co-workers[21] that the oxygen concentration gradient, generated by asymmetrical release (Pt segment), developed an asymmetric interfacial tension around the Pt-Au rod. The generated interfacial gradient is responsible for a slip velocity at the object-liquid interface propelling the rod preferably along the long axis, further assisted by the reduced drag force. As the rod moves, the gradient is re-established by the catalytic action of Pt. In addition, they estimated the speed to be linearly dependent on the oxygen evolution rate. The direction of the motion, in particular, has been investigated extensively by the same group. It was found that bi-metallic rods move towards the platinum end, hence towards the catalytic side of the object, in contrast to bubble-propelled systems.

New insights and interpretation of the propelling mechanism were proposed in 2005[36]. A system complementary to the Pt-Au nanorods, consisting of a silver catalyst immobilized on the Au surface, promotes "fluid pump". A similar electrokinetic mechanism of fluid flow was previously reported by Mano et. al.[37] The catalytically-driven convective motion observed by Kline et. al.[36] has been attributed to an electrokinetic mechanism generated by the electrochemical decomposition of hydrogen peroxide. Further evidence of the self-electrophoresis phenomena has been reported[38] by Paxton and used to re-interpret the previously reported axial motion of the bi-metallic rods.

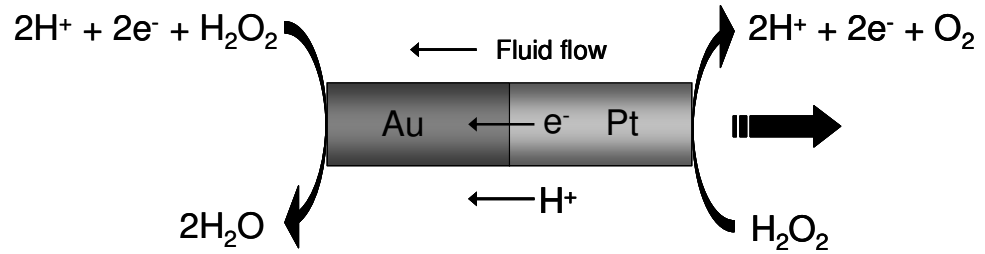

Figure 3.5: Schematic of the proposed self-electrophoresis propelling mechanism as described in Ref[40].

Figure 3.5 illustrates the self-electrophoresis mechanism as described by Paxton[38]. The platinum end of the bi-metallic rod oxidizes hydrogen peroxide releasing protons in the liquid and electrons in the rod. Afterwards, the gold end of the rod consumes protons and electrons by reducing H_2O_2. This process generates an ion flux that propels the particle in the fluid towards the Pt end. By substituting Pt with Catalase, an enzyme that decomposes H_2O_2 nonelectrochemically, no axial motion of the rods was observed[38].

The introduced electrophoresis mechanism requires electron transport between the two ends of the rod. Nevertheless, a few-micrometers-sized non-metallic Si "backbone" asymmetrically coated with Pt or Ag has also shown catalytic propelled motion, this time away from the active area[39].

The described examples show that even if various approaches have achieved catalytic self-propulsion at micro-scale, the origins of the propulsion mechanism are still matter of discussion and investigation.

3.3 Nanoparticles

The examples described above show how catalytic reactions occurring on the surface of objects with sizes from cm down to a few μm are able to transform chemical energy into mechanical energy, thereby inducing self-propulsion. In addition, it has been shown that the mechanism of propulsion is not unique, but quite dependent on the particular size of the object.

This chapter is intends to study the influence of the same catalytic reaction on the motion of nanoparticles.

Is a similar propelling action achievable if the objects involved are smaller then 1 μm? The nanoscale world is strongly dominated by thermally driven forces such as the Brownian force, whose influence strengthens as the size of the objects reduces. The features of the unavoidable Brownian motion require quantitative characterization since they represent the background in which the propelling action might arise. To do so, the diffusive motion must be directly measured.

The single particle tracking technique gives direct access to the path followed by single diffusing particles, whose ensemble behavior can be statistically

described by knowing the trajectory of each individual particle. How to characterize Brownian diffusion by the single particle tracking technique, and how self-propulsion may deviate from the purely diffusive motion is discussed in this work.

3.3.1 Brownian motion and the single particle tracking technique

When suspended in a liquid, microscopic bodies perform a random movement called Brownian motion (Figure 3.6). The latter takes its name from the botanist Robert Brown, who in 1827 studied and documented the motion of small pollen grains in water. Though not the very first, he was one of the first pioneering experimentalists to perform systematic studies on the motion of organic and inorganic objects. In "De Rerum Natura" (II, 112-141), Lucretius (1st century B.C., atomism) describes the physical basis of the phenomenon: "*…dust particles in sunbeam have an irregular motion since continuously bombarded by invisible blows of restless atoms*". Despite the more scientific approach, Brown failed, as a botanist, to rule out a specific organic origin of the motion. He addressed the Brownian motion to the incessant bombardment of molecules which he called "active molecules", not very far from Lucretius' description.

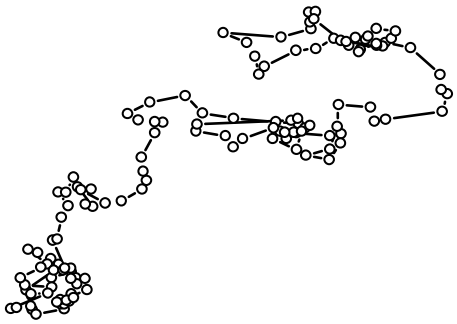

Figure 3.6: Motion of a particle undergoing Brownian motion. The circles represent consecutive particle positions at fixed time intervals. There is no correlation between consecutive particle movements.

Although the early intuition that the motion is generated by the continuous collisions with the molecules of the liquid is indeed correct, the highly erratic nature of Brownian motion has inhibited the development of a theoretical model for almost a century. In 1905, Albert Einstein finally solved the problem[40] starting from two basic assumptions:

1) The motion is caused by the exceedingly frequent impact of the molecules of the solvent on the diffusing objects.

2) The effect of the impacts on the suspended objects can only be described probabilistically.

If one takes a batch of identical particles suspended in a liquid, each of them is subjected to the same random force generated by the impact of the liquid molecules. The effect of this force on the motion of each individual particle leads to an "independent" random motion, uncorrelated to the motion of other particles. The motion of a single particle is not only independent from the motion of other particles, but the movements of the same particle at different time intervals are also:"*…mutually independent processes (as long as the time intervals are not taken too small)"*[40].

Let us define a time τ_c as the collision time between two subsequent collisions between the particle and a liquid molecule. Einstein understood that in order to model the Brownian motion statistical analysis is required. This means one should observe either many particles for a short time interval τ_s ($\tau_s > \tau_c$), or a single particle for a very long time ($\tau_l >> \tau_c$). The notion is essentially equivalent to assuming that the ergodic hypothesis is valid.

Einstein mathematically solved the problem for a particle diffusing in one-dimension (for details see Appendix). In this chapter, the two-dimensional form of the diffusion equation is used[41].

Einstein defines the term diffusion coefficient (D) and calculates it for a spherical particle with radius R:

$$D = \frac{k_B T}{6\pi\eta R} \qquad \text{Eq. 1}$$

known as Einstein-Stokes equation.

The diffusion of a particle in a liquid is solely dependent on the temperature of the liquid (T), viscosity of the liquid at T (η), and the radius of the particle (R). The diffusion constant D, as the velocity for constant motion, gives a measure of the amplitude of the mobility of an object. The higher the velocity or D, the more active the motion will be.

The problem of the particle motion is mathematically solved in two dimensions by[41, 42]:

$$f(r)dr = \frac{2r}{< r^2 >} \exp\left[-\frac{r^2}{< r^2 >} \right] dr \qquad \text{Eq. 2}$$

where *f(r)* represents the probability of a particle being at the position *r*, and $<r^2>$ stands for the mean squared displacement (MSD) of the diffusing particle (displacement with respect to a given starting position).

The solution of the diffusion equation in the two-dimensional form is[40]:

$$< r^2 >= 4Dt \qquad \text{Eq. 3}$$

Characteristic of Brownian motion is the linear time dependence of the mean square of the displacement, rather than the absolute displacement, as is the case for linear motion.

In general $<r^2> = 2dDt$, where d = dimensionality, giving:

$$d = 1 \rightarrow <r^2> = 2Dt$$
$$d = 2 \rightarrow <r^2> = 4Dt$$
$$d = 3 \rightarrow <r^2> = 6Dt$$

Einstein's mathematical solution was subjected to several criticisms. His starting assumption concerning the independence of the motion of each individual particle is valid as long as the time interval is not taken too small. Nevertheless, the solution is obtained by taking the time interval $\Delta\tau \rightarrow 0$. Still, Einstein's solution is considered the most satisfactory model. In order to emphasize the relevance of Einstein's approach, the diffusive motion must be introduced. Often, indeed, Brownian motion is associated to diffusive motion. They both describe the same thermally driven motion.

Ubiquitous are the examples of diffusive motion in physics, chemistry, biology, thus it is natural to consider diffusion as one of the fundamental processes by which materials move. Diffusion originates from the constant thermal motion of atoms, molecules and particles. Atoms or molecules concentrated in a small volume of a system will diffuse throughout the entire volume of the system in order to finally result in a constant concentration.

Fick's first law[43] (1855) describes the diffusion as dependent on concentration gradient.

$$J = -D\frac{\partial \phi}{\partial t} \qquad \text{Eq. 4}$$

J is the diffusion flux of a substance, and ϕ its concentration.

Fick first introduced and defined the term diffusion coefficient (D) as the proportionality constant between the molar flux driven by thermal motion and the gradient in the concentration of the species. Atoms or molecules of a constituent of a system move from volumes with high concentration to those with low concentration. The value of D is calculated by averaging over many molecules or

atoms. Even if the value of *D* is available, it is not sufficient in Fick's formula to fully characterize the motion of a single diffusive object.

Einstein's approach is radically new since, assuming the ergodic hypothesis is valid, he calculates *D* from the motion of a single particle. The erratic motion of a particle suspended in a liquid is the same motion performed by the molecules of the same liquid. Only the value of *D* is different since it is proportional to the size (radius) of the diffusing object. Brownian motion (macroscopic) and diffusive molecular motion (microscopic) represent the same process; the thermal motion of atoms and molecules.

Despite the fact that the term diffusion coefficient was not original, Einstein's approach radically changed the understanding of Brownian motion. A statistical method is required to characterize the motion of a single diffusive particle, since the irregularity of the motion no longer can be defined by a velocity term as in the classical case.

A different and more general solution of the Brownian motion problem has been found by Langevin in 1908[44]. Where Einstein's model is based on thermodynamics, Langevin based his model on pure mechanics. He considered the conservation of the mean kinetic energy, which equals thermal energy. Two forces are acting on a particle of mass m:

1) a steady dissipative drag force, opposing the motion, assumed to be the same as in the macroscopic case, that is $-m\gamma\frac{dx}{dt}$, with $m\gamma = 6\pi\eta a$, where η is the viscosity and *a* the particle diameter.

2) a fluctuating force (ζ) representing the incessant bombardment by molecules of the liquid.

By solving the equation of motion given by Newton's second law, Langevin arrived at the same solution as Einstein.

Any object suspended in a liquid is subject to the fluctuating force. Particles whose mass is such that the gravitational force is predominant, will sink and the overall motion will be mainly vertical. On the other hand, particles for which the Brownian force dominates perform a 'random walk' movement, which in principle will never cease. As it has been pointed out: *"…one of the most striking aspects of Brownian motion is the apparent tendency of the particles to dance about without going anywhere."*[45] This concept is mathematically written as Langevin did:

$< \zeta \cdot x > = 0$. It means that the net work done by the fluctuating force is zero.

Interesting in this second method is the identification of a fluctuating force, responsible for the random motion, with the term $< \zeta \cdot x >$ set to zero. It is possible

to evaluate the amplitude of the so called Brownian force[46] as $< |\zeta| >= \sqrt{12\pi\eta R k_B T}$.

As is clear from Eq. 1, the smaller the particle, the more its motion will become dominated by Brownian motion. This statement can easily be explained considering the two forces acting on the particle. The dissipative drag force is linear with the particle radius, while the fluctuating force varies as the square root of the radius. As the size of the particle becomes smaller and smaller the fluctuating force will become more and more predominant, and the resulting motion will appear more active.

In order to facilitate the understanding of Brownian motion, a direct comparison with linear constant motion is introduced. The differences between the two types of motion are illustrated in Figure 3.7 and Figure 3.8. The red and black curves in Figure 3.7 respectively show the trajectory followed in a linear and in a random motion in two dimensions (X-Y plane). Linear constant motion is represented by a straight line consisting of a succession of steps with equal amplitude. The trajectory illustrating random motion is formed by steps in random directions and with different amplitudes.

The linear motion is promoted by a force with constant amplitude and directed along the same direction. Therefore, if the force is balanced by friction, the time dependence of the displacement is linear and proportional to the velocity (m/s). If the applied force is fluctuating the directionality of the motion is not conserved and the linear time dependence of the displacement will be no longer valid. Brownian motion features linear time dependence of the average square displacement proportional to the diffusion coefficient D (m^2/s).

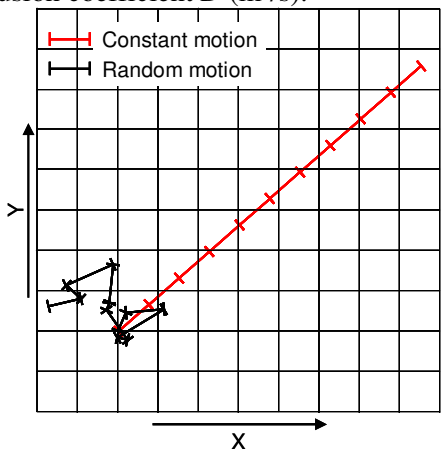

Figure 3.7: The red and the black lines shows respectively the trajectory followed in a linear and random motion in 2 dimensions. At fixed time-lag, constant motion presents steps of equal amplitude and along the same direction, while random motion displays steps with different sizes randomly oriented.

Figure 3.8 illustrates the stepsize (r) distribution for the linear constant motion and for Brownian motion.

Step-size is defined as the relative displacement of the object by its movement during a time interval τ. The graph is presented as the probability (Y-axis) vs. the step-size (X-axis). The constant motion consists of steps of constant amplitude; therefore the distribution of values of r is represented by a delta function (blue vertical line). In figure 7 the step-size has been given a constant amplitude of 1 μm.

In contrast to the linearly moving particle, a Brownian particle follows a trajectory consisting of steps of unequal amplitude. Thus the step-size distribution broadens. The distribution of r values for Brownian motion is described by Eq. 2. The black curve is obtained when particles are diffusing with D = 4.3 μm^2/s. The curve presents the highest probability for step-size ~ 1 μm, as for the case of constant motion. Nevertheless, a Brownian particle has a wider range of step-sizes, which are performed with decreasing probability the further they are from the 1 μm mean.

Several other curves are shown; each obtained with a different value of D. As D increases the step-size distribution broadens, with the probability maximum shifting toward higher values. D, similarly to the velocity, describes the mobility of a particle and gives a measure of how active the particle's motion is. A more active motion corresponds to a wider range of possible step-sizes. Figure 3.8 emphasizes the necessity of a statistical approach to describe Brownian motion. If a constant motion is completely characterized by a single step-size value, for Brownian motion a distribution of values is needed.

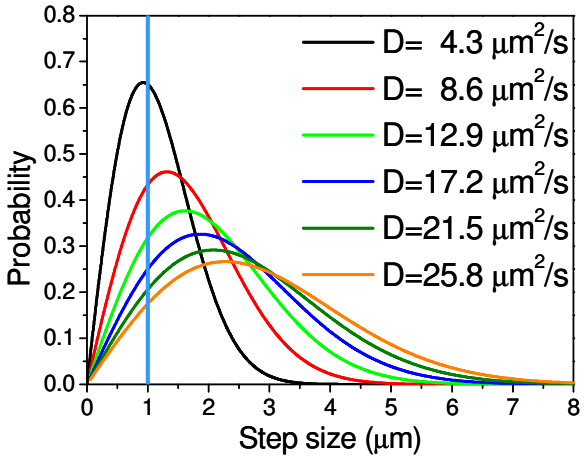

Figure 3.8: Stepsize distribution of constant motion (blue vertical line) and Brownian motion having different D values (4.3, 8.6, 12.9, 17.2, 21.5, and 25.8 μm^2/s). The curves used to model the stepsize distribution in case of Brownian motion are obtained with Eq. 2.

3.3.2 Experimental evidence of Brownian motion

In this general introduction, the step-size distributions are pictured while varying the diffusion constant. The curve is obtained by fixing the value of D and calculating the corresponding probability distribution. The experimental approach to measure the diffusion of particles works in the opposite way. The amplitude of r is measured at a great number consecutive fixed time-lags, after which the performed step-sizes are represented into a statistical distribution. By using Eq. 2 to model the experimentally obtained distribution, one can extract the value of $<r^2>$ and thus the diffusion coefficient D using Eq. 3. The displacement of particles is measured in two dimensions, so the equations describing the motion (Eq. 2 and 3) are used in the two-dimensional form.

As it has been shown, Eq. 2 characterizes the step-size distribution of a diffusing object, but it does not give any information concerning the direction of the motion. Random motion is so defined because of its erratic direction. The solution of the diffusion equation (Eq. 3) describes the average mean squared displacement of Brownian particles as linear with time, while for a linear constant motion the displacement is linear with time.

In order to highlight the implications concerning the random orientation of the motion let us consider a batch of particles diffusing in a liquid, in the usual Brownian condition, but let us assume the liquid to drift at a constant velocity. This example could be expressed mathematically by correcting the Langevin's condition. For pure Brownian motion, he assumed $<\zeta \cdot x> = 0$, where ζ is the fluctuating force. The mean value of the net work is set to zero.

If an additional force (ξ), although weak, generated by the drift motion of the liquid acts on the particles, it will modify Langevin's expression into $<\zeta \cdot x + \xi \cdot x> \neq 0$. If the drift force is assumed to be small, it might slightly effect the step-size distribution that could still be erroneously associated to a random motion. As a matter of fact, the net overall motion will gain directionality and the MSD will lose the linear time dependence.

Thus, in order to fully characterize the Brownian motion, a law concerning the orientation of the motion is required. Einstein's solution is written in Eq. 3:

$$< r^2 >= 2dDt$$

as mentioned, d = number of dimensions of the motion. Figure 3.9 compares the linear MSD time dependence of Brownian motion obtained with six different values of D to the MSD of linear motion used once again for comparison.

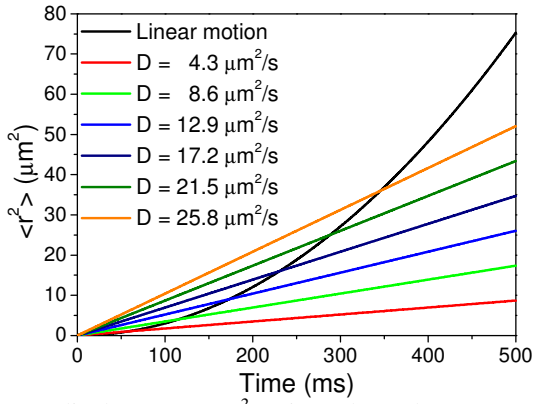

Figure 3.9: Mean square displacement $<r^2>$ time dependence curves having different values of D and (black curve) MSD t-dependence of linear motion.

A particle performing a linear and constant motion will always increase its displacement from a point origin r_0 and the time dependence of the displacement grows linearly with time ($r = v \cdot t$). Consequently, the squared displacement curve goes as the square of the time (black curve in Figure 3.9).

On the other hand, as depicted in Figure 3.7, in a random motion it is not certain that a particle will always move far from the point origin r_0. The randomly oriented motion could result in a particle going far and back to the r_0 position. On average though, the Brownian particle does accumulate a displacement. The average displacement $<r>$ performed by a Brownian particle does not depend linearly on time, but as the square root of time.

$$< r >= \sqrt{2dDt}$$
$$\downarrow$$
$$< r^2 >= 2dDt$$

The statement made by Nelson[45] (apparent tendency of Brownian particles to dance around without going anywhere) might be reformulated by saying that Brownian particles simply need more time to go anywhere.

Similar to the step-size distribution analysis, a linear time dependence of the MSD alone cannot fully prove the motion to be Brownian. For instance, a particle in linear motion through a medium with viscosity gradients could present a linear time dependence of the MSD, but a non-Brownian distribution of step-size.

The characterization of the features of Brownian motion (step-size distribution and MSD) is crucial in the study of self-propulsion at the nanoscale. The catalytic action might promote a deviation from pure Brownian behavior in either the step-size distribution or the MSD time-dependence.

How can we obtain experimental access to the step-size distribution and the MSD of the objects under investigation?

The diffusion of individual particles can be observed using the single particle tracking technique and characterized by the analysis of the particle trajectories. Single particle tracking is usually associated to the optical detection of individual particles using laser or bright field microscopy[28, 29]. The most direct method of studying particle diffusion is based on the analysis of a succession of microscope images (movie) of highly diluted samples. The high dilution is required in order to avoid scattering between diffusing particles, and in order to facilitate the tracking of individual particles.

In such a movie the optical signal of a diffusing particle consists of a pattern that changes from frame to frame. If the particle has a size smaller than the wavelength of the emitted light, the pattern is diffraction limited and is called the Point Spread Function (PSF). A two-dimensional Gaussian function can be used to approximate the PSF, and therefore determine the position of the particle beyond the diffraction limit[47, 48].

By tracking the position of the PSF in each of the consecutive frames of the movie, it is possible to recover the trajectory of a single particle. The analysis of such trajectories is known as single particle tracking. The latter is a powerful technique because it directly probes the motion of particles in space and time, providing the capability to unravel the nature of the motion, from purely diffusive to highly directional.

The main limitation of the technique is its low sensitivity to fast processes. The accuracy in the positioning of the tracked particles scales as the square root of number of the detected photons[47] (more photons → better information → smaller error). A poor accuracy may lead to erroneous analysis; therefore high photon count is preferable. At the same time, the faster the motion, the higher should the frame rate be in order to avoid blurring of the particle pattern. Thus, it is necessary to balance the frame rate with the photon count.

Figure 3.6 depicts the typical outcome from tracking a single diffusing particle. It resembles the 2-dimensional trajectory, or path, described by the moving object, consisting of positions (circles) taken at fixed time intervals. From the trajectory it is possible to extract the step-size at a given time-lag, and the time-dependence of the displacement from the starting position.

By recovering the trajectory of multiple individual particles, is also possible to determine the statistical ensemble behavior. The step-size distribution curve consists of the sum of the distributions from several particle trajectories. The MSD curve is the average value obtained by the single particle curves. All step-size distributions depicted in this chapter are constructed based on more than one thousand steps performed by several moving particles, while the MSD curves correspond to the average values from ~30 particles.

3.4 Single particle tracking of catalytically active nanoparticles

Catalysts–based engines have shown their potential toward particle self-propulsion when applied at bigger (μm) scales[20, 21]. As we have seen, there are two proposed mechanisms of propulsion: bubble-formation[20, 24] and interfacial concentration gradients[21]. The latter has been observed in bi-metallic particles having size of a few micrometers and it has been related to the catalytic activity occurring non-homogeneously on the particle surface. The solid background provided by the examples at micro-scales in terms of achieved propulsion and understanding of the process project the interest toward the nanometer scale.

The current project's goal is to gauge the effect of catalytic reactions occurring on the surface of nanoparticles, whose motion is normally purely diffusive.

Will the catalytic conversion of chemical energy by a monometallic nanoparticle be able to generate the conditions required to attain self-locomotion at the nanoscale level also?

And will it be possible to detect such propulsion on top of the Brownian motion of the particles?

To investigate this, we will monitor bi-functionalized silica nanoparticles labeled with a layer of catalase mimic molecular complexes, which perform hydrogen peroxide decomposition at the molecular scale. Detailed characterization of the motion of bi-functionalized silica nanoparticles and metallic nanoparticles at the single particle level is presented.

In order to provide evidence for the efficacious action of the catalytic particle propulsion, we first introduce micro-scale particles performing the same catalytic reaction.

3.4.1 Bi-functionalized silica microparticles

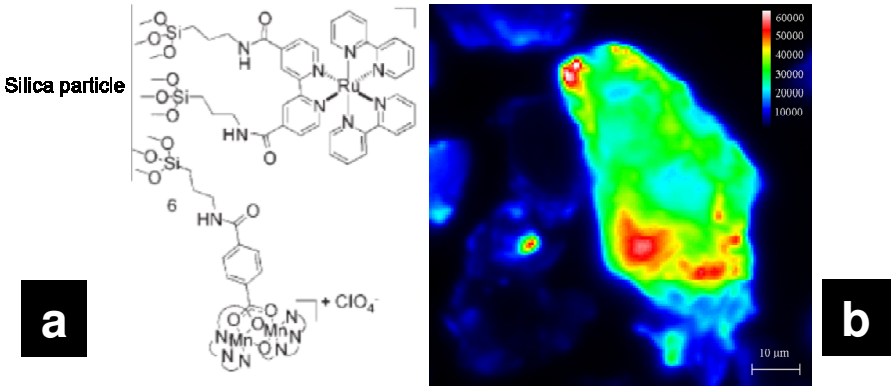

Figure 3.10: Schematic of surface-bound ruthenium complex (luminophore) and manganese catalyst from Ref [26] (a). Observation of the bi-functionalized silica micro-particles in a wide field fluorescence microscope (b).

The advantages of the bottom-up approach taken by Feringa *et al*. in the design of molecular complexes that convert chemical energy into motion, can be easily extracted from the exemplary system represented in Figure 3.10.[25, 26] The surface of silica microparticles is bi-functionalized, being covered with both catalase mimic complexes, used as engines for self-propulsion, and specially designed luminophores for fluorescence imaging (details are given in ref. 26).

The schematic of the system illustrates the potentiality of the bottom up approach. The surface of particles is modified in order to furnish it with the tools needed for both autonomous motion and for the detection thereof.

A dispersion of silica microparticles (20 – 60 μm) in acetonitrile (CH_3CN) is studied when a 5 % solution of H_2O_2 (the fuel of the catalyst-engine) is added. Upon addition of the catalyst-fuel, both rotational and translational motion driven by the release of bubbles is observed. The asymmetrical distribution of the reaction product (oxygen) due to the asymmetrical geometry of the particles leads to propelled motion. Particles are observed to propel away from the site where bubbles are formed, suggesting the same propulsion mechanism as described by Whitesides[20]. Figure 3.11 depicts a time-lapse of the rotation of such a bi-functionalized silica particle imaged with fluorescence microscopy.

The possibility to label the particle surface with the luminophore molecules enables observation through fluorescence microscopy, which is a valuable technique due its highly improved signal-to-noise ratio with respect to bright field microscopy.

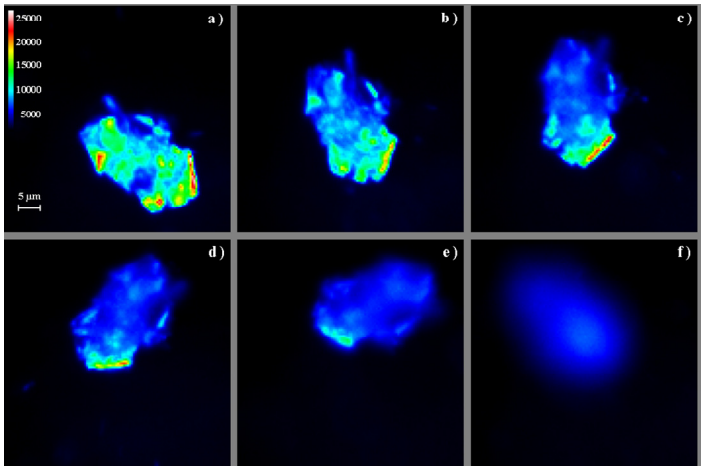

Figure 3.11: Rotational movement of bi-functionalized silica microparticles at a) 0 s, b) 1.25 s, c) 2.5 s, d) 5 s, e) 7.5 s, f) 12.5 s (average rotational speed ~0.24 rad s^{-1}). The total size of each of the images is 50 x 50 μm.

The luminophore employed should meet several criteria: i) It must be robust towards the chemical fuel used (i.e. H_2O_2); ii) it should be functionalizable to enable its covalent attachment to the particle surface, and iii) it should have a

suitable excitation and emission wavelength. Absorption and emission spectra of the ruthenium-based luminophores used in our study is shown in Figure 3.12. The relatively low fluorescence quantum yield (~4 %), obtained using the 488-nm line of an Ar^+-ion laser as excitation, is compensated by the great number of luminophores on the particles surface.

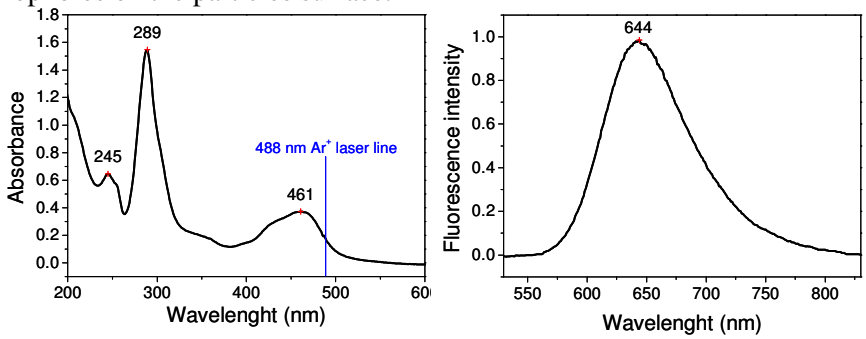

Figure 3.12: Absorption (left) and emission (right) spectra of the ruthenium-based luminophore in acetonitrile (CH_3CN).

The catalytic activity of synthetic molecular motors has shown propelling potential similar to the motion induced by noble metals.

3.4.2 Bi-functionalized silica nanoparticles

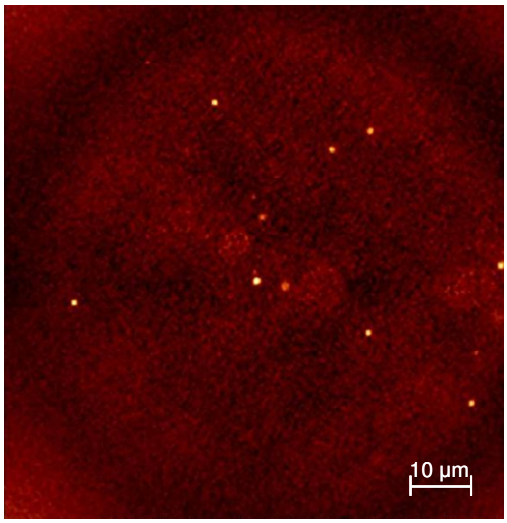

Figure 3.13: Image of the diffusing bi-functionalized silica nanoparticles obtained with fluorescence microscopy. The motion of the particles has been studied in bulk solution in order to avoid a potential surface influence to the particle motion (the axial focus of the excitation beam was approximately 100 µm above the glass substrate).

Spherical silica nanoparticles (average radius ~290 nm) labeled with synthetic molecular motors represent an attempt towards self-propelling nanomachines. The schematic of the system using spherical nanoparticles is similar to the one describing silica microparticles in Figure 3.10. The fabrication of the nanoparticles followed the standard procedure described in the literature[49]. Molecular motors and luminophores were homogeneously distributed on the particle surfaces, in a number ratio of 10:1. Figure 3.13 shows an image, obtained with fluorescence microscopy, of particles freely diffusing in the solution.

3.4.2.1 Results

Figure 3.14 compares the step-size distribution (200 ms time-lag) and the MSD of 290 nm-radius particles diffusing in pure ethanol (a and b) and in a solution 1 % rich of H_2O_2 (c and d), respectively.

The step-size distributions were modeled using Eq. 2, from which respective values of D = 0.7 $\mu m^2/s$ (a) and D = 0.68 $\mu m^2/s$ (c) were extracted. The obtained values of D result in agreement with the theoretically expected value of the diffusion coefficient (Eq.1) for particles with radius 290 nm diffusing in ethanol ($\eta = 1.08 \times 10^{-3}$ Pa·s) at room temperature.

Graphs b and d present the average MSD (data points) curves together with the dispersion bars (dispersion (σ) $= \sqrt{< x_i^2 > - < x_i >^2}$, where x is the square displacement). The MSD curves show linear time dependence which can be modeled by Eq. 3 to extract the value of D (D = 0.68 $\mu m^2/s$ for b, and D = 0.63 $\mu m^2/s$ for d) consistent with the values extracted from the step-size distribution analysis.

The analysis of the particle motion performed in an environment rich of hydrogen peroxide (Figure 3.14 c and d) unambiguously supports the conservation of the purely diffusive behavior of the nanoparticles in the presence of catalytic activity. Furthermore, the value of D seems to be fairly insensitive to the catalytic activity occurring on particles surface.

The catalytic conversion of reactants (H_2O_2) into H_2O and O_2 promoted by the molecular complexes, as supported by the study at micro-scale, does not affect the thermal diffusion that is dominant at the nanoscale. Although not directly observable from microscope' images, the reactions are assumed to take place. The labeling procedure of silica nanoparticles follows the same protocol used for silica microparticles where the oxygen bubble formation is directly related to the H_2O_2 disproportionation reactions.

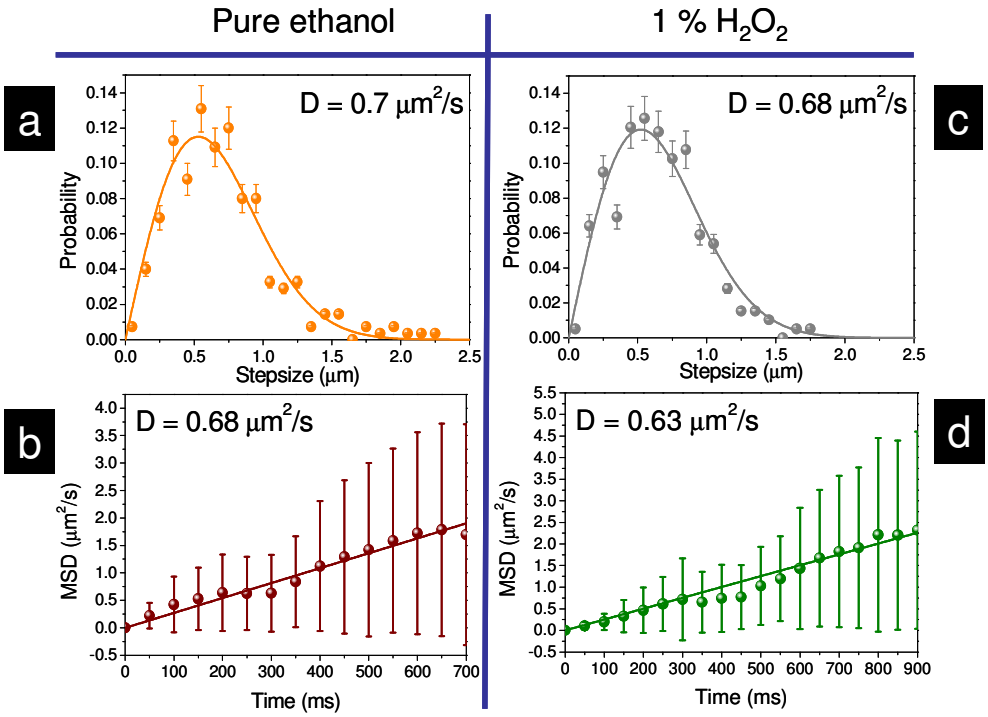

Figure 3.14: Step-size distributions (Δt = 200 ms) (a, c) and MSD time dependence (b, d) of tracked particles in pure ethanol and in a 1 % H_2O_2 ethanol solution. The model curves in a and b are obtained by using Eq. 2, while in b and d Eq. 3 was used for modeling. The bin-sizes used in a and c are 0.1 μm.

3.5 Metal nanoparticles

Noble metals, owing to their high efficiency in the disproportionation of hydrogen peroxide, have been extensively used to power self-propulsion at micro-scales[20-22, 24]. In this section, like in the last, we first document the surface catalytic action and its effect on micro-size particles, in an effort to reproduce the results presented in literature. Propelled motion is obtained through bubble-release by large particles (size > 10 μm) or particle-clusters. In smaller particles (size ~2-3 μm), the motion observed is not promoted or driven by bubbles formation.

Second, we will investigate potential propelling of metallic nanoparticles tested at the nanoscale. Gold nanospheres (radius 44 nm) and platinum nanorods (75 x 25 nm) are studied while diffusing in a water solution enriched with hydrogen peroxide.

3.5.1 Platinum microparticles

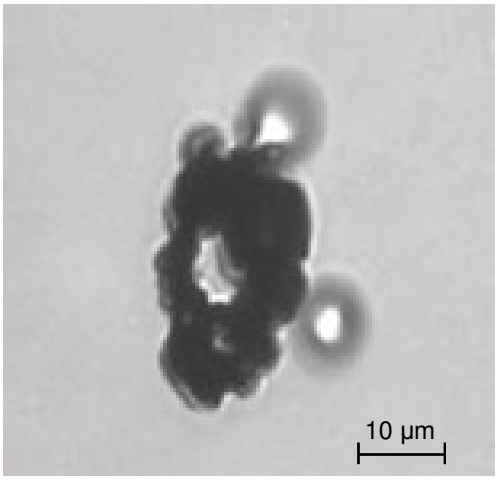

Figure 3.15: Aggregate of platinum particles imaged using bright field microscopy. The particles are immersed in a 25% hydrogen peroxide solution in water. The observed release of oxygen bubbles directly shows the catalytic decomposition of H_2O_2 into H_2O and O_2, driven by Pt.

The motion of platinum particles (size: few µm up to tens of µm) dispersed in a 25% aqueous solution of H_2O_2 has been studied in order to enlighten the phenomenology involved in the bubble-propelled motion.

Because of the relatively big size of the dispersed Pt particles, white light microscopy has been used in combination with a 60x microscope objective. A quantitative analysis appeared beyond the possibility of the sample, because the broad size and shape distribution of the particles precluded a general uniform description. Despite this limitation it is possible to outline a few phenomenological insights.

Due to the high density of platinum (21.45 g/cm^3) and the size of the single particles (> 2 µm), a strong sedimentation process occurs, causing the single particles and aggregates to sink onto the glass surface used as substrate.

Figure 3.15 shows a cluster of platinum particles and the release of oxygen bubbles, proof of the catalytic activity. Despite the bubble formation, the aggregate does not show any evidence of autonomous motion. The absence of movement could be due to the strong interaction between the metal and the glass surface.

The erratic behavior of particles, which precludes a quantitative analysis, is documented in Figure 3.16. Images, taken at 50 ms time intervals, show two aggregates, both generating bubbles. If the top left particle is in a fixed position, as the particle depicted in Figure 3.15, the second aggregate is clearly moving. The trajectory of the second particle-aggregate is highlighted by indicating its position in each image. Bubbles are distinctly visible and their position on the moving

particle support the propelling mechanism described in previous paragraph[20]. The propelled object is again pushed away from the region where the product concentration (oxygen) is higher. It is possible to distinguish the "front" of the particle from the "back", where the bubbles are released. Intuitively, the concept of front and back implies the notion of directionality. The asymmetrical shape of the particle suggests that the catalytic activity results in an asymmetrical distribution of reaction products, hence achieving a sort of directional motion.

The opposite behavior exhibited by the two aggregates in Figure 4.16 highlights how strongly the particle-surface interaction can affect the motion.

Figure 3.17 depicts a time-lapse (time intervals 50 ms) of the motion of a ~3 μm single particle. The shape and observed rotational motion of the particle recalls the aforementioned hemycilindrical plates. However, the big difference here is that no bubble formation is observed.

In Figure 3.18 (time interval 250 ms) a similar rotational motion is performed by a smaller particle having almost the same geometrical shape.

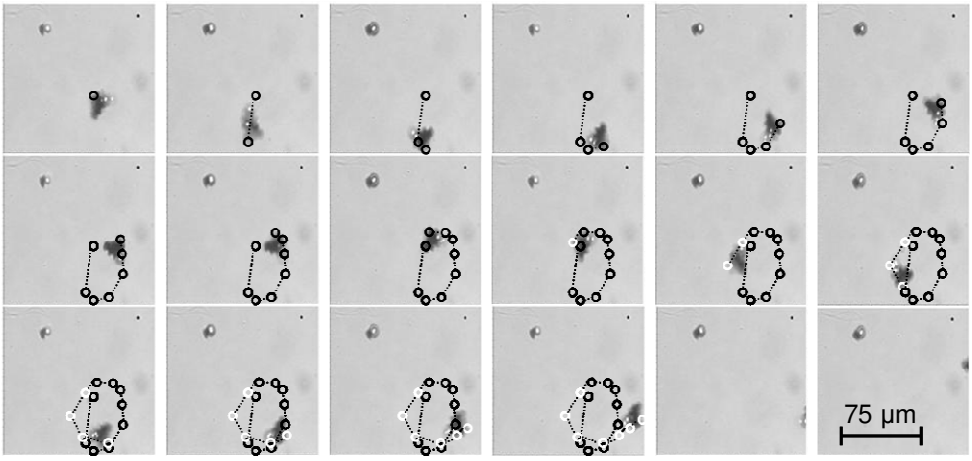

Figure 3.16: Images of aggregates of Pt particles at the glass surface are taken at a 20 Hz rate. Both the particles release oxygen bubbles, but only one undergoes propelled motion. The latter particle moves away from the area where the bubbles are formed. The motion of the moving object is illustrated by the trajectory, which is indicated in the consecutive images.

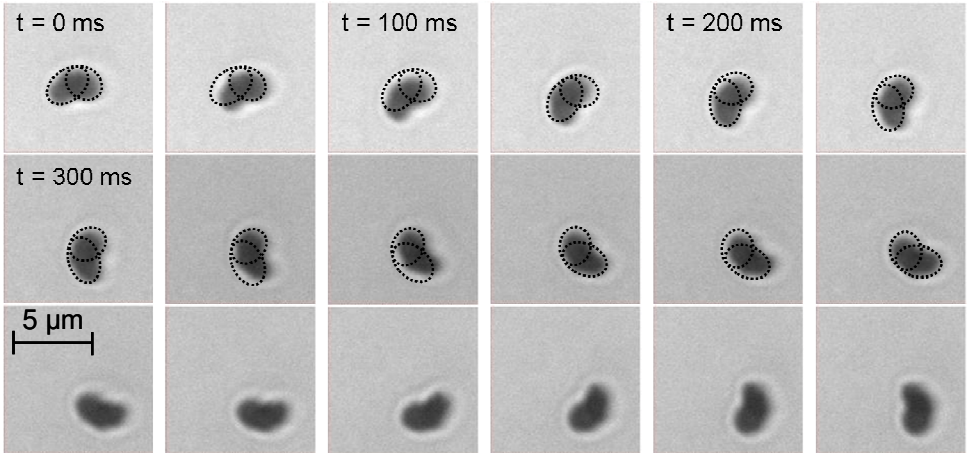

Figure 3.17: Images of a ~3 µm-sized Pt particle at the glass surface, taken at a 20 Hz rate. The particle performs rotational motion without release of oxygen bubbles.

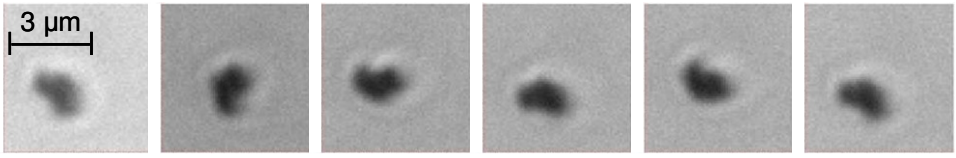

Figure 3.18: Rotational motion of a ~2 µm-sized Pt particle undergoing rotational motion on glass surface. Images are presented with time interval of 250 ms (time increasing from left to right).

As emphasized by the sketch in Figure 3.17, it is interesting to notice that the direction of the rotation occurs in both cases toward the same side of the particle. The absence of bubble formation together with the rotational motion could mean that a different propulsion mechanism is responsible for the autonomous motion here.

Figure 3.19 shows another three particles imaged at different times, along with the analyzed trajectory of particle 3 in the 15 second time. The trajectory consists of the positions of the moving particle in 300 consecutive frames, recorded at a rate of 20 Hz. The movie under investigation, from which the images are extracted, has been taken "dynamically", meaning that the solution of hydrogen peroxide was added to the starting solution (pure water) during the recording time, in order to document possible differences in the behavior of the same particles in absence and in presence of H_2O_2.

The top left image (t = 0s) corresponds to the first frame of the movie. Three particles immersed in water are visible, each resting on the glass substrate surface. In the second image (t = 9.6s), the position of the particles is still unchanged, as depicted in the trajectory of particle 3. Particles in pure water do not move. Images corresponding to 9.65s < t < 9.85s are not shown since documenting the two particles flowed away to different positions as a consequence of adding the solution

with hydrogen peroxide. This drift motion due to the mixing of the water and H_2O_2 solutions has been completely arrested at the time of the next image shown, at t = 9.9s.

Hereafter, particle 1 and 2 rest still on the surface, while particle 3 is observed to start movement, absent before, displayed in the last (red) part of the trajectory. The time interval covered by the movie (15s) makes it possible to distinguish three distinct stages (phases) in the behavior of particle 3. The first phase (0s < t < 9.6s), covering a time interval of more than 9 seconds, shows the particle virtually stuck in the same position, presumably due to a strong interaction with the glass substrate. In the time interval 9.65s < t < 9.9s (phase 2), the motion is not reported, but consists of the fast and unidirectional motion due to the induced drift of the liquid upon addition of the hydrogen peroxide solution.

At t = 9.9s the drift motion is arrested and the particles are finally immersed in a H_2O_2 rich solution. From t > 9.9s (phase 3), particle 3 is observed to move across the glass surface, and the trajectory is measured and presented. This type of particle motion is only observed when the catalytic reaction can take place (when the catalytic fuel is present). Assuming the catalytic reaction occurring, no bubble formation is observed. Once again (see Figure 3.17 and Figure 3.18), the size of the particle appears to be too small to enable the nucleation of gaseous bubbles.

It is not possible to directly and undoubtedly link the motion of particle 3 to catalytic propulsion, but the difference with the behavior observed in pure water (0s < t < 9.9s) is unambiguous.

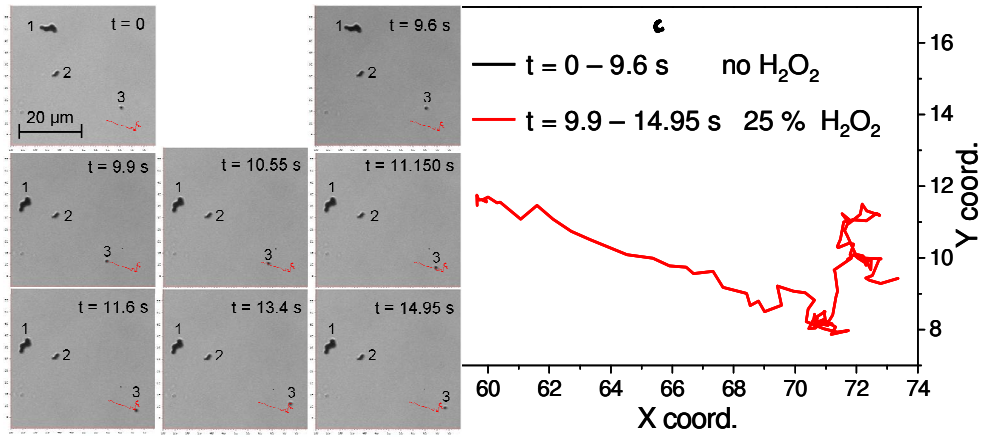

Figure 3.19: Images (integration time 50 ms) extracted from a microscope movie covering a time interval of 15 s. Three Pt particles (1, 2, and 3) immersed in pure water and initially resting on the glass substrate surface are observed. The successive of images document the different behavior of particle 3 upon hydrogen peroxide addition. The first two images (time interval > 9s) show the three particles immobile on the surface (phase 1). Between 9.6s and 9.9s the H_2O_2-rich solution is added, and a drift motion of the particles is observed

(phase 2), until they come to rest once more at t=9.9s. From t=9.9s on particle 3 is observed to move, its trajectory indicated by the red line in the graph on the right (phase 3).

As mentioned at the beginning of the paragraph, no quantitative analysis is possible due to the lack of homogeneity of the sample. Nevertheless, some examples of propelled motion have been observed (Figure 3.16), supporting the mechanism of propulsion proposed by Whitesides[20]. The rotational motion presented in Figure 3.17 and Figure 3.18, if related to the catalytic activity, could suggest a different propulsion mechanism since no bubbles are observed, as suggested by Paxton *et al*[21].

The case documented in Figure 3.19 is more complex. In fact, the behavior of particle 3 changes when hydrogen peroxide is added, and the particle moves autonomously showing some features of directional motion highlighted by the trajectory.

This paragraph aims at showing the catalytic activity of platinum particles when immersed in a hydrogen peroxide-rich solution. Direct proof of the catalytic activity is the observation of oxygen bubbles generated by particles having size > 5 μm and the following driven motion.

For particles of smaller size bubbles formation is inhibited by the reduced oxygen production which prevents bubble nucleation. Nevertheless, features of catalytically driven motion are still visible even for particles of a few micrometers size.

The particles exhibit a strong sedimentation process, suggesting gravity to be the dominant force governing their motion. Each of the particles in this section, as in the case reported in ref. [22], has been imaged on the glass surface.

The examples depicted in Figure 3.16 and Figure 3.19 showed particles behaving differently despite the occurrence of catalytic decomposition of the H_2O_2 fuel in both cases. For some particles, the formation of oxygen bubble proves to be ineffective in propelling motion, most likely because of the strong particle-surface interaction (see Figure 3.15 and Figure 3.16).

The batch of platinum particles, though a simple system, resembles many of the points outlined in literature. Still, the particles are rather unaffected by Brownian force suggesting strong gravitational and particle-substrate interactions to be the dominant forces acting on the particles.

The effectiveness of catalytic agents in propelling movement in metallic nanoparticles that are purely diffusing in liquid is still to be proven.

3.5.2 Gold nanoparticles

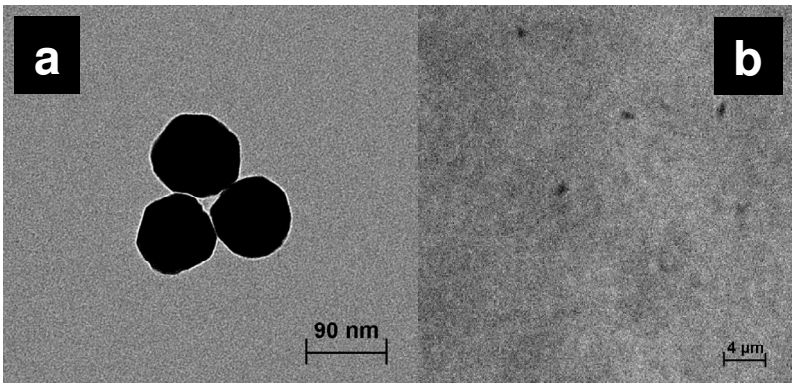

Figure 3.20: Electron microscopy image of gold nanoparticles (a). Bright field microscopy image of gold nanoparticles diffusing in water (b).

The diffusion of spherical gold nanoparticles of radius ~45 nm was studied both in pure water and in an aqueous solution of H_2O_2 (25%). Single particle tracking has been used to recover the trajectories of individual particles. The reduced size of the particles prevents the sedimentation effect, and therefore the motion, studied in the liquid at 100 µm above the glass substrate, is purely Brownian. The experimental method is similar to the one described for the case of bi-functionalized silica nanoparticles in section 3.4.2. The major differences are the use of bright field microscopy instead fluorescence microscopy and the particles being purely metallic in this case. A 60x microscope objective was used, and images were taken at a 40 Hz frame rate for particle diffusion in pure water and at a rate of 33 Hz in the presence of hydrogen peroxide.

Eq. 3 allows for the calculation of the theoretically expected diffusion coefficient, which is $D = 4.4\ \mu m^2/s$ ($R = 45$ nm, $\eta = 1x10^{-3}$ Pa·s at $T = 25°C$) for 45 nm radius gold nanoparticles. As for silica nanoparticles, the aim is to document possible deviations from the purely Brownian motion induced by the catalytic reaction.

Figure 3.21 compares the step size distribution (300 ms time-lag) and the MSD of 45 nm-radius particles diffusing in pure water (a and b) and in a 25 % aqueous solution of H_2O_2 (c and d). Step-size distributions can be modeled by using Eq. 2, from which the values of $D = 4.3\ \mu m^2/s$ (a, c) are extracted for both cases. In each case, the experimentally obtained diffusion constant is in very good agreement with the theoretical expectation value for purely diffusional motion. Graphs b and d present the average MSD (data points) curves.

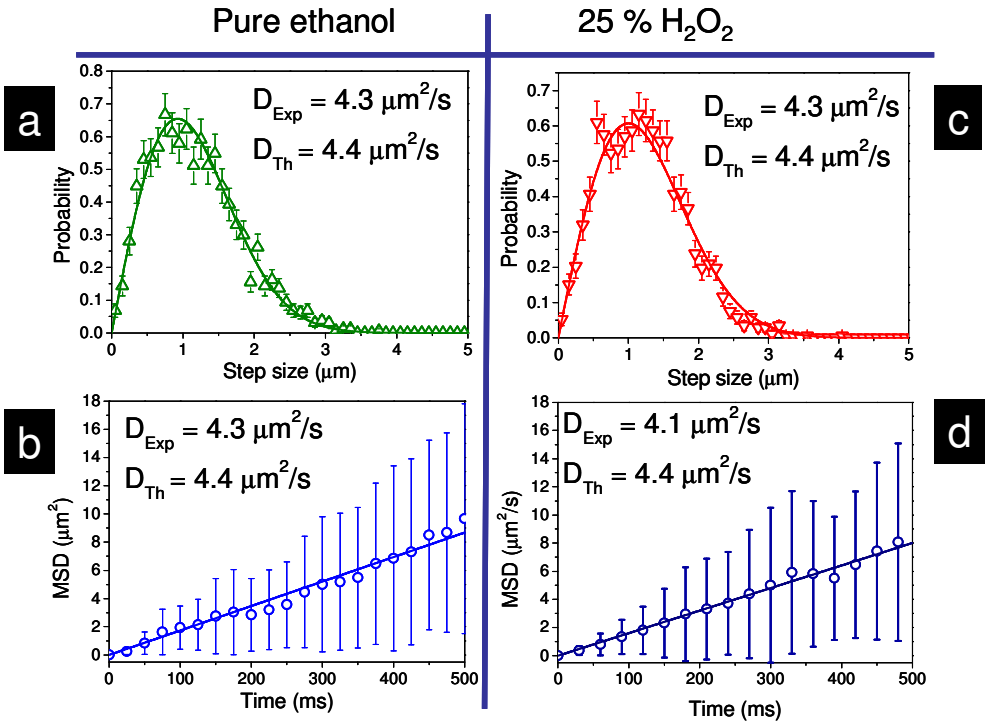

Figure 3.21: Step-size distributions (Δt = 300 ms) (a, c) and MSD time dependence (b, d) of tracked particles in pure ethanol and in a 25 % aqueous solution of H_2O_2. Model curves in a and b are obtained using Eq. 2, while in b and d Eq. 3 was used for modeling. The bin-sizes used in a and c are 0.1 µm.

To support the consistency of the result, the analysis of the mean squared displacement (Figure 3.21 b and d) of the tracked particles was performed. Eq. 3 was used to model the MSD time dependence (blue lines). The observed linearity underlines the Brownian nature of the observed motion, and the slope of the curve allows the estimation of D = 4.3 µm²/s (b) and 4.1 µm²/s (d), in agreement with the step-size analysis. The motion performed by particles is purely Brownian and D is not affected by the catalytic activity.

A control test concerning the value of D has been done using electron microscopy imaging and dynamic light scattering, in order to have direct access to the particle-size. Figure 3.20 shows the image of gold particles taken with electron microscopy. Here, the measured radius is in agreement with single particle tracking results. The same outcome is achieved by light scattering control measurements. The value of D measured with dynamic light scattering is D = 4.8 µm²/s in pure water, and D = 4.77 µm²/s in a 10% H_2O_2 solution. The small difference in the absolute value of the extracted diffusion constant, if compared to the theoretical value (4.4 µm²/s), could be due to temperature mis-calibration of the apparatus

(wrong temperature → wrong viscosity coefficient). Nevertheless, the final outcome supports the previous measurements: no propelled action, or deviation from purely diffusive motion, is observed.

The analysis of the motion of gold nanoparticles in the presence of hydrogen peroxide shows that the catalytic activity is unable to deviate the particles from pure Brownian diffusion.

3.5.3 Platinum nanorods

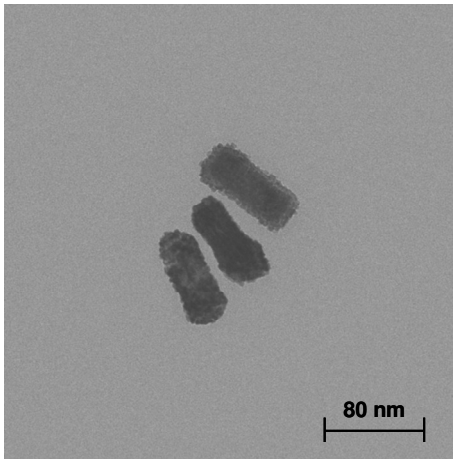

Figure 3.22: Electron microscopy image of Pt nanorods.

As well as spherical gold nanoparticles, platinum nanorods, of approximately 25x75 nm size, were investigated. Platinum particles, being more active in the decomposition of H_2O_2 than gold particles, have a big advantage in terms of propelling potential. Figure 3.22 shows the rod-like shape of particles in an electron microscopy image.

As mentioned, the main limitation of the single particle tracking technique is its low sensitivity to fast processes. Unfortunately, platinum rods diffuse with such a high *D* value, that white light microscopy cannot resolve the motion. Low signal-to-noise ratio prevents the observation of particles and single particle tracking is inaccessible.

Instead, dynamic light scattering was performed in an aqueous solution of hydrogen peroxide, again showing no significant deviation from the diffusion in pure water. The non-spherical shape of rods might affect the absolute value of the diffusion coefficient, nevertheless the average values obtained (D = 11.6 $\mu m^2/s$ in pure water and D = 12 $\mu m^2/s$ in 10 % H_2O_2) confirms the absence of clear deviation from purely Brownian diffusion.

Once again the analysis of the motion of metallic nanoparticles shows that the catalytic action of metals is not able to overcome Brownian diffusion at the nanoscale.

3.6 Discussion

The aim of documenting the self-propelling action by nanoparticles, which motion is strongly affected by thermal diffusion, has demanded an approach capable of fully characterizing and recognizing Brownian motion features. Obtaining step-size distributions and performing MSD analysis has required scrupulous work. By modeling the measured distribution and time dependence of MSD, it is possible not only to recognize Brownian motion, but also to provide quantitative data concerning the diffusional motion. Figure 3.23 illustrates some of the terms that the sensitivity of the technique must satisfy. Graphs a and b regard the dispersion of values in the MSD time dependence analysis, while graphs c and d show the term Chi squared (χ^2) in the fitting procedure of the step-size distribution with Eq. 2.

The dispersion term ($\sigma = \sqrt{< x_i^2 > - < x_i >^2}$), where x is the displacement of a single particle (i = particle index), gives access to investigate an intrinsic property of the ensemble of measurements from which the MSD is calculated. Theory predicts MSD – σ and MSD + σ to be equal to zero and twice the calculated MSD, respectively. In graphs a and b the red lines (experimental values) look consistent with the green lines (theoretical expectation of MSD ± σ).

In the bottom part of Figure 3.23, the focus of the discussion is on the error made (χ^2) by fitting data points with the applied model (Eq. 2). Graph c shows data points (green triangles) and the corresponding best fit (green line). The two red lines are obtained by varying the experimentally obtained diffusion constant by +20% and -20%, respectively. Panel d shows the corresponding trend of χ^2 as the percentual deviation from the best-fitting D is varied. An increase/decrease of 20% in the value of D corresponds to a doubling of χ^2.

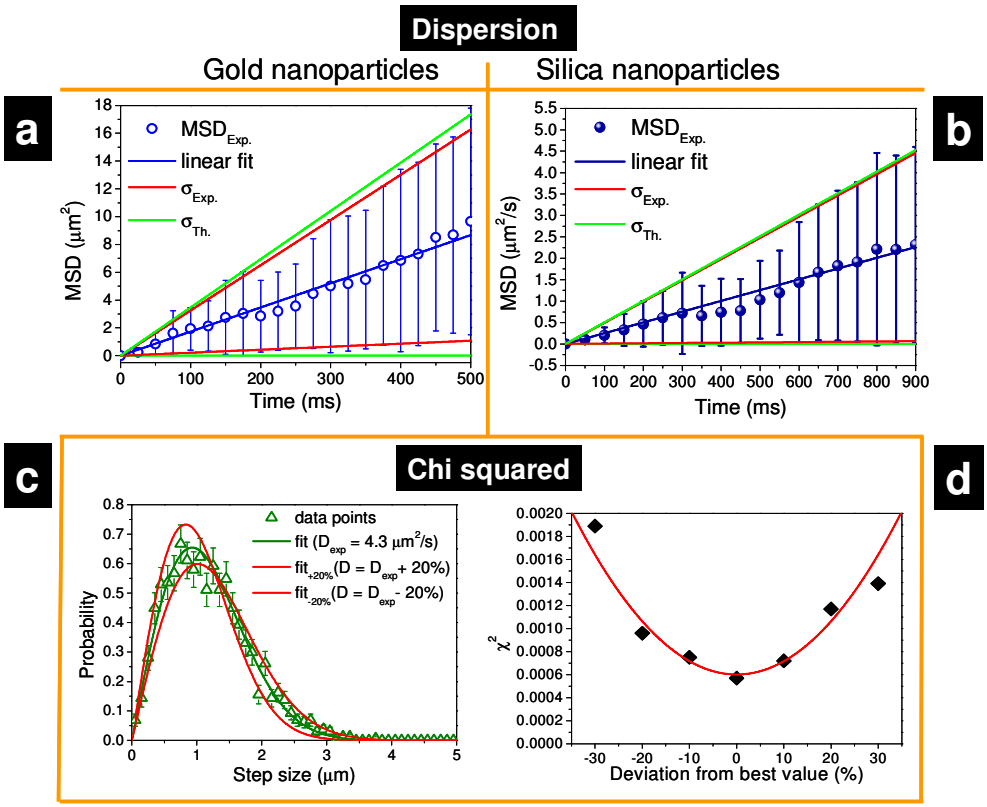

Figure 3.23: Graphs a and b show the dispersion of experimental data used to calculate the MSD time dependence. Red lines, corresponding to the experimental values, are consistent with the theoretical expectation (green lines). Graph c illustrates the fit of a stepsize distribution, obtained by using Eq. 2. Here, the green curve represents the best fit, while the two red curves represent fits obtained by fixing the diffusion constant to the best-fitting D value ± 20%. Panel d shows the dependence of χ^2 as the value of D is changed. By adding/subtracting 20 % from the best value of D χ^2 doubles.

The systems studied (bi-functionalized silica nanoparticles and metallic nanoparticles) have two main differences if compared to examples in literature: reduced size and more homogeneous release of oxygen. Nanoparticles represent the most challenging attempt in the quest for self-propulsion. Despite the difficulties in the bottom-up approach of synthetically designing a self-propelling nanoscale machine, nanoparticles represent the first system in which the propelling action has to face directly the Brownian force.

Bi-metallic micro rods[21] are the smallest machine in which catalytic motors were observed to successfully propel the objects. However, these rods are so heavy that they tend to sink the bottom of the cell. The density of metallic particles with such dimensions causes gravitation to be the dominant force in their motion. Only

in one case propelling action was observed for a particle resting on the substrate surface. In this case, catalytic propulsion was shown to enhance the directionality in a quasi-Brownian motion performed on the surface. Noteworthy as well, is the strong influence of the surface-particle interaction.

In contrast, the motion of silica nanoparticles and metallic nanoparticles is only affected by the Brownian force, which is further strengthen by the reduced size of these particles. A second crucial point in these cases is the absence of the factors that have been proposed as the origin of the self-propulsion; bubble formation and the interfacial concentration gradients.

Bubbles are observable only if the size of the particle is sufficient to allow for the production of oxygen in large enough quantities to induce bubble nucleation. Nanoparticles are simply too small to support oxygen bubble-formation. Besides, the nanoparticles have been designed in such a way that the release of oxygen is homogeneously distributed around the particle, preventing the formation of a gradient in the concentration of catalytic reactants.

The study of the catalytic action on nanoparticles generating a homogeneous distribution of the reaction products indicates the incapacity of such action to deviate the particle from the purely diffusive motion. For silica nanoparticles the spherical shape and rather homogeneous distribution of motors, hence of reaction products, inhibits the evolution of a propelling force sufficiently robust to rival Brownian force. The same seems to happen for gold spherical nanoparticles and for platinum nanorods.

The capability of chemical energy conversion alone is not sufficient to gain loco-motion in the nano-regime. Examples at big scales[20], micro scale[21, 24, 26], and at nanoscale have shown the importance of the capability of the catalytic engine to transform the chemical energy in such a way to generate an asymmetric distribution of oxygen. Bubble formation and interfacial concentration gradients both rely on inducing in a local change of the environment (the concentration of oxygen), which is the real motor of the propulsion. The study of the motion of nanoparticles has shown that this mechanism fails, despite the catalytic capability of the systems, in modifying the surrounding liquid to ignite the propelling mechanism. They do increase the concentration of oxygen molecules around the particles, but the overall effect is zero because of its spatial homogeneity.

Machines, which realization of the chemical energy conversion homogeneously modifies the environment around their surface, fail to trigger the processes generating the propelling force, or the generated propulsion force is simply not strong enough to overcome Brownian motion.

3.7 Conclusions

The nano-systems studied in this chapter have demonstrated the incapacity of catalytic activity to induce particle motion different from purely Brownian

diffusion. Various factors affecting the propulsion mechanism, such as a symmetrical distribution of the reaction products, the reduced particle size (no-bubble formation) and weak catalytic activity (in case of gold), can play a role in the process. Some of the listed points are strictly related to the difficulties in the making of such particles at nanoscale. At present, no bi-metallic nanorods have been reported, and gold particles have been studied because of the lack of platinum particles with similar size and regular shape, a necessary requirement for an ensemble classification and quantitative analysis.

The idea to quantitatively describe the motion of an ensemble of self-propelling objects demands a single particle approach. Despite the fact that no evidence of self-propulsion has been found in the nano-systems, the characterization of the motion, assuming Brownian motion as background, by using single particle tracking technique has been shown to be a powerful tool for precise nano-motion characterization.

For instance, from the step-size distributions of tracked particles it is possible not only to quantify variations in the value of D, but also to reveal deviations from the random walk movements. If the path followed by the moving particle presents some feature of directionality, it will be revealed in the distribution, which would in that case no longer be described by Eq. 2, and in the MSD time-dependence.

Experience based on the successfully achieved propelling action at the micrometer scale can suggest eventual improvement at the nanoscale. Here, due to the reduced absolute catalytically-active surface area, oxygen bubble formation is inhibited in water. The addition of a small amount of surfactants in the solution will reduce the surface tension of water, thereby stabilizing microbubbles[24].

Interfacial tension gradients arise when the nano-machine consists of two unequal parts, an engine and a cargo asymmetrically located in the body of the particle. The bi-functionalized silica and metallic nanoparticles studied here have their catalytic motors homogeneously distributed on the cargo surface and therefore no gradient can rise. Micro-scale bi-metallic rods, reported on by Paxton *et al.*[21], suggest the design of a similar nano-machine in the future that might be propelled by gradients. The cargo (gold segment) and engine (platinum segment) in such a system are joined together, resulting in an inherently asymmetrical structure. It has been show as well that the surface properties of the cargo may alter the propelling action[50]. This requires additional effort since hydrogen peroxide renders the gold surface hydrophilic.

Once favorable properties of the cargo and catalytic activity of the engine are attained, it will be possible to optimize the factors generating the propelling force, in a future effort to overcome the thus-far dominant Brownian diffusion at the nanoscale.

Bibliography

1. Ed.: Schliwa M., *Molecular Motors*. Wiley-VCH: Weinheim, 2002.
2. Purcell, E. M. *American Journal of Physics* **1977,** 45, 3-11.
3. Kay E.R.; Leigh D. A.; Zerbetto F. *Angew. Chem. Int. Ed.* **2007,** 46, 72-191.
4. Browne W. R.; Feringa B. L. *Nature Nanotech.* **2006,** 1, 25-35.
5. Shapere, A.; Wilczek, F. *Physical Review Letters* **1987,** 58, 2051-2054.
6. M. Porto, M. U., J. Klafter. *Phys. Rev. Lett.* **2000,** 84, 6058-6061.
7. Y. Shirai, A. J. O., Y. Zhao, K. F. Kelly, J. M. Tour. *Nano Lett.* **2005,** 5, (11), 2330-2334.
8. R. K. Soong, e. a. *Science* **2000,** 290, 1555-1558.
9. Hawthorne, M. F.; Zink, J. I.; Skelton, J. M.; Bayer, M. J.; Liu, C.; Livshits, E.; Baer, R.; Neuhauser, D. *Science* **2004,** 303, 1849-1851.
10. J. R. Dennis, J. H., V. Vogel. *Nanotech.* **1999,** 10, 232-236.
11. A. M. Brouwer, e. a. *Science* **2001,** 291, 2124-2128.
12. H. Hess, J. H., V. Vogel. *Nano Lett.* **2002,** 2, (10), 1113-1115.
13. H. Hess, J. C., J. Howard, V. Vogel. *Nano Lett.* **2002,** 2, (2), 113-116.
14. H. Hess, J. C., D. Qin, J. Howard, V. Vogel. *Nano Lett.* **2001,** 1, (5), 235-239.
15. Y. Hong, M. D., U. M. Cordova-Figueroa, A. Sen. *Adv. Funct. Mater.* **2010,** 20, 1568-1576.
16. Dekker, M., *Interfacial Electrokinetics and Electrophoresis*. New York, 2002.
17. H. Watari, M. S., Y. Iiguni. *Anal. Bioanal. Chem.* **2004,** 378, 1693-1699.
18. T.M. Vickrey, J. A. G.-R. *Sep. Sci. Technol.* **1980,** 15, 1297-1304.
19. S. Sundararajan, S. S., M. E. Ibele, A. Sen. *Small* **2010,** 6, (14), 1479-1482.
20. Ismagilov, R. F.; Schwartz, A.; Bowden, N.; Whitesides, G. M. *Angew. Chem. Int. Ed.* **2002,** 41, 652-+.
21. Paxton, W. F.; Kistler, K. C.; Olmeda, C. C.; Sen, A.; St Angelo, S. K.; Cao, Y. Y.; Mallouk, T. E.; Lammert, P. E.; Crespi, V. H. *J. Am. Chem. Soc.* **2004,** 126, 13424-13431.
22. Fournier-Bidoz, S.; Arsenault, A. C.; Manners, I.; Ozin, G. A. *Chem. Comm.* **2005**, 441-443.
23. Howse, J. R.; Jones, R. A. L.; Ryan, A. J.; Gough, T.; Vafabakhsh, R.; Golestanian, R. *Phys Rev Lett* **2007,** 99, 048102.
24. A. A. Solovev, Y. M., E. Bermudez Erena, G. Huang, O. G. Schmidt. *Small* **2009,** 5, (14), 1688-1692.
25. Vicario, J.; Eelkema, R.; Browne, W. R.; Meetsma, A.; La Crois, R. M.; Feringa, B. L. *Chem. Commun.* **2005**, 3936-3938.
26. Heureux, N.; Lusitani, F.; Browne, W. R.; Pshenichnikov, M. S.; van Loosdrecht, P. H. M.; Feringa, B. L. *Small* **2008,** 4, (4), 476-480.
27. Paxton, W. F.; Sundararajan, S.; Mallouk, T. E.; Sen, A. *Angew. Chem. Int. Ed.* **2006,** 45, 5420-5429.
28. Saxton, M. J.; Jacobson, K. *Annual Review of Biophysics and Biomolecular Structure* **1997,** 26, 373-399.
29. Hellriegel, C.; Kirstein, J.; Brauchle, C. *N. J. Phys.* **2005,** 7.
30. Raleigh, L. *Proc. R. Soc. London* **1890,** 47, (364).
31. S. Nakata, S. H., H. Kitahata. *J. Phys. Chem. B* **2003,** 107, 10557-10559.

32. McKee, D. W. *J. of Catalysis* **1969,** 14, 355-364.
33. M. McCabe, T. C. L. *Biochem. Biophys. Acta.* **1975,** 399, 131-138.
34. S. Ljunggren, J. C. E. *Colloids Surfaces A: Physicomchem. Eng. Aspects* **1997,** 129-130, 151-155.
35. J. Happell, H. B., *Low Reynolds Number Hydrodynamics*. Englewood Cliffs, 1965.
36. Kline, T. R.; Paxton, W. F.; Mallouk, T. E.; Sen, A. *Angew. Chem. Int. Ed.* **2005,** 44, 744-746.
37. N. Mano; Heller, A. *J. Am. Chem. Soc.* **2005,** 127, 11574.
38. W. F. Paxton, P. T. B., T. R. Kline, Y. Wang, T. E. Mallouk, A. Sen. *J. Am. Chem. Soc.* **2006,** 128, (46).
39. He, Y. P.; Wu, J. S.; Zhao, Y. P. *Nano Lett.* **2007,** 7, 1369-1375.
40. Einstein A. *Ann. Phys.* **1905,** 17, 549-560.
41. Chandrasekhar, S. *Rev. Mod. Phys.* **1943,** 15, 2-89.
42. Roeffaers, M. B. J.; Sels, B. F.; Uji-i, H.; De Schryver, F. C.; Jacobs, P. A.; De Vos, D. E.; Hofkens, J. *Nature* **2006,** 439, 572-575.
43. Fick, A. *Philos. Mag. J. Sci.* **1855,** 10, 31-39.
44. Langevin, P. *Comptes Rendus Hebdomadaires des Seances de l'Academie des Sciences* **1908**, 508-533.
45. Nelson, E., *Dynamical Theories of Brownian motion 2nd Ed.* 2001.
46. Gillespie, D. T. *Am. J. Phys.* **1993,** 61, (December), 1077-1083.
47. Thompson, R. E.; Larson, D. R.; Webb, W. W. *Biophysical Journal* **2002,** 82, (5), 2775-2783.
48. Yildiz, A.; Selvin, P. R. *Accounts of Chemical Research* **2005,** 38, (7), 574-582.
49. Stober, W.; Fink, A.; Bohn, E. *Journal of Colloid and Interface Science* **1968,** 26, (1), 62-&.
50. Catchmark, J. M.; Subramanian, S.; Sen, A. *Small* **2005,** 1, 202-206.

Chapter 4
Quantitative Analysis of the protein conducting channel SecYEG at the single molecule level

4.1 Introduction

About 25 – 30% of the proteins synthesized in the living cells of all the three domains of life (Bacteria, Archaea, and Eukaryota) are transported into or across the membranes that surround the cells. Interesting is that, despite the differences existing between the three domains, they all share similar protein conducting channels and a multi protein machinery termed translocase. Protein secretion and membrane insertion processes are among the basic functions of all living cells. In bacteria, protein translocation across the cytoplasmic membrane occurs via the protein conducting channel named SecYEG[1]. The details of the SecYEG functioning during the translocation event and the working mechanisms are currently being investigated[1]. In fact, the structure, the organization and the functional role of the various parts of the system involved in the translocation process have being investigated, with various techniques, in numerous works[1] by many groups.

One of the basic, and still open questions concerns the oligomeric state of the channel required for the translocation process. It is still not clear how many SecYEG proteins are required for the translocation. Various models have been proposed for this, the most important ones based on either monomer or dimer models[1-6]. Though extensively studied, the results produced in the last ten years with the implementation of a great number of approaches and techniques still fail to clearly and definitely characterize quantitatively the number of SecYEG proteins required in the translocation process.

In this chapter, a novel approach is proposed to investigate the oligomeric state of the protein conducting channel SecYEG, based on a quantitative characterization of the SecYEGs in the system at the single molecule level. Single molecule fluorescence microscopy, among the advantages introduced and

discussed in the previous chapters of this thesis, offers the possibility to yield quantitative information on imaged clusters of emitters by exploiting the stochastic behavior of fluorescence photobleaching. In this technique SecYEG proteins labeled with a single Alexa Fluor 488 dye molecule are imaged while embedded into proteoliposome (PL) membranes that are attached to a glass surface. By studying the time dependence of the fluorescent signal from the imaged proteoliposomes it is possible to quantify the number of emitters and consequently the number of proteins in each single proteoliposome.

4.2 Translocase system: SecYEG and SecA

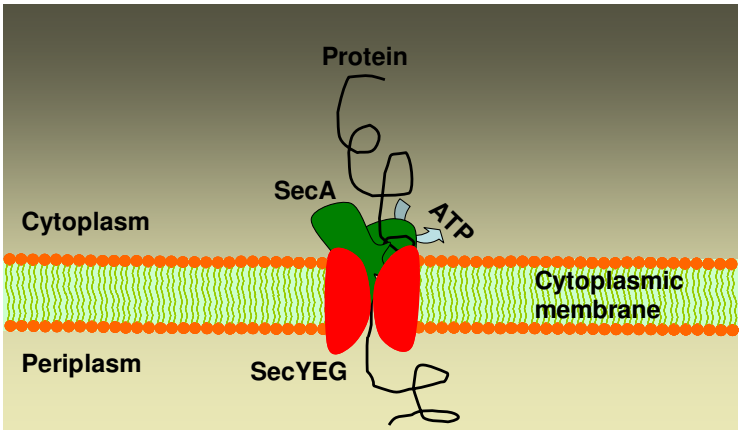

Figure 4.1: Sketch representing the translocase system of bacteria. The proteins synthesized by ribosomes in the cytoplasm are recognized by the SecA (green) that, in cooperation with the SecYEG channel (red), performs the protein translocation reaction by multiple cycles of ATP hydrolysis. The sketch illustrates the monomeric model of the SecYEG during the protein translocation.

Figure 4.1 illustrates the principle of the protein translocation process in bacteria. Two protein complexes, the dimeric motor protein SecA and the heterotrimeric SecYEG (the monomer) complex that forms the membrane channel, constitute the translocase system guiding protein secretion across the cytoplasmic membrane. What is defined as monomeric SecYEG is a rather complex system consisting of three different proteins (SecY, Sec E, and SecG).

In this section, the two core elements of the translocase (SecA and SecYEG) and their functions are introduced. For a more detailed description and discussion of such systems see Driessen and Nouwen 2008[1].

4.2.1 SecA

The ATP dependent motor protein SecA is present in the cytosol and when attached to the SecYEG provides the driving force for the protein secretion[1]. The binding of ATP to SecA ignites the translocation process which occurs as step-wise translocation through multiple cycles of ATP binding and hydrolysis on SecA[7, 8]. SecA ATPase activity is further stimulated in presence of secretory proteins and when attached to the SecYEG[9, 10]. SecA is also involved, while free in the cytosol, in the recognition of signal sequences and binding of proteins destined for secretion[11, 12]. Beyond the scope of this work is the actual oligomeric state of SecA during the translocation reaction, which is also still not clear. Despite the great effort that has been spent on this question and all the methodologies that have been used, the matter is still controversially debated.

What is known is that SecA exists in a dynamic equilibrium between monomer and dimer state while free diffusing in the solution (cytosol), and that this equilibrium is very sensitive to factors such as temperature and detergents[13-15]. In particular the works of Or[13] and of Benach[15] have shown the presence of detergents to favor the formation of monomers. The necessary use of detergents in some experiments might compromise the native configuration of the proteins. For instance, a X-ray structure of SecA co-crystallized with SecYEG by Zimmer et al[2] has shown a monomeric SecA bound to a single SecYEG. Yet, this has been achieved by the use of detergents in the crystallization process that might have influenced the system.

A recent study (I. Kusters et al, in press), performed in a physiological environment, shows that the dimeric state has higher translocation activity *in vitro* than monomeric SecA[4, 16]. Several other works have shown low or absent activity of the monomeric SecA[13, 17], and that the dimeric form of SecA maximizes the coupling of ATP hydrolysis[18]. Those results, if further confirmed, might provide a solid proof of the privileged dimeric state of SecA in the translocation process.

4.2.2 SecYEG

SecYEG is the protein conducting channel embedded into the cytoplasmic membrane through which the majority of bacterial secretory proteins are exported. The binding of the motor protein SecA to SecYEG stimulates the opening of the so called lateral gate leading to a widening of the channel required to accommodate a translocating polypeptide chain[2]. SecYEG possesses a rather complex structure being formed by three distinct subunits named SecY, SecE and SecG[1]. X-ray crystallography studies have revealed the structures of SecYEGs of four organisms in several different conformations[2, 19-22].

The core element is the SecY protein that resembles a clamshell fold. SecE stabilizes the channel by embracing the clamshell acting as a molecular clamp. The functional relevance of SecG is still not completely understood.

In the open state, the channel adopts an hourglass shape with a central funnel allowing the translocation of the polypeptide chain. In the closed state, the channel restricts the passage of ions or other small molecules. A re-entrance loop of SecY at the periplasmic side, termed the plug, blocks the channel and is believed to be displaced for the translocation reaction[1].

Several biochemical[5, 6, 23] and structural[24-26] studies show SecYEG to arrange in higher oligomeric states such as dimers or even tetramers[27], but their functional relevance remains unclear.

The monomer model, supporting the idea that a single SecYEG is sufficient for protein translocation, has been encouraged by new studies done on the eukaryotic homologue, Sec61[28-31] and by the hypothesis that segments of the SecA protein insert directly into the channel[8].

At the same time, a crucial role of the dimeric state has been suggested in several other works[5, 6]. In particular, Osborne et al[3] and Gold et al[32] propose that in the dimeric form one of the two SecYEG binds to the SecA that performs the translocation through the channel of the other SecYEG. Those results contradict the structure presented by Zimmer et al[2], where a single SecA is anchored to a single SecYEG. A definitive solution to the oligomeric state of SecYEG in the translocation problem is still missing.

4.3 Achieving quantitative analysis exploiting photobleaching of single molecules

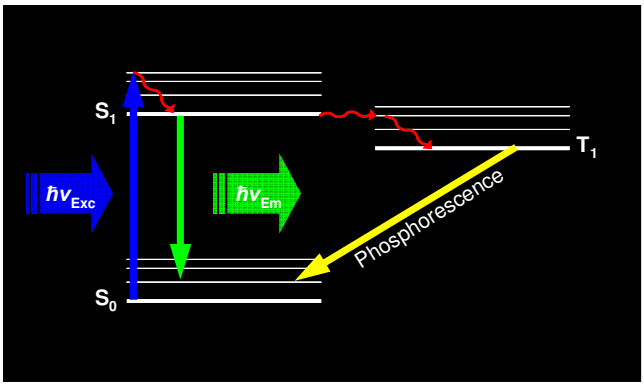

Figure 4.2: Sketch illustrating the molecular electronic and vibronic levels involved in fluorescent emission.

The methodology here proposed aims at a quantitative characterization of the number of emitters in multichromophore systems, based on successive photobleaching of fluorescent molecules. Figure 4.2 sketches the molecular electronic and vibronic states (Jablonski diagram) involved in the fluorescent

emission by a single molecule. In a normal fluorescence cycle the molecule absorbs a photon (blue arrow), bringing it from the ground singlet state (S_0) to a vibronic level of the first excited singlet state (S_1). After relaxation to the lowest vibrational level of the first excited state, the molecule can return to the ground state by emission of a photon (green arrow). This constitutes the normal fluorescence process which, provided that there are sufficient incident excitation photons repeats itself with a MHz repetition rate. However, while in the excited states, the excitation can migrate to the triplet state (T_1) by intersystem crossing[33]. Since T_1 is characterized by a much longer lifetime (ms - s) than S_1 (~ns - μs), this intersystem crossing will interrupt the fluorescent emission process for an appreciable time. Moreover, while in the triplet state, the molecule is chemically more reactive; this may lead to a photochemical reaction with one of the neighboring molecules, for instance with oxygen in the surroundings. When this latter process occurs it generates a new molecule that, with high probability, will no longer be fluorescent. This irreversible process is called photobleaching, and may be considered as one of the most limiting factors in various applications of single molecule spectroscopy.

Even though generally photobleaching is considered a problem in single molecule microscopy, there are a number of applications where photobleaching acts as a useful tool[34-36]. Single molecule microscopy and the features related to photobleaching have provided ultimate level of sensitivity for biological systems[37-39]. For instance, Nakajo et al[37] have applied the fluorescence bleaching method to investigate the stoichiometry of the KCNQ1 voltage-gated potassium channel and its auxiliary subunit KCNE1, crucial in the regulation of the heartbeat. Despite previous results have shown the stoichiometry to be 4:2 (4 KCNQ1 : 2 KCNE1), Nakajo study reveals the flexibility of the system which can provide stoichiometry up to 4:4.

Van den Bogaart et al[39] applied photobleaching to study the intracellular membrane fusion reactions mediated by the interaction of SNARE proteins. They show a single SNARE protein to be sufficient in the membrane fusion event.

Both reported examples highlight the achieved ultimate sensitivity. The possibility to resolve the number of reactants involved in chemical reactions crucial for the life of biological systems surely prove the sensitivity and support the power of the method. Still the new approach has limitations.

One of the weak points of the use of photobleaching is discussed here, it is sketched in Figure 4.3, and deals with the very nature of optical signal. Photons generate a noise which amplitude equals the square root of the number of photons. The methodology introduced here is based on the recognition of signal features that can only be observed under certain values of the signal-to-noise ratio.

In general, transient of fluorescent signal might present exponential decay if the source consists of multiple emitters (i.e. more than 10). The time trace decay can also present sharp step-like decay events when generated by a smaller number of

emitters. Step-like variations in the fluorescent signal are the features on which the work introduced here is based on. Counting the number of steps, before complete bleaching, can reveal the exact number of emitters. In the case of signal produced by numerous emitters, single bleaching events are more difficult to observe because the amplitude of a single event might be hidden in the noise.

Figure 4.3 illustrates two diffraction limited spots presenting different fluorescence intensity and imaged with the wide field fluorescent microscope. The six images on the left resemble the brightest of the two spots at different times. As visible in the various images the intensity of the spot decreases from the top left image (initial time) to the bottom right image upon constant illumination by the laser excitation. The diagram on the bottom left shows the time dependence of the emission intensity. The exponential decay (illustrated by the red exponential curve) resembles the typical fluorescence photobleaching of an ensemble of emitters. The high number of photons of the signal and the generated noise prevent the possibility to observe step-like bleaching events related to single emitters. The noise amplitude is much bigger than the amplitude of a single bleaching event.

On the other hand, the spot represented in the two images on the right, instead, shows a time dependence of the intensity (diagram on the bottom right) consisting of two single steps before complete bleaching. Step-like bleaching events corresponding to single molecules bleaching events are the key factor to perform a quantitative analysis at the single molecule level. In fact, as aforementioned, from the diagram is possible to count how many emitters are included into the spot. Sudden photobleaching events appear as step-like since emission from a single fluorescent molecule is quantized; either the molecule emits or it does not. The bleaching events present such a sharp time behavior at the time scale used for imaging (50 ms integration time/frame) since consequence of the migration of the excitation from the singlet excited state to the triplet state, process that occurs typically on time scale much shorter than the frame rate.

It has been mentioned already that the possibility to directly observe single steps and therefore to count the number of emitters is strictly related to the actual number of emitters. The fluorescent signal is required to generate a photon-noise much smaller than the amplitude of a single photobleaching step.

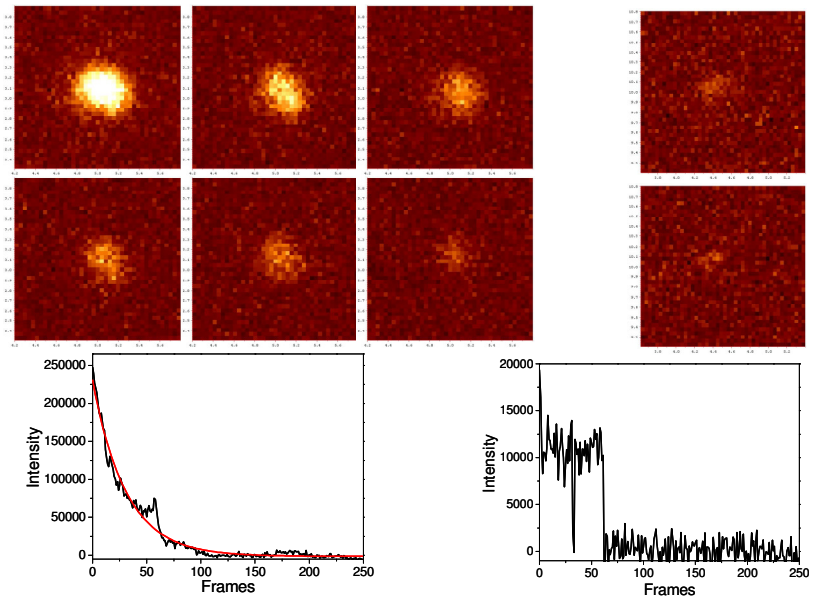

Figure 4.3: Images obtained with wide field fluorescence microscope showing diffraction limited spots consisting of several emitters. Six images of the same spot are visible on the left. From the top left image to the right bottom one, the fluorescent signal decreases as consequence of photobleaching. The diagram on the left presents the time dependence of the intensity of the imaged spot. The exponential time decay (red curve) resembles the expected fluorescence decay typical of an ensemble of emitters. The images on the right show a spot that from the diagram of the intensity time dependence appears to consist of two emitters. The step-like photobleaching events represent the key feature gained by joining single molecule sensitivity and photobleaching analysis.

Let us assume, for example, to have n emitters emitting each N photons in unit time. Each emitter will generate a noise equal to $\sqrt{N}$. Thus the optical signal (S) and the noise (B) before any photobleaching event occurs have the following values:

$$S = n \cdot N \qquad \text{and} \qquad B = \sqrt{n \cdot N}$$

In principle, the requirements from the signal to allow counting of the number of emitters are rather simple and can be approximate to:

$$N > \sqrt{(n-1) \cdot N}$$

where N is the amplitude of a single step and $\sqrt{(n-1) \cdot N}$ is the value of the noise after the bleaching event. Though simple, there is not an exact number of emitters above which the step can be recognize and below it cannot. There exist examples of signal processing methods[39] that allow quantitative characterization even when the actual noise is bigger than the step amplitude; they actually apply to signals

where the S/N is about 1. Though such methods are used and accepted, they demand more sophisticated signal processing and the approximated results might loose in accuracy. The signal processing applied here is based on much greater step/noise ratio and does not require any further signal manipulation.

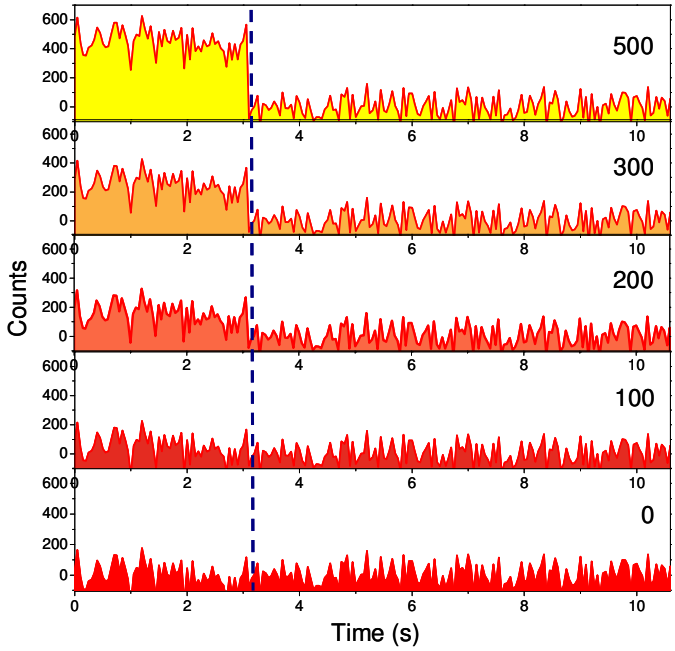

Figure 4.4: Examples representing different step's amplitude and their comparison in case of a constant noise. The bottom graph (0) illustrates a constant optical signal which noise value is around 70. This noise corresponds to an optical signal of ~ 5000 photons (assume the noise to be purely Poissonian) which average value is set to zero. Above graphs show steps of different amplitude (100, 200, 300, and 500) occurring at the same time interval. Though the graphs corresponding to step with amplitude 100 and 200 have bigger amplitude than the noise value (70) their recognition is not immediate and requires further signal manipulation. Steps with higher amplitude can be easier recognize and analyze with a simple step-like function to extract the amplitude of the step.

Figure 4.4 is introduced to facilitate the meaning of recognition of the step-like features of fluorescence photobleaching. Several steps of different amplitude are represented with the same noise value. The graph on the bottom (0) resembles a constant optical signal which noise value is 70, thus, assuming the noise to be purely optical noise, corresponding to an optical signal consisting of ~ 5000 photons. Here the mean value of the signal (5000) is set as zero.

The other four graphs represent the occurrence at the same time interval of a single bleaching step with different amplitudes (100, 200, 300, and 500). Though the graphs relatives to step with amplitude 100 and 200 fulfill the requirement for

the step amplitude to be higher than the noise (70), still they are difficult to recognize. To extract the value of the step's amplitude in these two cases might require further signal manipulation.

On the other hand, steps with amplitude of 300 and 500 clearly present the step-like feature required for the quantitative analysis, and the value of the step's amplitude can be extracted by the use of a simple step-like function.

Another important point is related to the stochastic distribution in time of the photobleaching events. The process regards the chemical interaction between two different molecules (i. e. dye and oxygen molecule) and the rate of this interaction strictly depends on the local environment and the relative configuration of the two molecules. It is highly unlike that ensembles of uncorrelated fluorescent molecules will photobleach at the same. The photobleaching steps are randomly distributed in time and thus often occurring one by one. The rate of bleaching steps depends quadratically by the excitation power density[40]. At high bleaching rate the temporal overlapping of more bleaching steps might increase, thus resulting in steps not corresponding to a single molecule. A more detailed discussion concerning the limitation of the technique is presented in the Appendix 2.

The obtained single molecule sensitivity and the features related to photobleaching process might result as the ultimate tool to finally unravel the controversial discussion concerning the configuration of the translocase system SecA-SecYEG. In fact, it might be able to show whether the translocation of a protein requires monomer or dimers.

4.4 Experiment

4.4.1 Sample

The proteoliposomes (~100 nm) dispersed in buffer A (50 mM Hepes pH 7.6, 5-mM KCl, 1 mM Dithiothreitol (DTT)) consist of a synthetic lipid mixture (30% 1,2-dioleoyl-sn-glycero-3-phospho- (1'-rac-glycerol) (DOPG), 30% 1,2-dioleoyl-sn-glycero-3-phosphoethanolamine (DOPE), 40% 1,2-dioleol-sn-glycero-3-phosphocholine (DOPC)) and contain an undetermined number of fluorescently labeled SecYEG. Prior reconstitution into the liposomes, SecYEG had been labeled with a single Alexa Fluor 488 fluorescent dye at a specific cysteine residue (C295) via maleimide chemistry[41]. The labeling efficiency was determined by absorption to ~ 90%. Labeling efficiency is crucial for this type of experiment since only the labeled SecYEGs are fluorescing and thus visible. A lower labeling efficiency, i. e. 50%, would heavily compromise the accuracy of the quantitative analysis misleading the eventual experimental conclusions.

For the microscopy experiment, a 2 mm-wide channel is created by using a custom made 0.5 mm silicon spacer between the microscope slide and the

coverslip. First, the channel was washed with buffer A followed by injection of the SecYEG-PLs into the channel. Due to the electrostatic charge of the coverslip glass surface, enhanced by the washing the slides with 1 M solution of NaOH (coverslips cleaning procedure), some of the proteoliposomes adsorbed non-specifically to the surface. Finally, buffer containing free diffusing PLs is washed away by injection of buffer A. Thus, proteoliposomes attached to the slide surface and immersed in buffer A were obtained.

Upon laser excitation with λ = 488 nm Alexa Fluor 488 molecules emit the fluorescent signal. Figure 4.5 illustrates a survey image of a typical sample. The concentration of bright spots (fluorescence) is such to allow the analysis of each individual. Images are taken at 20 Hz rate (50 ms) and the time behavior of the sample is recorded by collecting arrays of subsequent images till complete photobleaching of the imaged area.

The time dependence of the fluorescence intensity emitted by each spot is obtained by integrating the pixel count in an area around the spot as illustrated in the zoom in of Figure 4.5 (right image). The integration area is kept constant throughout all the analysis.

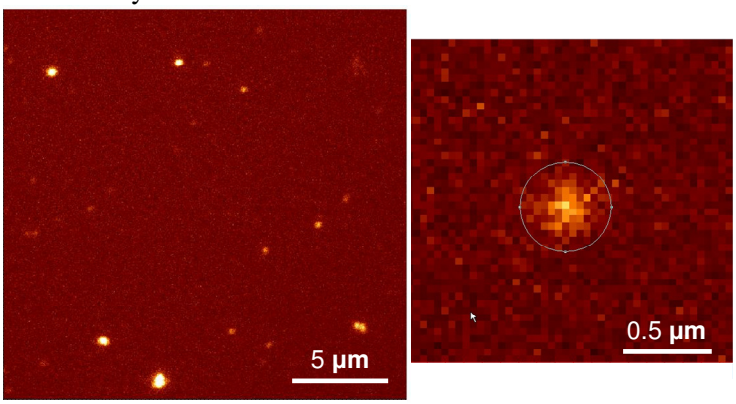

Figure 4.5: A survey image of the sample is presented together with a zoom in on a single spot. The concentration of bright spots on the coverslip surface is such to allow the analysis of single spots. In the zoom in it is also visible the area of counts integration.

4.4.2 Results

Figure 4.6 presents a collection of time traces corresponding to several fluorescent spots. As visible from Figure 4.5, the illuminated area contains very bright objects and others that are weakly visible; besides some of the spots appear bigger than others. This is likely due to the aggregation of proteoliposomes on the surface. The size of a single proteoliposome (~100 nm) containing fluorescent

molecules should appear as a diffraction limited spot with circular symmetry (in reference to Chapter 5: here the dyes are free to rotate and the SecYEG protein to diffuse in the membrane). Therefore, the analysis is limited to diffraction limited spots only.

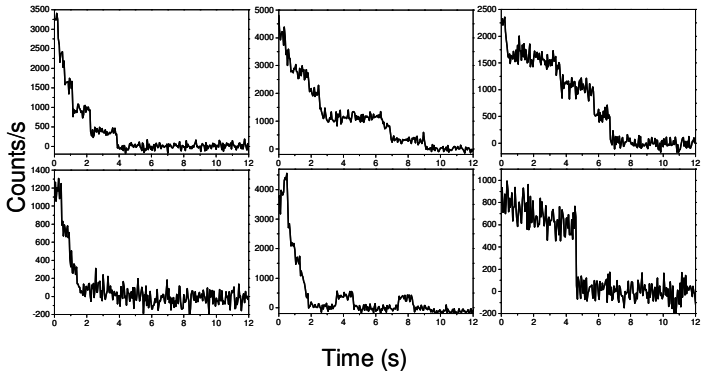

Figure 4.6: Examples of time dependence tracks of the intensity from six different spots. In the presented trajectories the intensity decreases with finite steps corresponding to the photobleaching of a single emitter. In the temporal analysis of fluorescence are considered only those spots where distinguished steps are clear.

From intensity time traces such as the ones presented in Figure 4.6 it is possible to measure the amplitude (counts) of each individual photobleaching step. The inset of Figure 4.7 presents the distribution of the amplitude of each single photobleaching step observed. The distribution consists of ~130 steps (~80 spots). The amplitude distribution mean value (~500 counts/s) is obtained by fitting the distribution with a Poissonian curve. Once estimated the mean value for the intensity amplitude for a single step, the intensities of each single fluorescent spot imaged in the first frame of each movie (photobleaching free) are divided by the mean value of the step-amplitude in order to evaluate the number of dyes present in the spots.

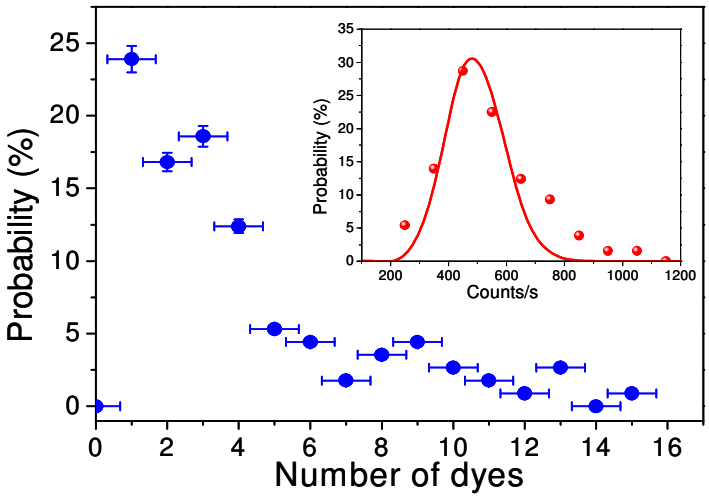

Figure 4.7: Distribution of the number of fluorescent molecules (blue graph) contained in the imaged spots. In the analysis is not possible to discriminate whether some of the spots consist of clusters of proteoliposomes or if a single liposome contains many fluorophores. In fact, some of the spots consist of more than 10 fluorophores. More than 20% of the images spots contain a single fluorophore thus a single SecYEG protein. In the inset (red graph) describe the distribution of the amplitude of single steps.

The blue distribution of Figure 4.7 illustrates the distribution of the number of fluorophores that are contained in each fluorescent spot. The distribution has its maximum in 1 meaning that more that 20% of the imaged spots consists of a single dye and a single SecYEG protein. It is not possible at this stage to discriminate whether the spots consisting of several more dyes are clusters or if, actually, such high number of proteins is present in their membrane. In conclusion, the sample seems to consist of a population of proteoliposomes 25% of which posses a single SecYEG protein.

4.5 Conclusion and outlook

The purpose of this work is to develop a new approach able to quantitatively characterize the number of fluorescently labeled SecYEGs inside proteoliposome membranes. At the knowledge of the author, an analogue work has been published only recently[42]. Results show the proof of principle that single molecule microscopy is able to discriminate the population of proteins in the investigated proteoliposomes. The time traces of the intensity of the fluorescent spots, consisting of the emission pattern from single or clusters of proteoliposomes, are obtained with sufficiently clear step-like features characteristic of photobleaching

single molecule events. The distribution of the amplitudes of 130 different steps has allowed estimating the mean value of the fluorescence intensity corresponding to a single molecule. Subsequently, this mean value has been used to determine the number of molecule contained in each imaged fluorescent spot.

The described single molecule approach has shown the potential to unequivocally determine the functional oligomeric state of SecYEG during protein translocation if functional assays are performed on the investigated proteoliposomes. To this end, the SecYEG reconstitution procedure was optimized as such that the majority of PLs contein only a single SecYEG (I. Kusters, unpublished data). In parallel to this study, an *in vitro* protein translocation assay with single molecule sensitivity was developed (I. Kusters, PhD thesis, chapter 7) to correlate the number of SecYEG/PL with translocation activity. The combination of these two approaches will allow to determine if PLs containing a single SecYEG channel are active or if rather higher oligomeric states are required for the translocation process.

Based on the methodology presented here, a thorough study on the translocase system will continue. As seen from the distribution of the number of dyes in the fluorescent spots, many of them contained more than two. The next step should aim to decreasing the occurrence of such objects. This will be achieved by first lowering the concentration of proteoliposomes in the starting solution which will reduce the occurrence of PL-clusters. Secondly, by decreasing the concentration of SecYEG protein in the reconstitution reaction of the proteoliposomes lower number of SecYEG per PL can be achieved (I. Kusters, unpublished data). In such a way it should be possible to produce a population of proteoliposomes containing only a single SecYEG.

Once obtained proteoliposomes with a single SecYEG are obtained, it may be possible to conduct an even more important study aiming at the direct observation of the translocation process of a single polypeptide chain through, possibly, a single SecYEG channel.

The translocation activity of the translocase system is only achieved in intact membranes. If the proteoliposome membrane ruptures, i. e. as result interactions with the glass surface, no activity will be obtainable. The integrity of the membranes may be checked with fluorescent microscope by using a multi-color approach. By inserting fluorescent lipids (emission in red) in the membrane and by filling the membrane with water soluble green fluorescent molecules, the integrity of the membrane could be directly observed. If the membrane would open upon surface immobilization, the green fluorophores would diffuse away from the spot (red) indicating the position of the membrane. On the other hand, if the membrane maintains its integrity, it will be possible to co-localized (same position) both the red and the green signal and fluorescence decrease will correlate with bleaching behavior rather than diffusion.

Once established that the membrane attached on the surface are closed and therefore the translocation activity is possible, the latter may be directly observable. The SecYEG proteins are labeled specifically with Alexa Fluor 488. By labeling the polypeptide chains with a spectrally separated fluorophores that can serve as acceptor for the light emitted by Alexa Fluor 488 (Alexa Fluor 594 or 610) it may be possible to obtain FRET signals rise when the two dyes are at a sufficiently small distance (few nm) which should occur during the translocation of the polypeptide chain through the channel.

Recently, the translocation process has been investigated at single molecule level and at different stages of translocation yielding the conclusion that the SecYEG is monomer at all stages [Kedrov A. et al unpublished data].

Direct observation of single SecYEG complexes being actively engaged in protein translocation would be the ultimate proof for the functional oligomeric state of this intriguing membrane channel. The here presented methodology provides us with a promising tool to achieve this goal.

Bibliography

1. Driessen A. J.; Nouwen N. *Annu. Rev. Biochem.* **2008,** 77, 643 - 667.
2. Zimmer J.; Nam Y.; al, e. *Nature* **2008,** 455, (7215), 936 - 943.
3. Osborne . R.; Rapoport T.A. *Cell* **2007,** 129, (1), 97 - 110.
4. de Keyzer J.; van der Sluis E. O.; al, e. *J. Biol. Chem.* **2005,** 280, (42), 35255 - 35260.
5. Duong F. *EMBO J.* **2003,** 22, (17), 4375 - 4384.
6. Tziatzios C.; Schubert D.; et al. *J. Mol. Biol.* **2004,** 340, (3), 513 - 524.
7. Schiebel J.; Driessen A. J.; et al. *Cell* **1991,** 64, (5), 927 - 939.
8. Economou A.; Wicker W. *Cell* **1994,** 78, (5), 835 - 843.
9. Lill R.; Dowhan W.; et al. *Cell* **1990,** 60, (2271 - 280).
10. Miller A.; Wang L. *Biochemestry* **2002,** 41, (16), 5325 - 5332.
11. Vrontou E.; Economou A. *Biochim. Biophys. Acta* **2004,** 1964, (1 - 3), 67 - 80.
12. Gouridis G.; Karamanou S. *Nature* **2009,** 462, (7271), 363 - 367.
13. Or E.; Navon A. *EMBO J.* **2002,** 21, (17), 4470 - 4479.
14. Woodbury R. L.; Hardy S. J.; et al. *Protein Sci.* **2002,** 11, (4), 875 - 882.
15. Benach J.; Chou Y. T.; al, e. *J. Biol. Chem.* **2003,** 278, (6), 3628 -3638.
16. Jilaveanu L. B.; Oliver D. *J. Bacteriol.* **2006,** 188, (1), 335 - 338.
17. Jilaveanu L. B.; Zito C. R.; al, e. *Proc. Nat. Acad. Sci. USA* **2005,** 101, (21), 7511 - 7516.

18. Mao C.; Hardy S. J.; et al. *J. Bacteriol.* **2009,** 191, (3), 978 - 984.
19. Mitra K.; Jenni S.; al, e. *Nature* **2005,** 438, 318 - 324.
20. Van den Berg B.; T.A.., R.; al, e. *Nature* **2004,** 427, 36 - 44.
21. Tsukazaki T.; Nureki O.; et al. *Nature* **2008,** 455, 988 - 991.
22. Egea P. F.; Stroud R. M. *Proc. Nat. Acad. Sci. USA* **2010,** 107, (40), 17182 - 17187.
23. Bessonneau P.; Besson V.; et al. *EMBO J.* **2002,** 21, (5), 995 - 1003.
24. Meyer T. H.; Menetret J. F.; et al. *J. Mol. Biol.* **1999,** 285, (4), 1789 - 1800.
25. Mitra K.; Schaffitzel C.; et al. *Nature* **2005,** 438, (7066), 318 - 324.
26. Scheuring J.; Braun N.; et al. *J. Mol. Biol.* **2005,** 354, (2), 258 - 271.
27. Manting E. H.; Driessen A. J.; et al. *EMBO J.* **2000,** 19, (5), 852 - 861.
28. Hanein D.; Matlack K. E.; et al. *Cell* **1996,** 87, (4), 721 - 732.
29. Beckmann R.; Bubeck D.; et al. *Science* **1997,** 278, (5346), 2123 - 2126.
30. Beckmann R.; Spahn C. M.; et al. *Cell* **2001,** 107, (3), 361 - 372.
31. Hamman B.; Chen J. C.; et al. *Cell* **1997,** 89, (4), 535 - 544.
32. Gold V. A. M.; Duong F.; Collinson I.; et al. *Proc. Nat. Acad. Sci. USA* **2010,** 107, (22), 10044 - 10049.
33. Lakowicz J. R., *Principles of Fluorescence Spectroscopy*. 3 ed.; Springer: 2006.
34. Bopp M. A.; Hochstrasser R. M.; et al. *Proc. Nat. Acad. Sci. USA* **1997,** 94, 10630 - 10635.
35. Gordon M. P.; Ha T.; Selvin P. R. *Proc. Nat. Acad. Sci. USA* **2004,** 101, (17), 6462 - 6465.
36. Cannone F.; Chirico G. *J. Phys. Chem. B* **2006,** 110, 16491 - 16498.
37. Nakajo K.; Isacoff E. Y.; et al. *early edition* **2010**, 1 - 6.
38. Park M.; Song N. W.; et al. *Bull. Chem. Soc. Jpn.* **2005,** 78, 1612 - 1618.
39. van den Bogaart G.; Jahn R.; al, e. *Nature* **2010,** 17, (3), 358 - 365.
40. Gensch T.; Bohmer M.; Aramendia F. *J. Phys. Chem. A* **2005,** 109, 6652 - 6658.
41. Kusters, I.; van den Bogaart, G.; de Wit, J.; Krasnikov, V.; Poolman, B.; Driessen, A. *Methods Mol Biol* **2010,** 619, 131-43.
42. Deville K.; Collinson I.; et al. *J. Biol. Chem.* **2011,** 286, (6), 4659 - 4669.

Chapter 5
Point Spread Function characterization

5.1 Point Spread Function in the classical approximation (Airy formula)

5.1.1 Definition

The Point Spread Function (PSF) of an imaging system represents the response to a point-like source of light. An emitter with spatial dimension much smaller (one or two orders of magnitude) of the emission wavelength (λ_{em}) is a point-like source. The PSF is the response of the system to a delta function, and basically resembles the capability of an imaging system to focus the light collected from a point emitter. Sharper is the image (small and defined PSF), higher is the resolving power. To highlight its relevance let us do it through a different imaging technique.

Painting often consists in representing objects by the use of pencils or paintbrushes. The smaller trace a paintbrush can draw has the size of its tip. Any image consists of a collection of points. Obviously, it is an extremely poor description of what painting is; nevertheless, for some was not that far. The artistic movement of pointillism, developed around the end of 19th century, based the drawing technique on what just mentioned. George Seurat is the first and most famous representative of the movement. Figure 5.1 illustrates a detail from one of Seurat's paintings: *Parade de Cirque* (1889).

From the details it is possible to clearly distinguish single monochromatic spots. The smaller object the painter can draw coincides with the size of the paintbrush's tip. In a similar way images are formed in a microscope.

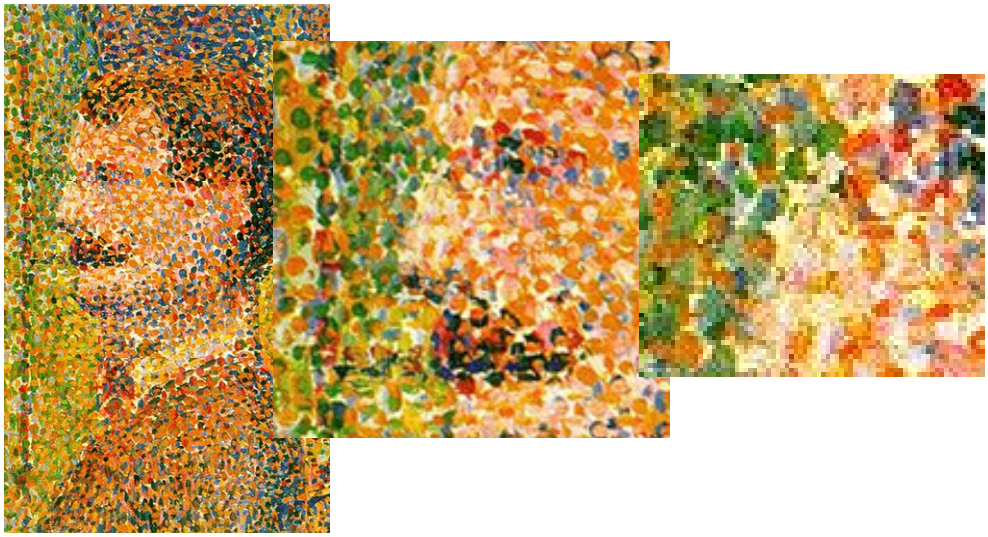

Figure 5.1: Detail from *Parade de Cirque*, *George* Seurat 1889.

Figure 5.2 illustrates how a microscope (represented by the single lens) generates the image of a point-like source emitter in the focal plane (X – Y plane). Let us use an incoherent point-like source (spatially isotropic emission); a microscope has limited collection efficiency due to the finite size of the lens (objective) used to collect the emitted photons. The microscope can collect only those photons that are travelling towards and incident to the lens losing all the others.

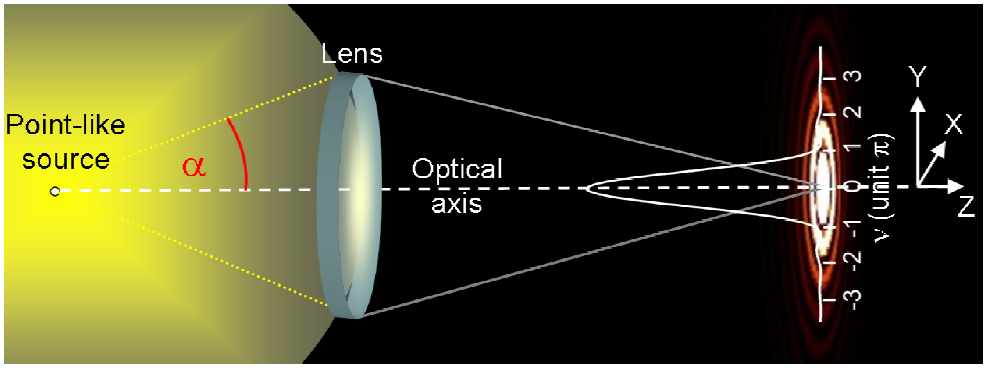

Figure 5.2: Schematic of the formation in the focal plane of the image of a point-like emitter. Light collected by the lens is focused on the focal plane. The intensity of the photons distribution has its maximum at the intercept of focal plane - optical axis. The zeros of the intensity are generated by the diffraction from the lens; in particular, the position of the first zero determines the optical resolution. Due to the circular shape of the lens, the light distribution presents circular symmetry around the optical axis. The central disk is called Airy disk.

Afterwards, the lens "duplicates" the object (collected photons) in the focal plane. The distribution of photons in the focal plane is what defines the point spread function. The finite size of the lens affects profoundly the generated image that will result diffraction limited[1]. Each single point in the lens behaves like a single emitter[1], thus creating an interference pattern, called diffraction pattern, which forms the image. Figure 5.2 illustrates the image of a point-like source in the focal plane. It consists of a central disk surrounded by rings. The geometrical shape of the PSF is determined by the geometry of the lens.

5.1.2 Mathematical model: Airy formula

In 1835 Airy[2] mathematically described the diffraction-limited distribution of photons collected by circular lens from a point-like source.
The Airy function in the focal plane is given by:

$$I(0,\nu) = \left(\frac{2J_1(\nu)}{\nu} \right)^2 \qquad \text{Eq. 1}$$

where $J_1(\nu)$ is the 1st order Bessel function. I is the intensity at a position r off optical axis and $\nu = r \cdot \frac{2\pi n}{\lambda} \sin\alpha = r \cdot \frac{2\pi}{\lambda} NA$; n refractive index, λ wavelength of emitted light, *N.A.* is the numerical aperture ($N.A. = n \cdot \sin\alpha$), and α the semi-angle of the light cone collected by the lens. The first zero of the function $J_1(\nu)$ determines the first zero in the intensity distribution thus the size of the central disk, called Airy disk.

The importance of the size of the Airy disk, especially concerning the resolution of a microscope, will be treated more accurately in the next paragraph. In the area included in the first zero (Airy disk), is concentrated ~ 84% of the total intensity (Figure 5.3). Often the secondary rings are not clearly resolvable.

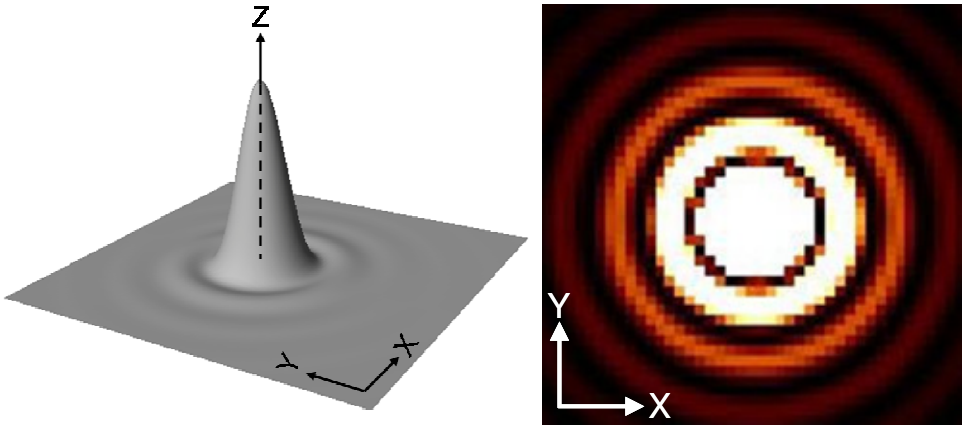

Figure 5.3: 3- and 2-dimensional intensity distribution of the PSF. In the central disk (Airy disk) is concentrated about 84 % of the total light intensity. In the 2-dimensional image the intensity in the Airy disk has been set above the saturation level to make visible the outer rings.

The position in the focal plane (X-Y plane) corresponding to the first zero is found for (in a non-approximated solution)[3]:

$$r_0 = \frac{\lambda}{2\pi n}\frac{1}{\tan\alpha}\nu \Rightarrow r_0 = 0.61\frac{\lambda}{n\tan\alpha}$$

r_0 is the radius of the Airy disk, therefore the least resolvable distance according to Rayleigh criterion. The implications of the value of r_0 concerning the optical resolution will be treated later, here it is important to take a look to the formula itself. For $\alpha \rightarrow \pi/2$, $r_0 \rightarrow 0$ suggesting that the Airy formula is not valid for large angles[3]. The approximation Airy used in the derivation of the formula is equivalent to set $\cos\alpha = 1$, so that the formula can be written in the well known form:

$$r_0 = 0.61\frac{\lambda}{n\sin\alpha}$$

being $\tan\alpha = \sin\alpha$. The Airy formula is valid in the approximation that the collection angle of the lens is taken not too big (paraxial approximation).

There is also a second approximation in the derivation of the formula concerning the illumination of the lens. By illumination it is meant the distribution of light intensity from the source on the lens. It is assumed the intensity to be homogeneously distributed; the point-like source irradiates light which spherical wave-surfaces have homogeneous amplitude. The photons emitted by the point-like source are assumed to have uncorrelated orientation of the electric field. Therefore the light is unpolarized. Such source could be represented by a point-like object consisting of several uncorrelated single emitters, or by a single rotating dipole,

such as a thermally-driven rotating single fluorescent molecule, resulting again in uncorrelated emitted photons.

The Airy formula, calculated in a regime where the two aforementioned approximations are valid, defines a PSF with circular symmetry around the optical axis. The value of r_0 is the same in all radial directions in the optical plane of the lens (see Figure 5.3).

5.2 Point Spread Function characteristics with polarized light source and no-paraxial approximation

Modern laser microscopy has gained the potential to detect and resolve single dipole emitters such as single fluorescent molecules. This has been possible thanks to crucial technological improvements; particularly relevant is here the availability of objectives with high numerical aperture substantially improving the collection efficiency of optical systems. The numerical aperture of an objective gives a measure of the semi-angle on which the lens gathers the photons emitted by the source. Objectives with NA=1.4 (used in this thesis) provides a collecting semi-angle of about 70 degrees. Clearly in this circumstance the paraxial approximation used to derive the Airy disk formula is no longer valid. This might provide the possibility to explore different conditions for the imaging process.

Theoretically, a solution for the characterization of the PSF has been derived in 1943 by Hopkins[3] when neglecting the two approximations used for the classical formula. He calculated the formula describing the Airy disk in the case of a polarized light emitter omitting as well the paraxial approximation. Hopkins calculations describe the Airy disk up to ~40 degrees for the collection semi-angle. The PSF is shown to experience a geometrical change: from circular to elliptical.

Further improvements were achieved by Richards and Wolf [4], who extended the calculation to larger angles. They show how the diffraction limited pattern of the PSF changes as the angle rises up to 90 degrees. As anticipated by Hopkins' calculations, by keeping fixed the orientation of the single dipole and increasing the collecting angle, the PSF assumes elliptical shape.

The mathematical investigation on the structure of the electro-magnetic field near the focus was performed to derive expressions for the electric and magnetic vectors in the image space. They discuss the symmetry properties of the field with respect the focal plane and calculate the distribution of the time-averaged electric and magnetic energy densities.

The solution for the electric energy density takes the form:

$$< w_e(u,v,\phi) >= \frac{A^2}{16\pi}\left\{ |I_0|^2 + 4|I_1|^2 \cos^2\phi + |I_2|^2 + 2\cos 2\phi \Re(I_0 I_2^*) \right\}$$

with A constant and:

$$I_0(u,v) = \int_0^{\alpha} \cos^{\frac{1}{2}}\theta \sin\theta(1+\cos\theta) J_0\left(\frac{v\sin\theta}{\sin\alpha}\right) e^{iu\frac{\cos\theta}{\sin^2\alpha}} d\theta$$

$$I_1(u,v) = \int_0^{\alpha} \cos^{\frac{1}{2}}\theta \sin^2\theta J_1\left(\frac{v\sin\theta}{\sin\alpha}\right) e^{iu\frac{\cos\theta}{\sin^2\alpha}} d\theta$$

$$I_2(u,v) = \int_0^{\alpha} \cos^{\frac{1}{2}}\theta \sin\theta(1-\cos\theta) J_2\left(\frac{v\sin\theta}{\sin\alpha}\right) e^{iu\frac{\cos\theta}{\sin^2\alpha}} d\theta$$

$<w_e>$, I_0, I_1, and I_2 are expressed as function of the optical coordinates in the image space u and v defined by the formula:

$$u = kz\sin^2\alpha$$

$$v = k\sqrt{x^2+y^2}\sin\alpha$$

with k the wave vector. θ ($0 \le \theta \le \alpha$) is the angle at which light rays are focused/collected, in other words it describes the aperture, and ϕ ($0 \le \phi \le 2\pi$) represents the rotation around the optical axis. The energy density in the focal plane, determining the point spread function, is obtained for u=0 (z=0).

The solution proposed by Richards and Wolf proves its consistency when applied to the same conditions used by Airy in his model. In fact, they calculated independently for both the cases that, if $\alpha \sim 0$ (paraxial approximation) or the point source emits unpolarized light, the solution of the model converges to the classical Airy model:

$$< w_e >= \frac{A^2\alpha^4}{16\pi}\left(\frac{2J_1(v)}{v}\right)^2$$

Figure 5.4 shows the 3- and 2-Dimensional distribution of the light intensity according to the calculation of Wolf. In particular, the 2-dimensional representation of the PSF emphasizes the elliptical shape. The PSF represented is obtained with α = 70° and the emitting dipole oriented along the Y-axis. The size of the distribution along the two axes supports Richards and Wolf statement: "*For large values of α, the ellipticity of the contours becomes quite pronounced and the first minimum in the azimuth ϕ = 0* (Y-axis) *is well outside the first zero of the Airy pattern, while in the azimuth ϕ = π/2* (X-axis) *is well inside*"[4]. Once again the intensity in the central disk has been enhanced beyond the saturation level in order to make the outer rings visible.

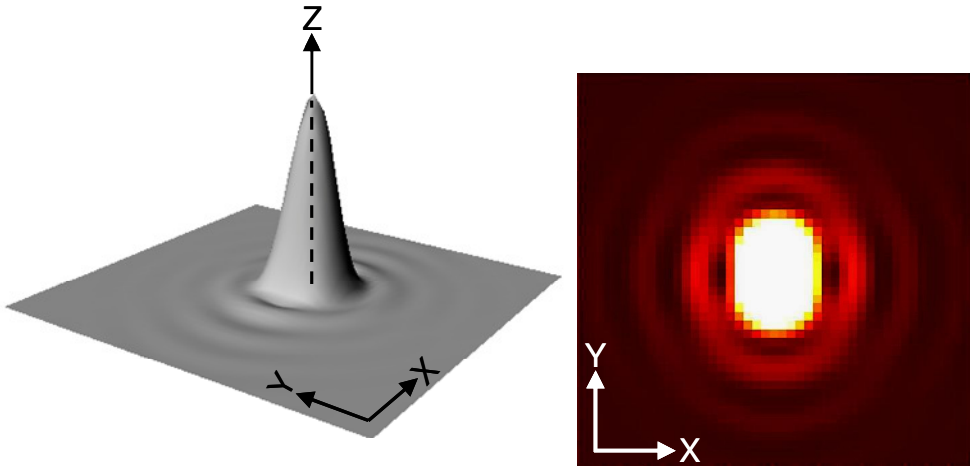

Figure 5.4: 3- and 2-Dimensional intensity distribution of the PSF of a polarized emitter and NA=1.4 (α~ 70°). The focal plane (X-Y) distribution clearly shows the elliptical shape of the PSF. The orientation of the dipole source is along the Y axis. The spatial extension of the PSF in the X direction is reduced compared to the classical case, while it results elongated in the direction of the orientation of the dipole (Y-axis).

5.3 Experimental verification

5.3.1 Ellipticity and in-plane orientation

The experimental verification of the consistency of the described model (Richards and Wolf) for the PSF requires a polarized point-like emitter and a high NA objective. Single molecules of a fluorescent dye imbedded in a glassy-polymer matrix might provide a polarized point-like source.

A solution containing Poly(methyl methacrylate) (PMMA) polymer and highly diluted Alexa Fluor 488 has been spin coated onto a glass cover slide. The high glass transition temperature (Tg) of the PMMA (85° C < Tg < 165° C)[5] allows to consider the matrix very rigid at room temperature thus preventing the thermal motion of the imbedded dipoles. Additionally, a high NA objectives (NA = 1.4) has been used for the imaging.

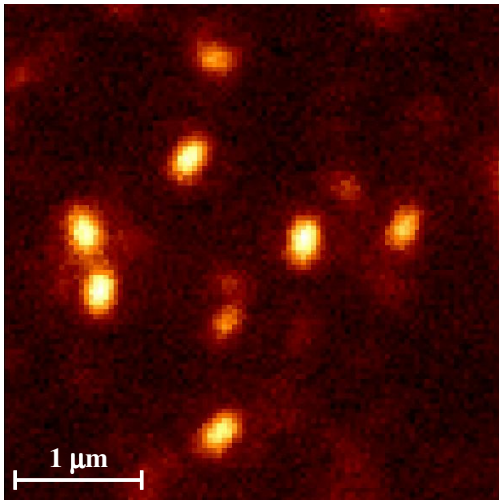

Figure 5.5: Survey image of the investigated sample. Elliptical PSFs generated by single Alexa Fluor 488 molecules embedded in a PMMA thin film. Vertically polarized laser light (Ar^+ laser, λ_{exc} = 488 nm) is used as excitation.

Figure 5.5 shows an image of the sample obtained with the Wide Field Fluorescence Microscope. Laser excitation at 488 nm is linearly polarized along the Y-axis of the image (Y- Polarization). Several bright spots, consisting of individual PSFs, are visible and the concentration of Alexa Fluor 488 molecules is such to allow single molecule analysis.

Commonly in microscopy the PSF patterns are modeled by using Gaussian function instead the Airy formula to facilitate the calculations and because the error made is negligible[6-8]. This happens as result of the non ideal imaging capability of the system that introduces various sources of noise (photon-count, pixilation, background, read-out noise) preventing ideal imaging. The generated noise "contaminates" the PSF such that the fitting with Gaussian function is considered acceptable. In this work the model proposed by Wolf is replaced by a 2-Dimensional Gaussian curve calculated by considering the widths along the two axes as independent parameters.

Figure 5.6 illustrates a direct comparison between the modeling of the cross section of a single PSF obtained by using Wolf's formula and the 2-D Gaussian function. The widths of the two curves differ of about 5%. Even though the presence of the first outer ring is noticeable from the Wolf's curve, its amplitude is comparable or even smaller than the background noise. Therefore, the modeling of the PSF might be achieved with the use of a function, such as the 2-D Gaussian, that does not contain terms regarding the outer rings.

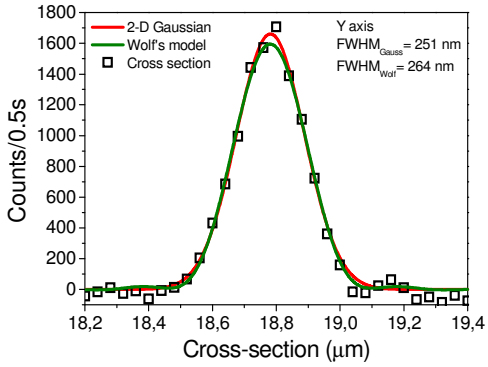

Figure 5.6: Comparison between the Wolf's formula and 2-D Gaussian function in the modeling of the cross section of a single PSF. The amplitude of the outer ring, generated by Wolf's model, results comparable or even smaller to the background noise.

To introduce and explain another parameter of the Gaussian function applied, it is necessary to consider a particular feature of the sample under investigation. As suggested, each single dipole holds a fixed orientation inside the polymer matrix. Nevertheless, polymer chains and fluorescent molecules when in solution (solvent) possess high mobility. Once the solution is spin coated on the glass substrate and the solvent evaporates, the polymer chains "solidify" into the rigid glassy matrix. This process preserves the orientation of the fluorescent molecules leaving the dipoles randomly oriented in the matrix.

The elongated shape of the PSFs, as visible in Figure 5.5, suggests and supports the validity of the starting hypothesis. The in-plane orientation of individual dipoles recalls the postulated random orientation.

Let us consider only the in-plane (X-Y) orientation of the dipoles. The model of Wolf describes how the PSF elongates in the direction of the dipole orientation. If a non-rotating dipole is oriented 40° respect the X-axis consequently the PSF will follow its orientation, and the long axis of the ellipse will be oriented 40° respect the X-axis. The random orientation of the fluorescent dipoles in the focal plane determines the orientation of the elliptical PSF. The image will consist of an ensemble of elliptical PSFs randomly oriented as suggested by Figure 5.5.

If the width of the PSF along two orthogonal directions presents different values, consistent with Wolf model, the change in the PSF shape will be demonstrated. To directly support the elongation of the PSF, measurements of the ellipticity of PSFs (ratio between the long and short axis) and of the in-plane orientation of the long axis have been performed by using two different orientations of a linearly polarized excitation light. Highly polarized laser light along Y-axis (Y- polarization) and X-axis (X- polarization) have been used as excitation sources. The intensity of the excitation light applied for the Y-configuration is higher than the intensity used for the X- configuration, thus

resulting in a higher photon counts (brighter PSFs) in the vertical excitation. Images of the illuminated areas containing several single Alexa Fluor 488 molecules have been taken at 2 Hz frame rate. PSFs present in the area have been individually modeled by a 2 dimensional Gaussian function.

Figure 5.7 illustrates the results of the analysis concerning the ellipticity of PSFs and the orientation of the dipoles. The distributions illustrated in the figure consist of several hundreds of individual single molecules. The elliptical shape of the analyzed PSFs is demonstrated by calculating the ratio between the two axes of the 2-dimensional PSFs. Results show single emitters to generate PSF which axes differ of about 20%.

The only selection rule used for the analyzed PSFs concerns the intensity of the emission. However, to improve the fitting procedure only objects well separated from others are analyzed. Nevertheless, erroneous fitting is still present as visible from the shoulders of distributions at higher ratio values. This feature is only visible at higher ratio values.

Molecules are recognized by the software as spots presenting a minimum of 5 pixels all having a count above a threshold. In the case of Y-polarization the threshold is fixed at 400 counts, while in the X-polarization configuration is 300 counts, since the last has been performed using a lower excitation power.

The first to graphs of Figure 5.7 (orange) depict the integrated count distribution of the analyzed molecules. The mean value of the emission count rate in the Y-configuration is ~25000 counts/per frame, while in the X- configuration is ~12000 (due to the different excitation power). Afterwards, the selected molecules are analyzed by the 2-dimensional Gaussian and the values of the axes of the elliptical PSFs are calculated and used to evaluate the ratio between the two axes. Blue graphs in Figure 5.7 represent the distribution of the values of the ratio of the two axes for each analyzed molecule. In both cases, Y- and X- configuration, PSFs present elliptical shape with ~ 1.25 ratio value between the long and short axis.

Ellipticity of the PSF, modeled by Richards and Wolf, is here experimentally verified and achieved. Single molecules when emitting polarized fluorescence and when imaged by a high numerical aperture objective, generate elliptical PSFs which ellipticity, represented by the ratio of long/short axes, agrees with the theoretical model.

Additionally, because of the demonstrated elliptical shape, it is possible to estimate the in-plane orientation of the imaged dipole. The last two graphs (black) of Figure 5.7 shows the distribution of the orientation of the molecules when illuminated in the Y- and X- polarization. The angles here represented are the angle formed by the long axis of the PSf with the x-axis of the image.

In the Y- configuration, the angle distribution presents its mean value around 90° with respect the x-axis of the image, while in the X- configuration the mean value is 0°. This result is not surprising.

A dipole can only be excited by a linearly polarized light when it possesses a component along the direction of the polarization of the illumination. A dipole orthogonal to the polarization of a linearly polarized light will not get excited. In the case of the sample used here, only those molecules with a component of their dipole along the direction of the polarization can absorb/emit photons. The sample consists of several single molecules embedded into the PMMA matrix with random orientation. When the solution containing PMMA and Alexa Fluor 488 molecules is spin coated onto the glass substrate, the embedded molecules will be "frozen" into the thin polymer film with random orientation.

When the sample is illuminated with Y- polarization excitation light, only the molecules presenting a dipole component along the Y- direction can be excited. Analogue is for the X-polarization. So, the molecules observed in the Y-configuration will present distribution of orientation around the direction of the polarization of the light (Y-axis → 90°), while those molecules observed in the X-configuration will have a distribution of angles around 0° (X-axis →0°).

This very point is crucial for the discussion. In fact, the intimate relation between orientation of the molecules with respect to the linear polarize excitation light (angle distribution) and the ellipticity of the imaged PSFs (ratio long/short axes) perfectly agrees with the theoretical model.

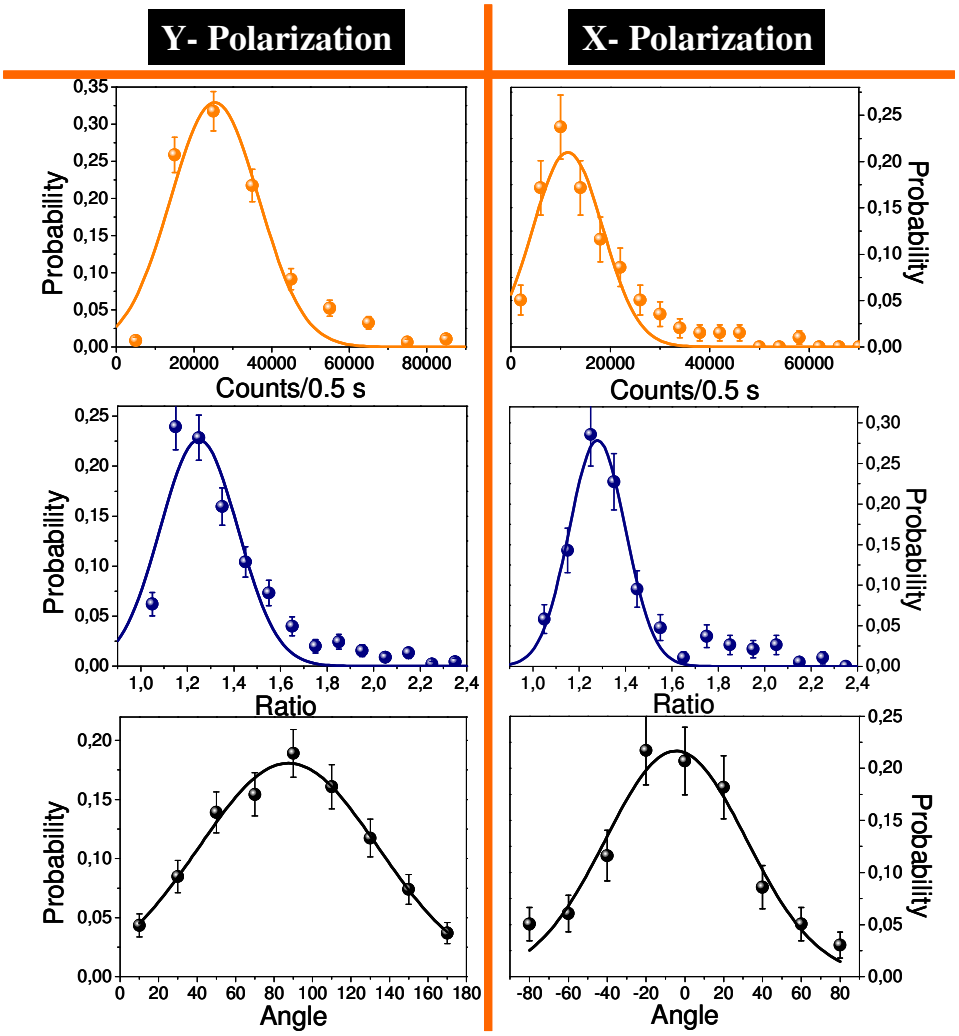

Figure 5.7: Integrated emission, long/short axes ratio distributions and angle distributions of in-plane angle of single dipole emitters along two polarization's directions as measured from imaged PSFs. The angle measured is between the long axis of the ellipse and the X-axis. Ratio distributions present in both the excitation configuration a mean value of ~ 1.25. Angle distributions posses mean values (90° in Y- configuration, and 0° in X-configuration) in agreement with the theoretical model.

After the survey analysis of the sample concerning the angle distribution and the ellipticity of the imaged PSFs, a more detailed analysis is presented in Figure 5.8 focused on the actual values of the short and long axes.

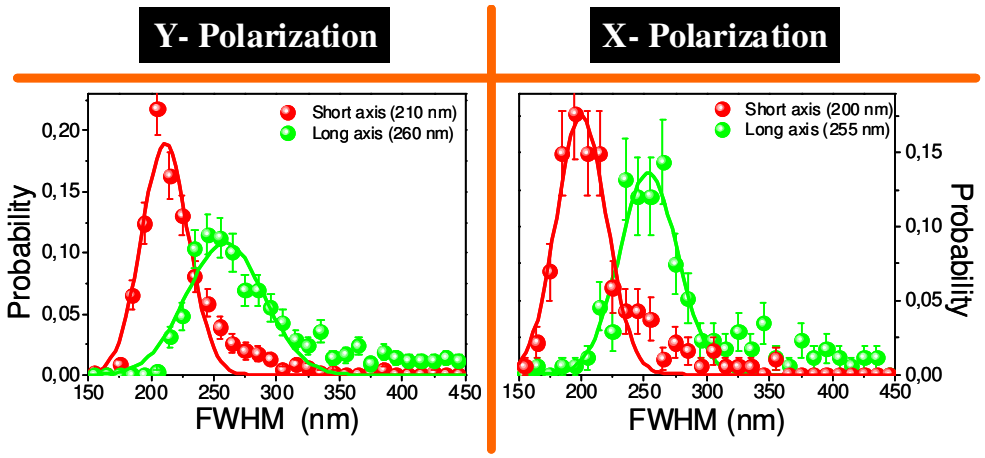

Figure 5.8: FWHM of the long and short axes. The erroneous fitting values are represented by the shoulders of distributions at higher values. The four graphs represent 2 polarizations and 2 groups of molecules.

Figure 5.9 shows the distributions of values of the projection on X- and Y-axis of the standard deviation (σ) of Gaussian functions (σ = FWHM/2.35) obtained from the brightest molecules. It is introduced to clarify how the orientation of a single dipole might affect the position accuracy along the two main dimensions (X- and Y-axis) of the image. The sigma values are also shown because used afterwards in the section concerning the super resolution.

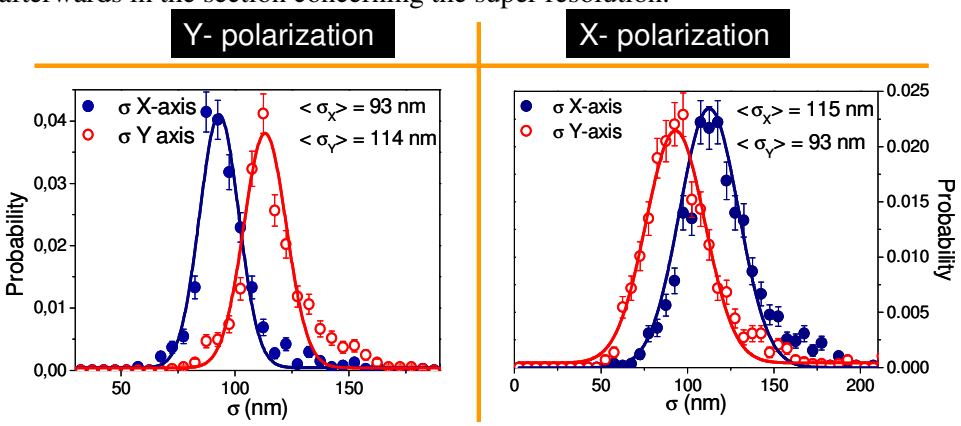

Figure 5.9: Distributions of the widths (σ) of the PSF along X- and Y-axis of single dipoles embedded in a glassy polymer matrix (PMMA) and measured by irradiating with vertical (Y-axis) and horizontal (X-axis) linearly polarized laser light. Red points refer to σ measured along y direction and blue points to σ measured along the x direction. The shift between distributions supports the consistency of Wolf model.

The model predicts the width of the PSFs to be larger along the direction of the excitation's polarization. Red data points refer to the measurements of the σ of the 2-dimensional Gaussian curve in the y direction, while the blue points are relative to the values along x. For both the excitations the σ_Y and σ_X distributions are clearly shifted apart. The distribution relative to long axis displays a mean value of 114 nm, while the short axis is 93 nm.

The direct measurements of the widths of PSFs prove that imaging single dipoles having fixed orientation through high numerical aperture lens results in a non-isotropic light distribution in the focal plane.

5.3.2 Control measurements (a): Fluorescent Beads

As mentioned, the model proposed by Wolf is valid in non-paraxial approximation and for polarized light emitters. Control measurement shows that for a point-like source consisting of uncorrelated emitters the PSF obeys the more general case and appears isotropic in space (circular shape). A sample consisting of single fluorescent beads with radius ~ 20 nm has been used as point-like sources of unpolarized fluorescent emission after illumination by Y- polarized laser light.

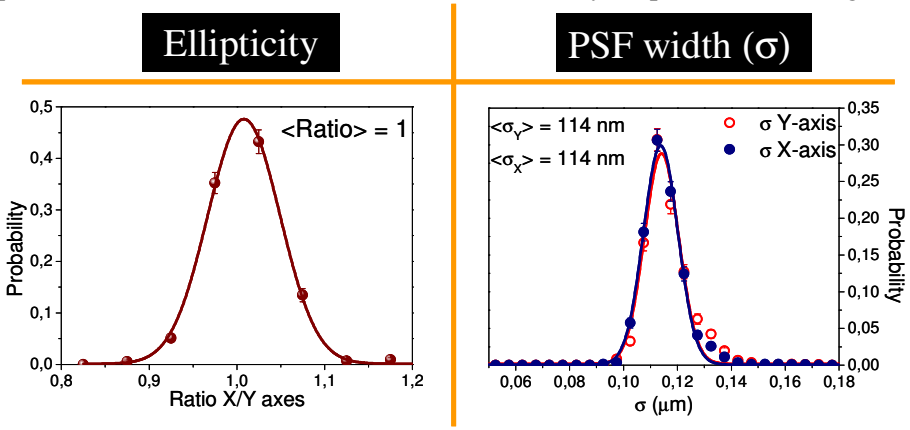

Figure 5.10: Ellipticity measurements and width along the two axes of PSFs produced by fluorescent beads. The value of the ellipticity and the widths show the analyzed PSFs to be circular.

Figure 5.10 presents the results of the analysis of the imaged PSFs. The measured ellipticity equals the unity as supported by the direct measurements of the size of the PSFs axes.

The observed change in the spatial distribution of the PSF is only present when the conditions assumed in the theoretical model are satisfied. The same experiments have been performed with the fluorescent beads and with single dipole embedded in the polymer matrix, but the PSF assumes elliptical shape only when generated by polarized light.

Figure 5.11 summarizes the main features discussed in the paragraph and the control test. Images of single fluorescent molecules (Alexa Fluor 488) are shown in both the direction of the polarization used and the relative cross-sections along the two axes together with images of fluorescent beads presented as comparison. The cross-sections of the uncorrelated source are equal along the two axes and with the two polarizations applied.

It has been demonstrated that the PSF undergoes a geometrical change if obtained with high NA lens in combination with a highly polarized light source. The reported effect should be considered in all the analysis involving the value of the size of the PSF, such as the so called super-resolution microscopy.

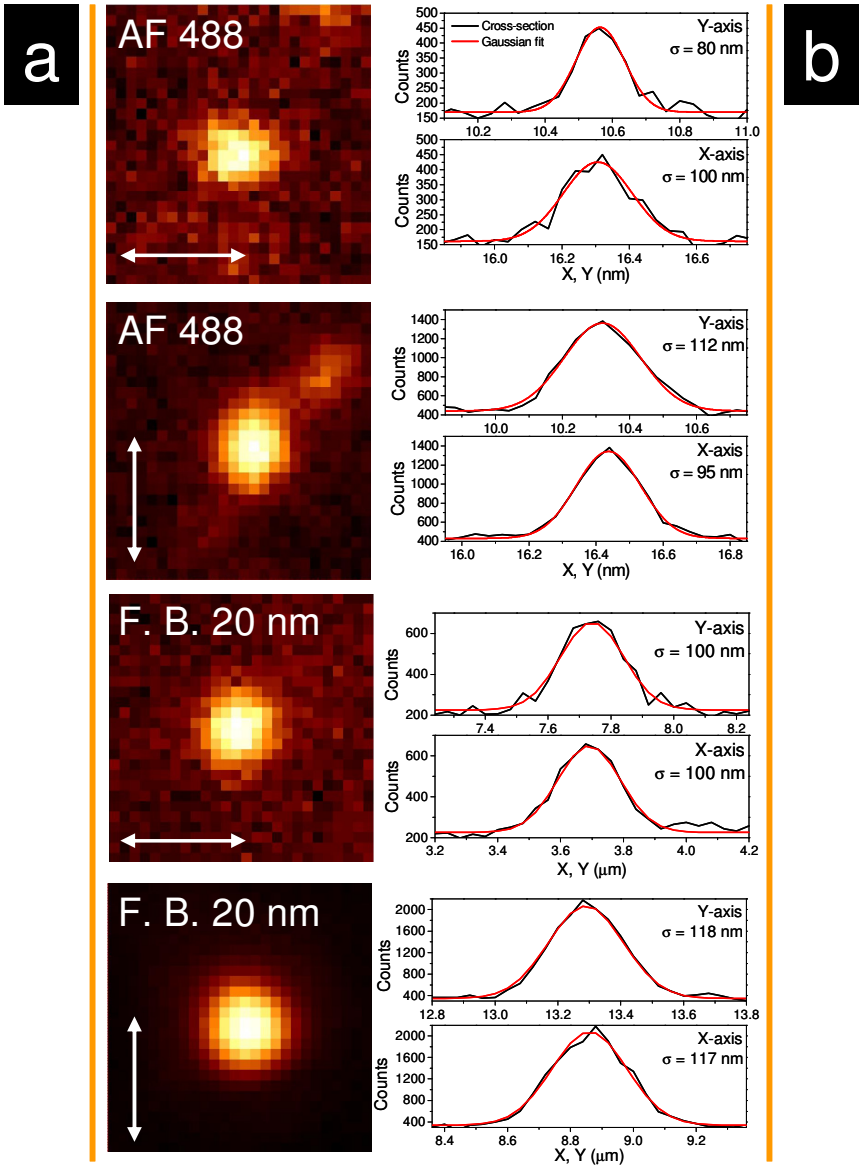

Figure 5.11: Images of PSFs of single dipole emitters (Alexa Fluor) and of fluorescence beads (a) obtained with different polarization of the excitation light (arrows). The corresponding cross-sections and the fit obtained with 2 dimensional Gaussian function (b) underlines the changes in the width of the PSF to be present only in presence of a polarized light emitter, and to follow the model described by Wolf (see Ref. 4).

5.4 Super resolution microscopy

5.4.1 Definition and theoretical limit

By the term optical resolution of a microscope is indicated the least distance (separation?) two point-like sources of light require to be optically resolved. It has been already explained that due to light diffraction photons emitted from a point-like source are imaged with a broader spatial distribution that is described by the Airy disk formula[2, 3]:

$$I(0,v) = \left(\frac{2J_1(v)}{v} \right)^2$$

The minima of I as function of v correspond to the zero of the $J_1(v)$ function. In particular the first three zeros are found at:

1^{st} zero $\rightarrow$ $v_0 = \pm 1.22\ \pi$

2^{nd} zero $\rightarrow$ $v = \pm\ 1.63\ \pi$

3^{rd} zero $\rightarrow$ $v = \pm\ 2.23\ \pi$

The first zero is the one determining the resolution and gives the size of the Airy disk. From the definition of v it is possible to calculate the distance off axis corresponding to the first zero. Therefore, r_0 is the least resolvable distance (optical resolution).

$$v_0 = 1.22\pi = r_0 \cdot \frac{2\pi}{\lambda} NA$$

$$r_0 = 0.61 \frac{\lambda}{NA}$$

Figure 5.12 illustrates the cross-section of a PSF and the position of the first zero.

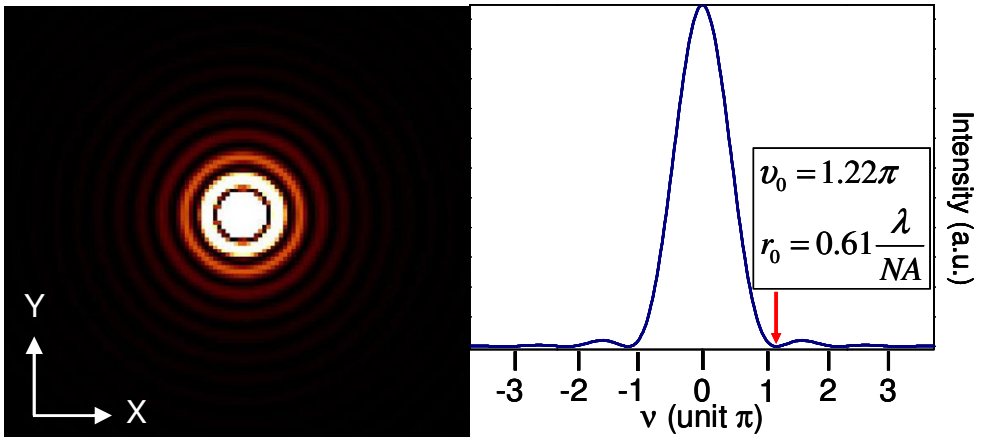

Figure 5.12: Intensity distribution of light in the focal plane. The size of the central disk (Airy disk) determines the least resolvable distance. On the right the cross-section of the distribution is shown.

Figure 5.13 is introduced to facilitate the understanding of the optical resolution of a microscope and to highlight its limiting effect. Figure 5.13, a and b, shows identical distributions of light from four point-like emitters (blue curves). In a two emitters are placed at a distance such that the maximum of one distribution is positioned as the minimum of the second.

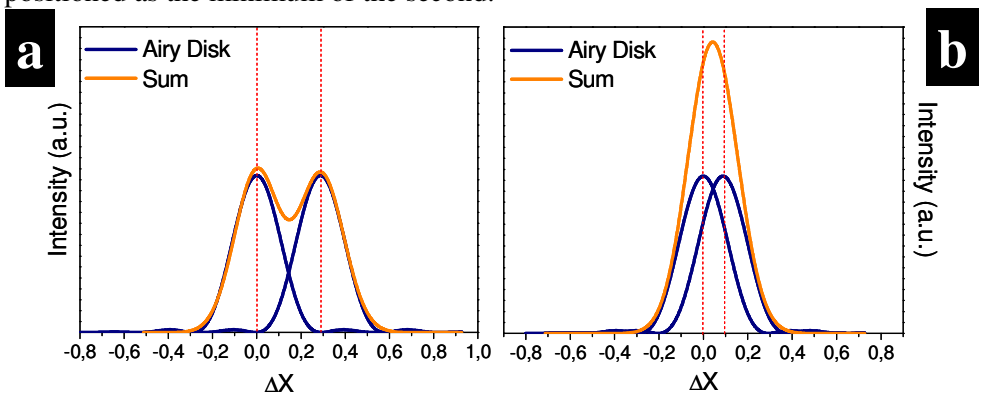

Figure 5.13: Panels a and b illustrate the overall distribution arising from two emitters when positioned at a distance equal to the resolution (a), and when placed closer (b). In a the distance of the emitters is such that the maximum of one emitter coincides with the zero of the other and the sum distribution allows the two sources to be resolvable. In b the distance of the emitters is smaller than the resolution and therefore it is not possible to distinguish them from the sum.

In this situation the distance between the two sources coincides with the resolution. The overall (sum) distribution of photons, represented by the orange curve, allows the resolution of the two individual sources. In the panel b, the two emitters are

placed at a closer distance and the sum-distribution appears like a single, more intense, source. In this case, it is impossible to resolve individual emitters.

The resolution of a light microscope it is commonly taken being around 250 nm and any smaller emitter will appear as a diffraction limited spot in the image[9]. Let assume that a single molecule dye is imaged, and assume as well that the size of the molecule is around 1 nm. The accuracy concerning the position of the molecule in the image is limited to the 250 nm size of the corresponding Airy disk. Single molecule fluorescent microscopy approach to investigate matter at nanoscale has required the bypass of the diffraction limit.

Last decade have seen the explosion of several successful approaches meant to overcome the diffraction limit[10-15]. Those methods have originated the so called: "Super-resolution microscopy". An *a priory* knowledge of the distribution of collected photons allows the determination of the position of the centre of the Airy disk with an accuracy of few nm[16, 17]. Diffraction theory and the solution concerning the light distribution in the focal plane of a lens (Airy formula and Gaussian function used as approximation) provide the tool to spatially characterize the emission pattern. Even if the details in the spot are not resolvable, its center, and therefore the position of the emitter, can be estimated with accuracy two orders of magnitude higher. Several are the parameters affecting the value of the accuracy. A theoretical model is used to evaluate the limit concerning the reachable accuracy.

The model presented by Thompson et al.[17] is introduced here and used to estimate the theoretical limit for the accuracy in resolving the position of point-like source beyond the diffraction limit. Although frequently applied[10], the authors point out that the model gives values 30 % higher (better accuracy) with respect experimental measurements when the PSF is fitted with a 2 dimensional Gaussian function. The model consists in the characterization of the signal-to-noise ratio in which terms concerning the light source, optics, and the detector (CCD) are considered.

Thompson expression for the theoretical accuracy achievable in 1 dimension takes the form:

$$<(\Delta x)^2>=\frac{s^2+\frac{a^2}{12}}{N}+\frac{4\sqrt{\pi}s^3b^2}{aN^2}$$

where:

$<(\Delta x)^2>$ = Standard Error of the Mean (SEM) (Gaussian or Airy)

s = standard deviation of the Point Spread Function

a = pixel size

N = number of collected photons

b = background noise

The achievable accuracy is mainly affected by two terms: photon noise and background noise.

$$\text{Photon Noise} \qquad <(\Delta x)^2> = \frac{s^2 + \frac{a^2}{12}}{N} \qquad \text{if } s > a$$

The term $\frac{s^2}{N}$ gives the error introduced by the light source itself, or better by the photons emitted by the source. Each photon collected gives information about the position of the emitter; any measure (photon) has an error in the positioning which is equal to the standard deviation of the point spread function of the microscope. As said before, the PSF indicates the resolution of a microscope, thus its error. A microscope cannot evaluate from which point inside the PSF a photon comes.

The term $\frac{a^2}{12}$ represents the increase in error due to the finite size of the pixel, or Pixelation noise. It is not possible to estimate the position within the pixel where the photon has been detected.

$$\text{Background noise} \qquad <(\Delta x)^2> = \frac{4\sqrt{\pi}s^3b^2}{aN^2}$$

The term describing the background noise is a bit more complicated. The authors applied the criterion of least-squares fitting to estimate the minimum of the sum of squared errors. To facilitate the solution of the equations, they substitute a sum with an integral thus not considering the finite size of the detector element (pixel size). That is why in the background noise formula the pixilation term does not appear, a at the denominator is added to make units correct.

Let us assume, for instance, that the pixel size is about the PSF, thus the ratio s/a will be simply 1. If $s > a$, the accuracy will decrease ($<(\Delta x)^2>$ grows) since each pixel included in the PSF region will introduce additional uncertainty.

The model shows that the accuracy goes as $\frac{1}{\sqrt{N}}$ for photon counting noise and as $\frac{1}{N}$ for background noise. The localization accuracy in case of low photon-count is dominated by the background term, while with high photon-count the photon noise term is predominant.

5.4.2 Experimental verification

5.4.2.1 Unpolarized emitter

In order to verify experimentally the possibility to achieve details beyond the diffraction limit, the position of fluorescent beads (radius ~ 160) nm is measured on a substrate surface.

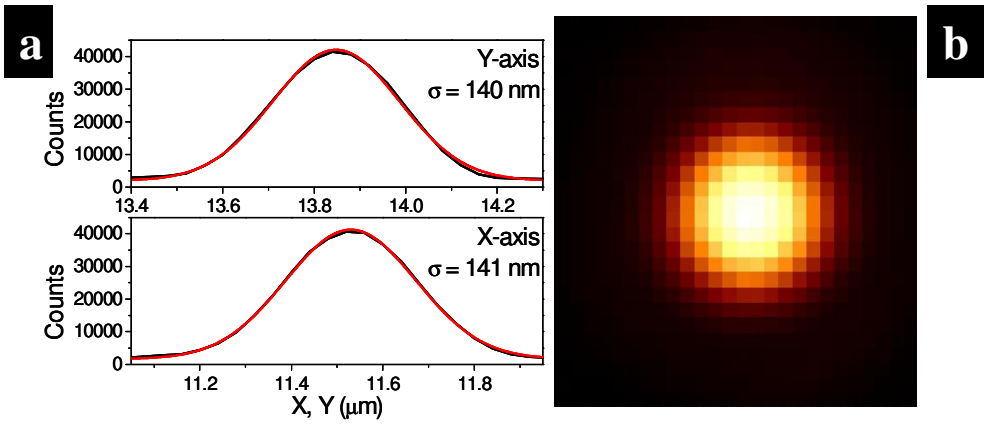

Figure 5.14: In a, the black curves indicate the cross-sections (X, Y) and the red lines the fitting curves obtained by Gaussian function of the single fluorescent bead imaged in b. The size of the imaged area is 1 μm.

Figure 5.14 shows the PSF of a single fluorescent bead in section b, and the cross-sections of the same emission peak together with the obtained Gaussian fit in a. By fitting the PSF with a 2 dimensional Gaussian function it is possible to extrapolate the standard deviation of the PSF (*s*), from the cross-section the number of collected photons (N). The noise (*b*) is calculated by averaging the standard deviation of the background signal measured in several pixels.

The isotropic shape of the PSF reflects the unpolarized emitted light, thus the PSF is well described by the usual Airy disk.

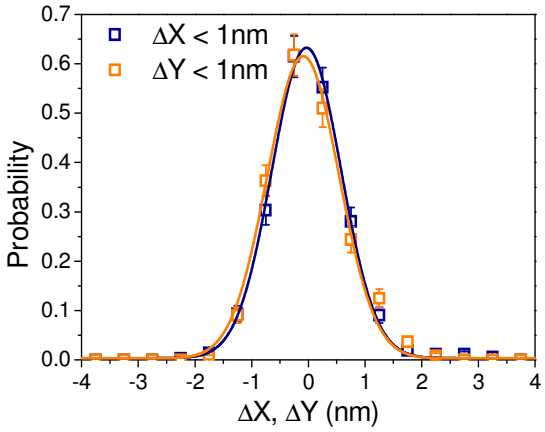

Figure 5.15: Distributions of the measured value for the position of several single fluorescent beads. Distributions are obtained independently along the two axes and consist of more than 1000 measurements. Gaussian functions have been used to model the distributions. The standard deviation of the curves resembles the accuracy of the positioning measurements. The accuracy along the two axes is ~ 1nm.

Experimental evidence of the super-resolution microscopy is presented in Figure 5.15. A vertically polarized laser light has been used to illuminate an area containing several single fluorescent beads. Images have been taken at 2 Hz frame-rate. The relative position (in the imaged area) of single emitters is measured and normalized according to each relative mean value to obtain an absolute mean position equal to zero. The mean value of all the measurements results to be centered at zero, and the deviations from it provides the error/accuracy in the positioning.

In Figure 5.15, blue points and curve refer to position/accuracy along the X-axis, while the orange points indicate the Y-axis. Each distribution consists of more than 1000 measurements. By fitting the two distributions with a Gaussian function, the standard deviation of the curve, and consequently the accuracy (width of the Gaussian), is calculated. The obtained value for the accuracy in the position of single fluorescent beads is ~ 1 nm, thus improving by two orders of magnitudes the diffraction limit. The measured accuracy value is the same along the two main axes.

The experimental results support the possibility to reach details beyond the diffraction limit. Further, the measured accuracy along X- and Y-axis coincides as expected by the isotropic geometry of the PSF of an unpolarized emitter.

5.4.2.2 Polarized emitter

From Thomson equation, it is possible to approximate (to some extent) the value of the accuracy as directly proportional to the value of the standard deviation of the PSF (σ).

$$< \Delta x > \propto \sigma$$

The anisotropic shape of the PSF, documented in section 3.3 of this chapter, might affect the correct evaluation of the accuracy. In order to investigate this point, the same positioning measurements aforementioned have been performed by using single dipole emitters (Alexa Fluor 488) embedded in PMMA matrix. The sample is the same used in section 3.3 of this chapter. Vertically polarized laser light is used as excitation.

Similarly to the previous paragraphs, the values of parameters used in Thompson model, are directly obtained as depicted in Figure 5.14. Here the values are presented in order to directly compare the experimental and theoretical values.

The pixel size (a) is determined by the magnification of the microscope; in this case a = 40 nm. Values obtained for a single Alexa Fluor emitter along the X-axis are:

s = 90 nm,
a = 40 nm,
N = ~9000,
b = 32
The theoretical limit for the position accuracy is:

$<\Delta x>$ = 1.7 nm → experimental correction (+30%) $<\Delta x>$ = 2.2 nm

Experimental evidence of the super-resolution microscopy analysis is presented in Figure 5.16. Panel a and b present the distributions of the measured values of the position around the "zero" mean value. All the graphs are obtained with ~ 500 measures.

Because of the high sensitivity of the measurements, the influence of the piezo stage has been estimate separately by repeating the measurements with the piezo stage on and off. The distribution depicted in panel a of Figure 5.16 is obtained with the piezo stage off. Blue points refer to the position along the X-axis, while the red points along the Y-axis.

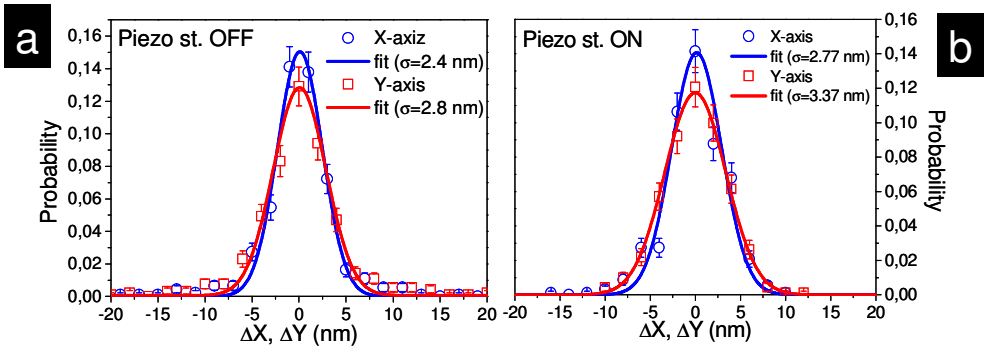

Figure 5.16: Panel a and b show the distribution of the measured value for the position of several single molecules with and without the piezo stage. Distributions are obtained independently along the two axes and consist of more than 500 measures. Gaussian functions have been used to model the distributions. The width of the curves, giving the accuracy, is indicated by the sigma value. Values are consistent with the theoretical model, and a 20% difference is observed along the two axes.

By fitting the two distributions with Gaussian function the value of the accuracy obtained are: $<\Delta x>$ = 2.4 nm (± 0.1 nm) (X-axis), and $<\Delta y>$ = 2.8 nm (± 0.1 nm) (Y-axis). They both are consistent with the expected theoretical limit value 2.2 nm. The sub-nanometer deviation might be due to not ideal experimental conditions (vibrations, or nanometer range drift of the sample). Panel b shows the results obtained with the piezo stage on to be consistent with the results in panel a.

The accuracy along the Y-axis appears to be about 20 % lower respect the value along X-axis. A small deviation is nevertheless observed. The elliptical shape of the PSF affects the value of the accuracy along the two orthogonal directions.

In order to directly prove the potential to "read" displacements beyond the diffraction limit, steps of 10 nm along the X-axis driven by the piezo stage, have been measured.

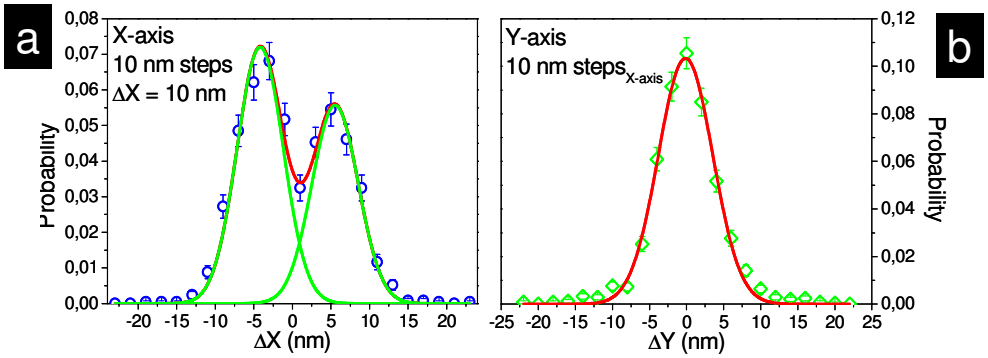

Figure 5.17: In panel a and b are depicted the displacements induced by the piezo stage along the X-axis (a) and Y-axis (b).

Figure 5.17 illustrates the displacements measured in different movies while the piezo stage performing a single 10-nm step along the X-axis. The specifications of the piezo stage and the measurements of the accuracy (when the piezo stage on) guarantee position-accuracy around 1 nm. The piezo stage has been programmed to perform a single 10-nm step (in each single movie) in a time shorter than the integration time for a single frame to reduce "stroboscopic" effect to a single frame hence not considered in the displacement analysis. The steps have been measured by tracking the positions of single emitters embedded into a polymer matrix. The sample is the same described above (thin film of PMMA and Alexa Fluor 488).

Panel a of Figure 5.17 presents the displacement performed by molecules in the x-direction. Each position-measurement has been obtained by fitting the PSF with Gaussian function as described previously. The distribution of the positions presents two peaks. By fitting the two peaks with Gaussian function it is possible to determine not only the width, as for the case of the accuracy measurements, but the distance from the two peaks. The displacement of the two peaks is 10 nm, consistent with the induced motion by the piezo stage, and the peaks have a $\sigma \sim 3$ nm according to the accuracy tests.

The peak on the right presents lower intensity compared to the peak on the left because of photobleaching events of the tracked molecules. The second peak resembles the final position of molecules after each step, thus the final time instant. This results as consequence of the procedure adopted in the experiments which is therefore here described.

To avoid additional "noise" to the position determination, it has been necessary to avoid the hysteresis of the piezo material. First a long step (1 μm) has been performed to the left (decreased x), then a step of the same amplitude to the right. From this final position steps of 10 nm have been performed. The distribution presented in Figure 5.17 consists of the analysis of several movies in which the step have been induced always along the same direction. Thus the position described by the left peak represents the initial time-position, while the peak on the right the final.

The influence of photobleaching is time-dependent. As longer is the time interval an ensemble of molecules is irradiated, as fewer molecules will be fluorescing at the end of the interval. The difference in amplitude of the two peaks in Figure 5.17 panel a is due to this effect. The amplitude of the right-peak is lower simply because fewer molecules are observable or (as in this case) they are visible for shorter time respect the initial position. Consequently, the statistics on the initial position are lightly higher. Nevertheless, both peaks consist of several hundreds of measurements.

In panel b of Figure 5.17 is presented the displacement along the y-direction of the same molecules used in panel a. The distribution consists of a single peak, as expected being the motion along X-axis, with $\sigma = 3.5$ nm in agreement with the accuracy measurements with piezo stage on.

5.4.2.3 Polarization analysis

The analysis of the accuracy represented in Figure 5.16 highlights the difference along the two axes. The accuracy measured in the x direction (σ_X=2.4 nm) is 20% higher respect the accuracy measure in the y direction (σ_Y=2.8 nm). The accuracy value, base of the super-resolution techniques, follows the results presented in the paragraph 3.3. If a single dipole oriented in the y direction is irradiated with a vertically polarized light, the accuracy measured along the y direction will result 20% lower than the accuracy in the x direction.

In order to investigate the dependence of the accuracy along the two axes on the orientation of the dipole emitter, measurements obtained with vertically polarized light are compared to results obtained with horizontally polarized light. Figure 5.18 compares the accuracy measurements done with linear polarized light at two different orientations. The distribution presented in the vertical polarization configuration is the same presented in Figure 5.16.

Distribution (> 800 measurements) obtained for the horizontal configuration was measured irradiating the same sample, imaging with the same frame rate (2 Hz), but by applying a lower excitation intensity.

In the distributions shown in Figure 5.18, the accuracy along the two axes differs of about 20% as result of the 20% difference in the size of the PSF along the two directions.

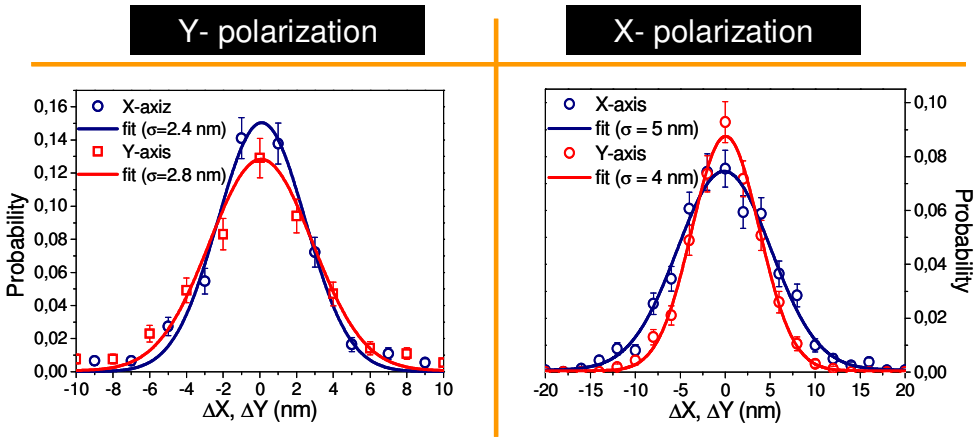

Figure 5.18: Distribution of the measured position of several single dipoles obtained by applying linearly polarized Y- and X- oriented. The graph illustrating the Y polarization is the same depicted in figure 9 (piezo stage off). The curve obtained for the X- polarization consists of > 800 measurements. In both curves the accuracy along the two directions differs of about 20%. The axis with the higher accuracy is, in both cases, the one orthogonal the polarization of the excitation.

Supporting further what discussed in the previous paragraph, by rotating 90° the direction of the polarization of the excitation light the axis with higher accuracy (short axis of the elliptical PSF) rotates consequently

5.4.2.4 Control measurement (b): Fluorescent Beads

Similarly to the previous control measurements, here the super-resolution accuracy value has been evaluated by using fluorescence beads with 20 nm radius. As expected by the circular shape of the PSFs, demonstrated by the measurements reported in Figure 5.10, the values of the accuracy along the two axes coincides. Figure 5.19 illustrates the distribution of the position of several beads around a mean value. The width of the distribution, 4.1 nm, corresponding to the value of the accuracy is equal along the two main directions (X-axis and Y-axis).

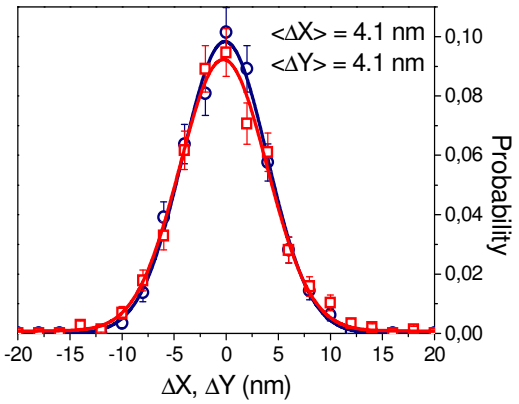

Figure 5.19: Distribution of the measured position of several fluorescent beads obtained by applying linearly polarized vertically. The measured value of the accuracy is constant along the two main axes.

5.4.3 Excitation intensity influence

The different width of the distributions (Figure 5.9) obtained with Y- and X-polarization configuration is caused by the different intensity of the excitation light used and therefore by the fluorescence signal intensity. In the intensity range applied (no saturation effect), to higher excitation intensity correspond higher fluorescence intensity; therefore the signal-to-noise ratio improves (see cross-sections in Figure 5.11). The higher intensity of the Y- configuration light determines the narrower distribution (17 nm) respect the one obtained with X-polarization (34 nm). The higher signal-to-noise ratio in the Y- polarization experiment improves the fitting process of the PSF, therefore reducing the error represented by the width.

This should not mislead the results obtained, since with both the polarizations and intensity the mean values are the same. The intensity of the excitation light applied, and thus the fluorescence emission, affects the distribution's width of the measured values (accuracy of the measurement), but not the mean value which is the value under investigation. The broader distributions of values for the sigma of

the PSF shown at X- configuration will affect the following analysis concerning the super resolution accuracy. Naturally, the value of the accuracy along the x-axis ($<\Delta x>$ = 2.4 nm) obtained with Y- polarization should be compare to the value obtained along the y-axis ($<\Delta y>$ = 4 nm) for the X- polarization (Figure 5.18). The error made in the fitting of the PSF depends on the signal-to-nose ratio. That same error determines also the accuracy being $<\Delta x> \alpha (<\sigma_{PSF}> \pm$ error).

5.5 Single molecule dipole orientation

5.5.1 Introduction

The *a priori* knowledge of the mathematical description of the Point Spread Function has provided scientist the possibility to obtain an optical accuracy far better than the Abbe's limit, thereby boosting the applicability of fluorescent microscopy in the study of matter at nanoscale. In addition, the single molecule sensitivity has shown the uniqueness of the behavior of molecules caused by the inter-molecular interactions of each single molecule with their environment. Early single molecule experiments have shown that changes in photophysical properties of single emitters, for example the absorption and emission spectra, only occur in presence of environmental changes[18-21]. These developments opened the possibility to study the environmental dynamics through single molecule spectroscopy. The course dynamics may be followed by recording the position of the emitting molecules (see Chapter 3) or by monitoring the single molecule emission spectra[19]. An alternative and more elegant method to study the environmental dynamics is to follow the orientation of the single emitter dipoles[21-24].

This makes use of the possibility to characterize the three dimensional orientation of single emitters from defocused fluorescent microscopy images[24]. This method has, however, one drawback in that it degrades the positional accuracy. Nevertheless, the study and modeling of single fluorescent molecules patterns imaged using 1 μm defocussing can provide detailed characterization of the orientation of the emitting dipole, and it has for instance been used to investigate the dynamics of a polymer matrix close the glass transition temperature[24].

Despite the great achievement provided by the defocus imaging, which in fact extends the field of applications of single molecule fluorescent microscopy, the technique is inherently associated with an overall decrease of the signal to noise ratio (SNR) thus compromising the position accuracy. As introduced in the first part of this chapter, the accuracy in the position measurement depends on the SNR[25]; imaging at a defocused position of ~ 1 μm changes the pattern of the detected photons which become distributed over a wider detector area thereby reducing the SNR. To avoid this problem Selvin et al[26] have proposed to separately

image the emitter in focussed and defocused mode. Though this indeed yields high spatial as well as orientational resolution, it does require two images to be experimental complexity and limits the temporal resolution.

In the remainder of this chapter it will be shown that one can also obtain the required positional and orientational information from a single, in focus, image. To demonstrate the capabilities of this novel method, we will show that it can be used to determine both the position and the orientation of single fluorescent molecules attached to Teflon molecular chains stretched on a glass surface.

5.5.2 Defocus imaging to resolve molecular dipole orientation

Several reasons have boosted the interest on the experimental determination of the 3-dimensional orientation of molecule's absorption/emission dipole. First, the fluorescence lifetime and the emission intensity often depend on the orientation of the fluorescing molecule[27]. The relative orientation of the molecule dipole moment to the polarization of the excitation field (if linearly polarized) determines the extent of the absorption efficiency thus of the emission intensity.

Second, the eventual application of the orientation study has brought new insights concerning the photophysics of molecules[28], the structure of the dipole environment[24, 29, 30], and allowed the probing of the orientation of labeled biomolecules[31-34].

The first approaches applied to recover the orientation of single dipoles, such as polarization-resolved scanned imaging both in near-[19, 35] and in far-field[36, 37] optical configuration, were based on detecting the fluorescence signal on two channels cross-polarized. More recently, the defocus imaging approach has been largely adopted since based on direct images of the emitters.

Central idea is to gain information about the orientation of the fluorescent dipole by deteriorating the in focus image and gain access to the intrinsic heterogeneous spatial distribution of its field (see Figure 5.20). Though already achieved at cryostat temperature[38], the crucial improvement of detectors technology has allowed the experimental realization at room temperature[23].

Enderlein and Bohmer have reported the observation of the typical bipolar patterns corresponding to emitting dipoles parallel to the glass surface of the microscope coverslip, together with the first modeling of dipole defocus pattern at an interface[23]. Images of fluorescent dye molecules adsorbed at the glass-air interface have been obtained with integration time of 3 s. The authors underline the fact that the imaged dipoles were mainly oriented parallel to the surface because of the illumination configuration adopted. In fact, the wide field illumination area obtained with a circular polarized laser light does not present an electric field component along the optical axis (perpendicular to the surface). By enlarging the inclination angle with the surface, the fluorescence excitation efficiency decreases towards zero for a completely vertical dipole. The authors suggest that a total

internal reflection illumination of the sample would provide also a vertical component for the electric field enabling the imaging of dipoles with vertical component.

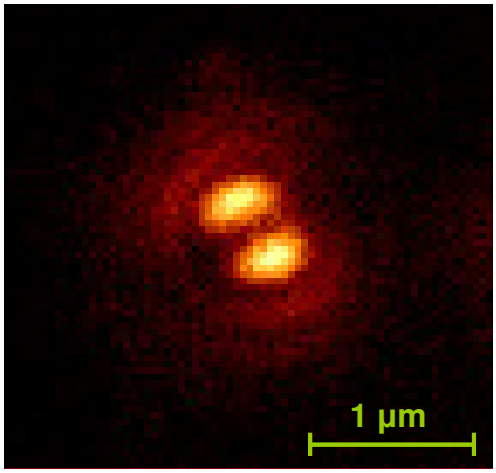

Figure 5.20: Emission pattern of a single molecule of Alexa Fluor 488 imaged with wide field fluorescent microscope at ~ 1µm away from the focal position of the objective. The pattern corresponds to a dipole parallel to the surface.

Nonetheless, the defocus imaging approach has proved its sensitivity on revealing the 3-dimensional orientation of single dipoles as demonstrated by Uji-i and Hofkens[24] in the study concerning the structural dynamics of a polymer thin film of PMA close to the glass transition temperature. They indeed observed that only 25% of the imaged dipoles posses a partially vertical orientation. As mentioned in the introduction, the defocusing weakens the signal-to-noise ratio thus decreasing the position accuracy. Uji-i and Hofkens[24] report that the pattern of a single imaged dipole covers an area of about 1 x 1 μm^2, similar to the size imaged in Figure 5.20. Comparing this with the diffraction limited pattern of single emitters (PSF) as presented in the previous part of this chapter, where the overall ensemble of detected photons covers an area of about 0.2 x 0.2 μm^2 and assuming the number of collected photons to be constant either in focus or defocus, one can estimate about one order of magnitude poorer position accuracy[25]. The defocusing method severely affects the accuracy in the positioning of the single emitters, key factor for all super resolution microscopy techniques (see Figure 5.21). A proposed method to gain both super resolution accuracy and orientation information of single emitting dipole has been suggested by Toprak et at[26]. They combined both the methods by imaging the same dipoles both while in focal and defocal positions. In this way they demonstrate the possibility to achieve super resolution position (focus image) and orientation characterization (defocus image) of the imaged dipoles. Two images of the same dipole are necessary. This illustrates the intrinsic

limitation of the methodology, since more experimental accuracy is required and a more limited temporal resolution is achievable.

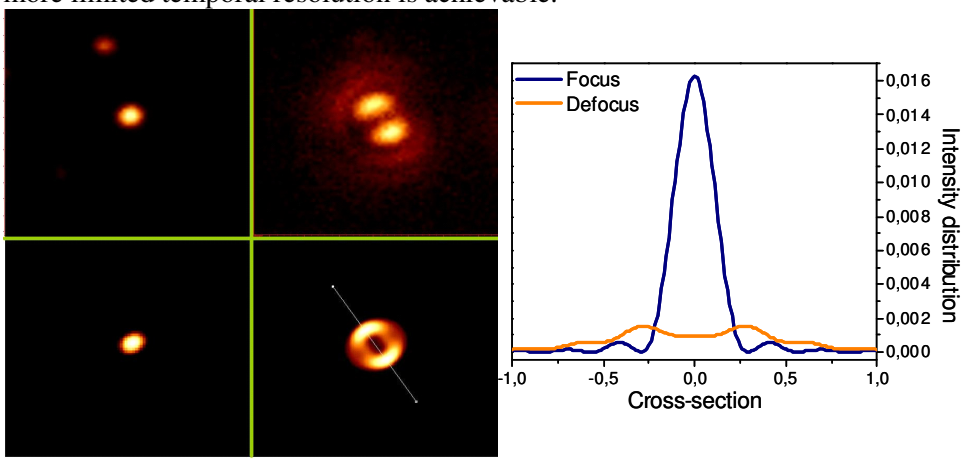

Figure 5.21: (Top) real images in focus (left) and ~1 μm defocused, and (bottom) corresponding simulation obtained by Wolf's formula. On the left, the graphs represent the cross-sections of the two simulated images. It is possible to appreciate the high difference existing between the signal-to-noise ratios between the focus and defocused images.

Experimentally, the difficulty lies on the accurate positioning of the objective in the two positions about 1 μm apart; the movement cannot occur too fast in order to avoid stress on the sample and the liquid drop (water or oil) used with high NA immersion objective. Further, the requirement of two images temporally affects the dynamics that can be investigated and surely it is sensitive to photobleaching. If a dipole bleaches within the total integration time required to get both the images, consequently the information will be partially reduced.

5.5.3 In focus imaging to resolve molecular dipole orientation and comparison with the defocusing technique

The in-focus imaging of single fluorescing dipoles (Alexa Fluor 488) embedded into a polymer matrix (PMMA) has revealed the experimental exploitation of the Point Spread Function (PSF) model proposed by Richards and Wolf in 1959[39]. In previous part of the chapter, it is discussed how the elliptical shape of the PSF affects the value of the position accuracy along the two main axis of the image (X, Y). The high accuracy value measured (~2 nm) positively supports the achieved super resolution microscopy. In the chapter, it is also proposed that the ellipticity of the PSF, elongation of the PSF along the dipole axis, might be used to unravel the orientation of the molecular dipole.

Here, it is proposed a direct comparison between the traditional defocusing method to extract the orientation of dipoles and the in-focus imaging that takes advantage of the elliptical shape of the PSFs of the imaged dipoles. The correlation

between the angles values obtained with the two approaches strongly supports the validity of this work.

5.5.3.1 Experimental details and results

The sample used for the experiment, highly diluted Alexa Fluor 488 dyes dispersed in a thin film of PMMA, is prepared by spin coating the starting solution on a microscope coverslip. The sample preparation follows the same procedure described in the first part of the Chapter. In focus images are collected with 0.5 s integration time while the defocused images with 1.5 s integration time to compensate the lower signal-to-noise ratio. First the sample is imaged while positioned at the focus of the objective lens, and then the objective is displaced of about 1 µm towards the sample. The displacement cannot be estimate with high accuracy because the piezo stage used to move the objective lacks of a feedback system.

It has been necessary also to introduce few seconds delay between the displacement of the objective and the recording of the images to allow relaxation of the oil drop used with the objective. Images without delay time have shown erroneous positioning in the z direction together with translational motion of the sample. It is crucial to image the same dipole in the same position (for recognition) and at the proper focal distance (in focus and ~ 1 µm defocused). To prevent photobleaching of the emitters, the laser excitation light is stopped by a shutter at the end of the in focus integration time and re-opened with 10 ms delayed in respect to the defocus integration initial time. The 488 nm line of the Argon ion laser was tuned to be circularly polarized by the use of a λ/4 waveplate.

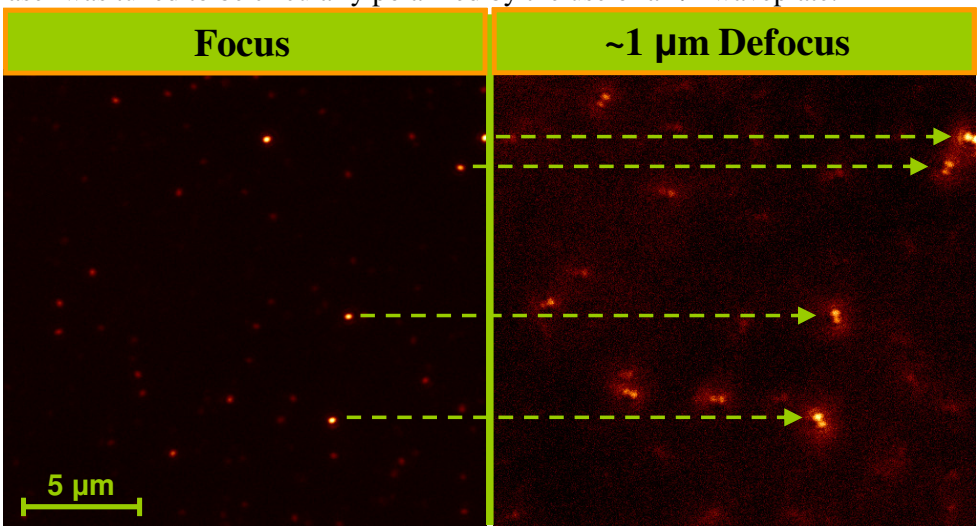

Figure 5.22: Survey images of the sample obtained in focus (left) and ~ 1 µm defocused. Several emitters are recognizable in both images. Some of the emitters present in the focus image are missing from the defocus images because of photobleaching.

Figure 5.22 illustrates a survey of the sample where a 21 x 21 μm^2 area is imaged both in focus and ~ 1µm defocused with the wide field fluorescent microscope. Several emitters are recognizable in both images; some in the left image (focus) are not visible on the right because of photobleaching events occurred. The defocused patterns, in particular, seem to correspond to dipole mainly parallel to the surface as result of the illumination adopted as mentioned earlier[23]. By analyzing the diffraction limited spots (PSF) and the corresponding defocused patterns is possible to correlate the measured angles of each emitter.

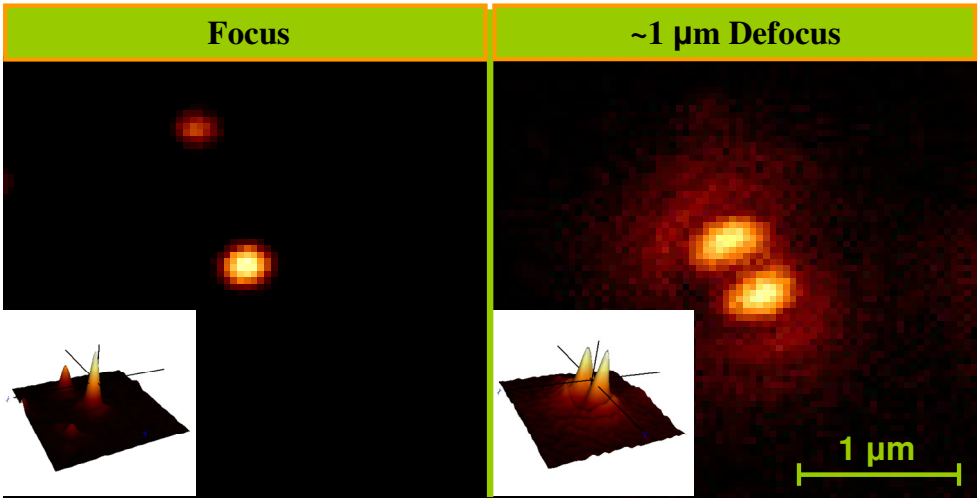

Figure 5.23: Detailed images of a single dipole imaged in focus (left) and at ~ 1 µm defocused position. The insets show the spatial distribution of the fluorescence intensity of the two patterns. From the defocus image it is possible to roughly estimate the dipole to lie at ~ 45° with the x-axis and parallel to the surface.

Figure 5.23 shows the two images (focus on the left and defocused on the right) of the same emitting dipole. In the corresponding insights the 3-D distributions of photons are represented. From the defocus image is also possible to appreciate the different pattern of the fluorescence which is spread over a wider area. The imaged dipole is adsorbed parallel to the glass surface at about 45° respect the x-axis.

The orientation of dipoles imaged out of focus has been calculated by the use of two 2-dimensional Gaussian functions to mimic the symmetry of the defocused pattern around the dipole axis. The 2-dimensional Gaussian function introduced earlier has been used to calculate the angle of the in focus images. The orientation of more than 80 dipoles has been calculated and the correlation of the focus-defocus values is presented in Figure 5.24.

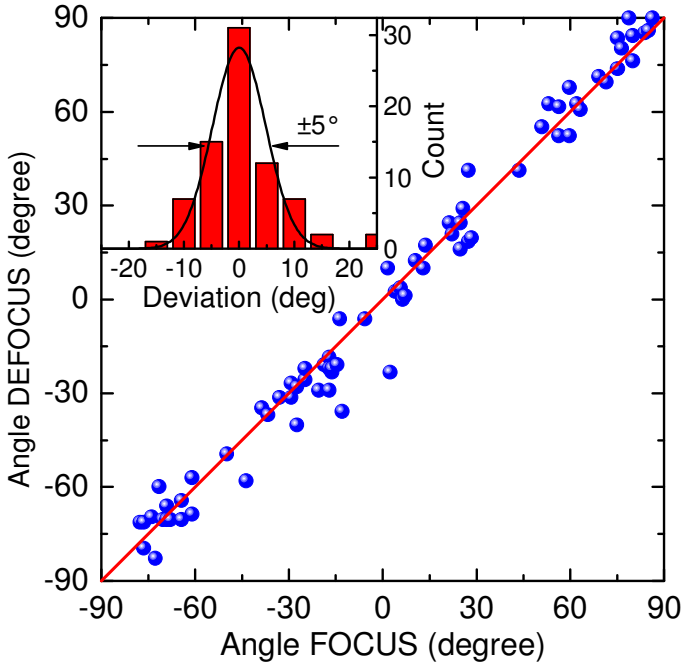

Figure 5.24: Correlation curve Focus-Defocus angle values. The angle with respect the x-axis is measured and the values reported between 0° and 180°. The orange dash line resembles an ideal correspondence. The correlation focus-defocus lies close to the ideal case and the estimated accuracy of the angle measurement is about 10°.

The blue points represent the measured value of the angles of the analyzed dipoles with the x-axis. The x coordinate represents the focus value, while the y coordinate the defocus one. The orange dash line resembles the perfect correspondence of values. The obtained correlation of values follows rather precisely the ideal condition thus supporting the consistency of the method proposed here. The estimated deviation holds about 5° accuracy in the measurement of the in-plane angle.

The substantial convergence of the value of the angles describing the in-plane orientation of single molecular dipoles measured either in focus or in defocus images proves the validity of the new approach proposed here. Besides, it is also shown the obtained nm accuracy in the determination of the position of the emitting dipoles. At the knowledge of the author, the approach proposed here alone can provide with a single image super resolution accuracy and orientation characterization of the imaged fluorescent dipoles. Additionally, the accuracy of the measured quantities (~2 nm for accuracy position and ~5° accuracy for the in-plane orientation) and the time dynamics 0.5s (single frame integration time) are comparable to the values found in literature. Here, they represent the starting point eventually leading to much further substantial improvements.

5.5.4 Application: dipoles orientation in an anisotropic environment

To prove the validity of the method proposed, the latter is applied to investigate the orientation of single emitters while imaged in an environment presenting strong spatial anisotropic features. So far, the analysis of the PSFs of single emitting fluorescent dipoles exploiting the theoretical model introduced by Richards and Wolf[39] has been applied only to samples where the dipoles feature random orientation following the sample's preparation protocol. The new method has proven its validity in following the random orientation of dipoles as well as compared to the defocusing technique. Here, the idea is to introduce in the sample a spatially anisotropic structure and, by labeling it with fluorescent dipoles, possibly to recognize its anisotropy by measuring the orientation of dipoles.

The anisotropic structure is created on the glass surface by highly oriented chains of polytetrafluoroethylene (PTFE) with length of several micrometers adsorbed onto the glass surface of the coverslip by frictional force. The surface is then spin coated with a solution containing highly diluted Alexa Fluor 488 and PMMA. Therefore, the sample consists of a similar thin polymeric film with embedded fluorescent dipoles, as in the previous examples, but the glass surface presents highly anisotropic structures which might promote the alignment of the fluorescent dipoles along the PTFE "backbone".

It has been observed and demonstrated that PTFE, thanks to its low surface energy, by sliding it on a glass surface experiences transfer of matter to the surface because of frictional force exerted between the two materials[40, 41]. Tabor and coworkers[40, 41], in their study focused on the kinetic and static friction coefficient of PTFE when sliding on smooth surfaces such as glass, have reported the transfer of PTFE chains onto the glass in form of lumps, ribbons and sheets. The highly aligned conjugated molecules have been also investigated in optical or microelectronic devices because of the properties derived from their "backbone" preferentially oriented along the substrate surface[42]. It has been also observed that pre-oriented layers of PTFE have favored the oriented growth of wide range of materials including polymers and liquid crystals[43].

In this work, the interest focuses on the orientation of backbones along the sliding direction of PTFE on the glass surface of coverslips to achieve highly oriented structures able to drive the partially ordered growth of the polymer film in which single fluorescent dipoles are embedded. The alignment of polymer chains of PMMA along the backbone of PTFE might exert the driving force for the subsequent alignment of fluorescent dipoles.

5.5.4.1 Sample preparation and results

The sample used has first required the sliding of a rod of PTFE on the surface of a microscope coverslip at room temperature, followed by the spin coating of the

solution containing PMMA and Alexa Fluor 488 fluorescent dipoles. The obtained surface was then imaged in the wide field fluorescent microscope.

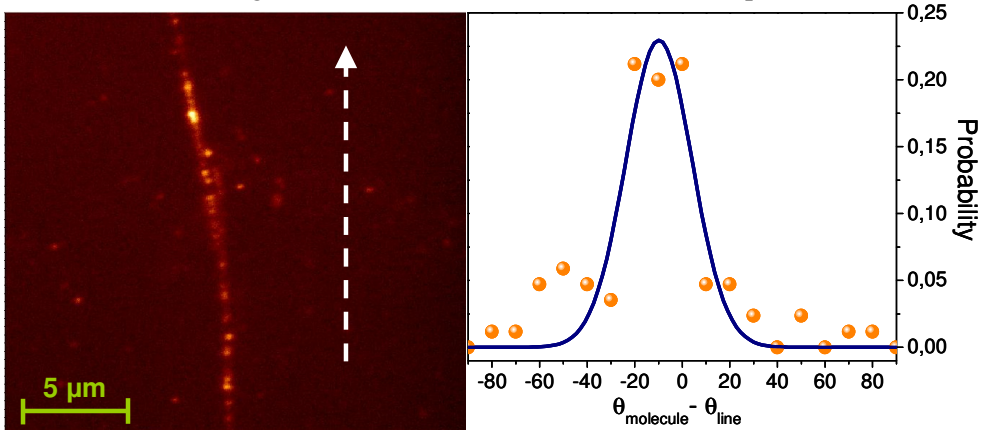

Figure 5.25: Wide Field Fluorescent Microscope image of the sample. A highly oriented structure (several µm length), following the direction of the sliding process, is labeled with fluorescent single dipoles. The graph on the right illustrates the distribution of angles measured from the single molecules labeling the oriented PTFE backbone. More than 60% of the analyzed molecules posses an in-plane orientation which follows the PTFE structure with a deviation of ±10°.

Figure 5.25 illustrates, on the right, a typical structure observed on the sample's surface with the wide field fluorescent microscope. A chain-like structure (several µm long), oriented along the sliding direction (white arrow), is labeled with various fluorescent single molecules. An analogue analysis as presented in Figure 5.7 has revealed the analyzed emitters to consist of single dipoles. Fluorescent images of the surface, illuminated with circular polarized light from the Argon ion laser, are obtained at 2 Hz frame rate in the focal position of the objective. The PSFs of the fluorescent molecules embedded in the PMMA film are then analyzed in order to extract the value of the orientation angles.

The graph in Figure 5.25 presents the distribution of the measured angles of the analyzed molecules. On the x-coordinate is represented the difference (between 0° and 180°) between the estimated angle of the PTFE linear structure and the angles of the molecules labeling the structure. More than 60% of the analyzed dipoles lie with an in-plane angle that follows the structure orientation with a deviation of about 10°. This value is considered to be representative of the real angle distribution being the experimental accuracy around 5° (see Figure 5.24). The presence of PTFE linear and oriented structures on the glass surface substantially affects the orientation of fluorescent dipoles in the PMMA matrix otherwise randomly oriented. The results achieved here at single molecule level support what predicted by previous works[42, 43]; the highly pre-oriented structure favors the alignment of the polymer molecules resulting in the hindered orientation of the embedded fluorescent molecules.

5.6 Conclusions

The analysis devoted to the experimental characterization of the point spread function has revealed the agreement with the theoretical model of Richards and Wolf[4]. If a single dipole is imaged while emitting polarized light (fixed orientation within the image integration time) and the collection of the emitted photons is achieved with a high numerical aperture lens (objective), the PSF develops anisotropic geometry (ellipse). This conformational change can affect the correct evaluation of features such as the super-resolution accuracy.

It has been shown that the ellipticity of the PSF consequentially causes the value of the localization accuracy to vary at different directions. If the long axis of the ellipse is 20% longer than the short one, the accuracy along the direction of the long axis will result 20% lower.

The elongation of the PSF along the axis corresponding to the direction of the dipole could be used to extract information not only concerning the position of the dipole, but also its orientation. It is possible to introduce in the 2-dimensional Gaussian function, used to model the PSF, a term concerning the orientation of the ellipse. The parameter alfa (α) represents the angle the long axis of the ellipse forms with the X-axis of the image. Figure 5.26 shows the real image of a single emitting dipole, the fit obtained by 2-dimensional Gaussian with $\alpha = 90°$, and the fit obtained by leaving the parameter α free. In the fit obtained with fixed value of α, the possible information obtainable concerns solely the position accuracy. By fitting the same PSF with Gaussian function having free value for the parameter α, it is possible to estimate the orientation of the dipole as shown in Figure 5.26.

Dual to the position accuracy study, is the investigation concerning the possibility to achieve orientation information of the dipoles imaged with the wide field fluorescent microscope. The approach proposed often in literature to yield orientation characterization of single molecules by the exploitation of the defocus imaging technique[24, 26] that weakens the position accuracy achievable because of the intrinsic lower signal-to-noise ratio resulting from the defocusing.

The proposed exploitation of Richards and Wolf theoretical model of the PSF has proven its sensitivity concerning the position accuracy and is applied also to reveal the orientation of the imaged dipoles. The elliptical shape of the PSFs imaged under the conditions required by the theoretical model, following the elongation of the PSF along the emitting dipole axis, can be used to characterize not only the position of the dipole with accuracy beyond the Abbe's limit, but also the 2-dimensional orientation.

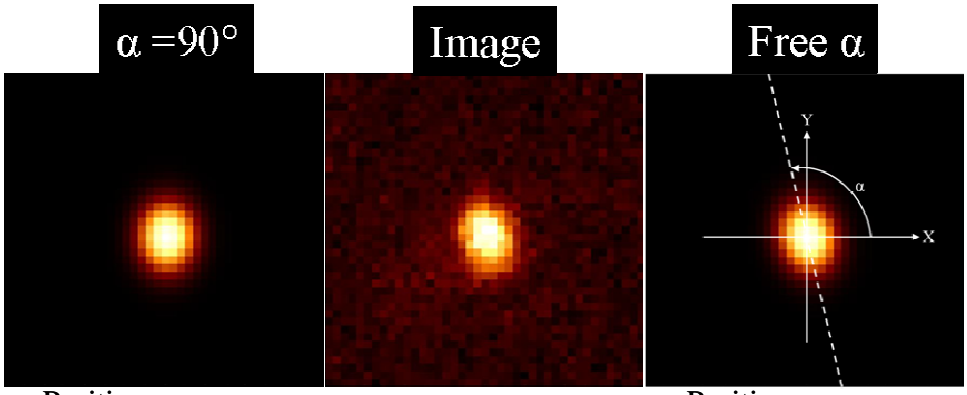

Figure 5.26: Image of PSF of a single dipole and of fits obtained by 2-dimensional Gaussian. The image to the left represents the fit when the angle α is kept constant at 90°. Image on the right is obtained by letting the value of α free. By modeling the PSF according the orientation of the dipole, it is possible to measure the orientation of the dipole itself.

Direct comparison between the new approach and the more traditional defocus imaging has proven the consistency of the novel method. Single dipoles have been imaged first in focus and afterwards in a position ~1 μm away as usually done in the defocusing approach. The analysis of the so obtained images and the subsequent analysis have provided the possibility to correlate the values of the focus images with the defocus ones with a deviation of about 5°. Additionally, the combination of the idea presented in Chapter 4, meant to exploit features of photobleaching events to achieve quantitative analysis, and the one presented in here can produce surprising information. Here follows an example to support what just mentioned. Images and analysis of what at first seems to be a single molecule embedded in PMMA matrix are presented.

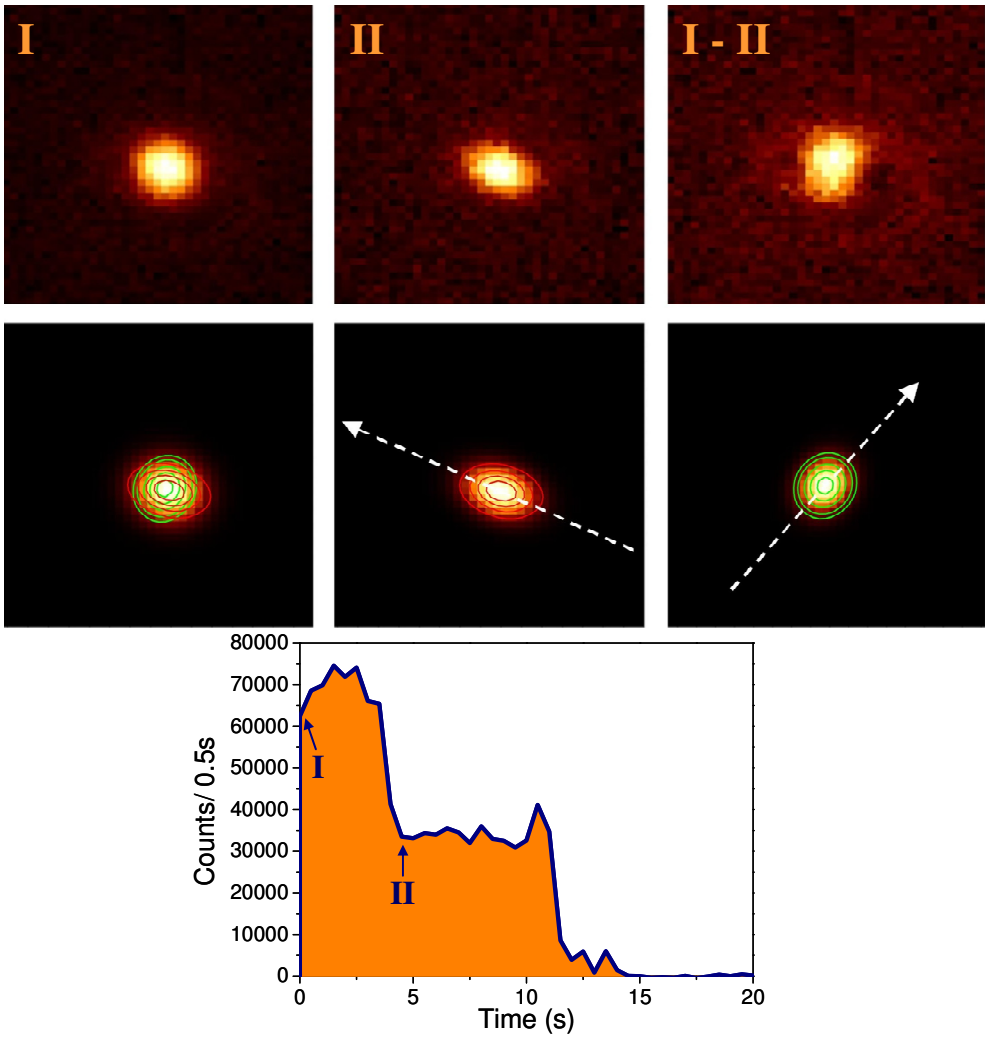

Figure 27: Image I shows a diffraction limited spot presenting a circular symmetry (ratio long short axis ~1). The diagram on the bottom resembles the time dependence of the intensity of the imaged spot. The time transient shows two step like events before complete photobleaching, thus suggesting the spot to consist of two single molecules (see chapter 4). Image II is obtained after the first photobleaching event. The only molecules still emitting shows elliptical PSF (ratio long/short axes ~ 1.25). Image I-II corresponds to a reconstructed image of the second molecule and it has been obtained by subtracting image II from image I. The analysis performed on images II and I-II reveals the spot imaged in I consisting of two single molecules 30 nm apart, and oriented 150° and 42° as shown in the three images on the bottom.

Figure 27 shows real images of a diffraction limited spot. The image illustrates a bright spot (I) which possesses circular symmetry. Below is also introduced the time dependence of the fluorescence intensity from the spot. The graph presents two step-like events typical for single molecule photobleaching events (details about photobleaching are presented in chapter 4). From this, it is possible to conclude that the imaged spot consists actually of two single molecules whose distance is too small to be optically resolved.

After the first photobleaching event, a single molecule is visible (II). It clearly presents elliptical PSF enabling not only to accurately measure its position, but also its orientation (~ 150° respect the X-axis) in the imaged plane. By subtracting image II from the starting image of the spot (I), the image of the second molecule can be recovered (I-II), as shown in the work of Selvin et. al.[44] (though limited to the molecules' position). The analysis of the reconstructed image of the second molecule allows to estimate the dipole to be oriented at ~ 42°. The two molecules are at a distance of ~ 30 nm apart.

The example presented shows a much more detailed investigation and understanding of what classically could be considered irresolvable. If the starting image resembles a circular diffraction limited spot (no information about its orientation and number of emitters), the idea proposed in this chapter (together with the knowledge from Chapter 4) instead shows the spot to consist of two single emitters 30 nm apart and oriented respectively at 150° and 42° respect the X-axis.

Furthermore, the proposed method has been applied to unravel the orientation of pre-oriented PTFE structures. The analysis of Alexa Fluor 488 molecules embedded in the PMMA matrix has highlighted the possible preferential oriented organization of the polymer structure along the PTFE linear "backbone".

In conclusion, the work presented in this chapter proposes the first imaging method to achieve both position and orientation characterization at the single molecule level of the investigated specimen by the use of a single in-focus image, therefore further improving, at the judgment of the author, the potential of the single molecule fluorescent microscopy technique. A more complex method based on defocus images has been proposed by Aguet et al[45]. Their approach relies on the representation of the emitted pattern by 3-D steerable filters providing an accuracy of 5 nm for position and 2 degrees for orientation. In a very recent work by the group of Stefan Hell[46], it is again discussed to influence of molecular orientation on the localization accuracy especially in relation to the imaging of the emitting dipole from a defocal position.

The required polarized light source limits the observable dynamics (rotation) to the frame rate. The dipole orientation can vary in time, but it should be imaged at a frame rate such to hold polarized emission. The integration time used in the experiments presented in this chapter (0.5 second) may prevent the application to systems with faster dynamics; nevertheless, the frame rate can be optimized to higher values.

All the obtainable informations are based on the value of the signal-to-nose ratio. Optimization of the sample preparation (to reduce the background signal), the use of electron-multiplied CCD cameras (EMCCD), and different excitation light polarization (circular) might enhance the applicability of the approach described here.

Bibliography

1. Born, M.; Wolf, E., *Principles of Optics*. 7 ed.; Cambridge, 1999.
2. Airy, G. B. *Trans. Cambr. Philos. Soc.* **1835,** 5, 283-291.
3. Hopkins, H. *Proc. Phys. Soc.* **1943,** 55, (2).
4. B. Richards E. Wolf. *Proc. R. Soc. London* **1959,** 253, (1274), 358-379.
5. K. Wondraczek, J. A., J. Fuhrmann. *Macromol. Chem. Phys.* **2004,** 205, 1858-1862.
6. C. M. Anderson, G. N. G., I. E. Morrison, G. V. Stevenson, R. J. Cherry. *J. Cell. Sci.* **1992,** 101, 415-425.
7. G. J. Schulz, H. S., T. Schmidt. *Biophys. J.* **1997,** 77, 3371-3383.
8. M. K. Cheezum, W. F. W., W. H. Guilford. *Biophys. J.* **2001,** 81, 2378-2388.
9. J.James, *Light Microscopic Techniques in Biology and Medicine*. Amsterdam, 1976; p 75 - 82.
10. A. Yildiz, J. N. F., S. A. McKinney, T. Ha, Y. E. Goldman, P. R. Selvin. *Science* **2003,** 300, 2061-2065.
11. D. Wu, Z. L., C. Sun, X. Zhang. *Nan. Lett.* **2008,** 8, (4).
12. A. Sharonov, R. M. H. *Proc. Nat. Am. Soc.* **2006,** 103, (50).
13. C. Eggeling, e. a. *Nature* **2009,** 457.
14. C. Flores, e. a. *J. Am. Chem. Soc.* **2007,** 129, 13970-13977.
15. E. Betzig, e. a. *Science* **2006,** 313, 1642-1645.
16. Bobroff, N. *Rev. Sci. Instrum.* **1986,** 57, 1152-1157.
17. R. E. Thompson, D. R. L., W. W. Webb. *Biophys. J.* **2002,** 82, 2775 - 2783.
18. Skinner J. L.; Moerner W. E. *J. Phys. Chem.* **1996,** 100, 13251.
19. Trautman J. K.; Betzig E.; et al. *Nature* **1994,** 369, 40 -42.
20. Skinner J. L.; Basche' T.; Moerner W. E.; Orrit M.; Wild U. P., *In Single Molecule Optical Detection, Imaging, and Spectroscopy*. Verlag-Chemie: Munich, 1997.
21. Hofkens J.; De Schryver F. C.; et al. *Macromolecules* **1998,** 31, 4493 - 4497.
22. Bartko A. P.; Dickson R. M. *J. Phys. Chem. B* **1999,** 103, (16), 3053 - 3056.
23. Bohmer M.; Enderlein J. *J. Opt. Soc. Am. B* **2003,** 20, (3), 554 - 559.
24. Uji-i H.; Hofkens J; et al. *Polymer* **2006,** 47, 2511 - 2518.
25. Thompson R. E.; Larson D. R.; Webb W. W. *Biophys. J.* **2002,** 82, 2775 - 2783.

26. Toprak E.; Selvin P. R.; et al. *Proc. Natl. Acad. Sci. USA* **2006,** 103, (17), 6495 - 6499.
27. Schroeyers W.; De Schryver F. C.; et al. *J. Am. Chem. Soc.* **2004,** 126, 14310 - 14311.
28. Tietz C; Wrachtrup J.; et al. *Biophys. J.* **2001,** 81, 556 - 562.
29. Deschenes L. A.; Van den Bout D. A. *Science* **2001,** 292, 255 - 258.
30. Trabesinger W.; Weder C.; et al. *J. Phys. Chem. B* **2000,** 104, 5221 - 5224.
31. Ishijima A.; Yanagida T.; et al. *Biophys. J.* **1996,** 70, 383 - 400.
32. Kinosita K. Jr. *FASEB J.* **1999,** 13, 201 - 208.
33. Kinosita K. Jr.; Yoshida M.; et al. *Cell* **1998,** 93, 21 - 24.
34. Warshaw D. M.; Berger C.; et al. *Proc. Natl. Acad. Sci. USA* **1998,** 95, 8034 - 8039.
35. Macklin J. J.; Brus L. E.; et al. *Science* **1996,** 272, 255 - 258.
36. Ha T.; Weiss S.; et al. *Phys. Rev. Lett.* **1996,** 77, 3979 - 3982.
37. Farrer R. A.; So P. T. C.; et al. *Opt. Lett.* **1999,** 24, 1832 - 1834.
38. Jasny J.; Sepiol J. *Chem. Phys. Lett.* **1997,** 273, 439 - 443.
39. Richards B.; Wolf E. *Proc. Roy. Soc. Lon.* **1959,** 253, (1274), 358 - 379.
40. Makinson K.; Tabor D. *Proc. Roy. Soc. Lond. A* **1964,** 281, 49.
41. Pooley C.; Tabor D. *Proc. Roy. Soc. Lond. A* **1972,** 329, 251.
42. Gill R. E. Design, synthesis and characterization of luminescent organic semiconductors. Phd Thesis, Rijksunivesiteit Groningen, Groningen, 1996.
43. Wittman J. C.; Smith P. *Nature* **1991,** 352, 414 - 417.
44. Gordon M.P.; Ha T.; R., S. P. *Proc. Natl. Acad. Sci. USA* **2004,** 101, (17), 6462 - 6465.
45. Aguet F.; Unser M.; et. al. *Opt. Expr.* **2009,** 17, (8), 6829 - 6848.
46. Engelhardt J.; Hell S.W.; et. al. *Nano Lett.* **2011,** 11, 209 - 213.

Appendix 1 (Albert Einstein, 1905)

Diffusion coefficient

It is considered the state of dynamic equilibrium of a batch of particles suspended in a liquid on the assumption that a force K, only depending on the position and not on time, acts on the particles. To simplify the calculations, K is assumed to be exerted only in the x-axis. v is assumed to be the number of suspended particles per unit volume. In the condition of dynamic equilibrium v is such function of x that the variation of free energy vanishes for an arbitrary virtual displacement δx of the suspended particle.

$$\delta F = \delta E - T\delta S = 0$$

with:
F = Free energy,
E = Energy of the system,
T = Absolute temperature,
S = Entropy

The liquid is assumed to have unit area of cross-section perpendicular to the x-axis and bounded by the planes x = 0 and x = ℓ.

Then,

$$\delta E = -\int_0^{\ell} K v \delta x dx$$

and

$$\delta S = -\int_0^{\ell} R \frac{\nu}{N} \frac{\partial \delta x}{\partial x} dx = -\frac{R}{N} \int_0^{\ell} \frac{\partial \nu}{\partial x} \delta x dx$$

The required condition of equilibrium is:

$$-K\nu + \frac{RT}{N} \frac{\partial \nu}{\partial x} = 0 \qquad \text{Eq. I}$$

with N as the actual number of molecules contained in a mole.

Equation I could be used to find the coefficient of diffusion of the suspended particle.

The condition of dynamic equilibrium is considered as superposition of two processes:

1) A movement of the suspended substance under the influence of the force K acting on each single suspended particle.
2) A process of diffusion, which is to be looked upon as result of the irregular movement of the particles produced by thermal molecular movement.

If suspended particles are assumed to have spherical form (radius = R), and the liquid to have a coefficient of viscosity η, then the force K imparts to the single particle a velocity (Kirchoff' law) $= \frac{K}{6\pi\eta R}$, and there will pass a unit area per unit time $\frac{\nu K}{6\pi\eta R}$ particles.

If D signifies the coefficient of diffusion of the suspended substance, and μ the mass of a particle, as result of diffusion there will pass across unit area in a unit time $-D\frac{\partial \nu}{\partial x}$ particles.

In dynamic equilibrium is: $$\frac{\nu K}{6\pi\eta R} - D\frac{\partial \nu}{\partial x} = 0 \qquad \text{Eq. II}$$

It is possible to calculate the coefficient of diffusion from the two conditions (I and II) found for the dynamic equilibrium:

$$D = \frac{RT}{N}\frac{1}{6\pi\eta R} = \frac{K_B T}{6\pi\eta R}$$

The coefficient of diffusion of the suspended substance, therefore, depends only (except for universal constant and absolute temperature) on the coefficient of viscosity of the liquid and on the size of the suspended particles.

From Einstein's publication[1]:*"This result represents an exact value of a process which has to deal with probability as I will show in the next section".*

On the irregular movement of particles and the relation of this with diffusion

There are two major points in Einstein's solution of the problem of Brownian motion:

1) The motion is caused by the exceedingly frequent impacts on particles of the incessantly moving molecules of liquid in which they are suspended.
2) The motion of these molecules is so complicated that its effect on the particle can only be described probabilistically in term of exceedingly frequent statistically independent impacts.

The motion of each individual particle has to be assumed independent form the movements of all other particles; the movements of one and same particle at different time intervals have to be considered as mutually independent processes (Ergodic principle), as long as the time intervals are not taken too small.

Let us introduce the time interval τ, very small to the observation time interval, but of such magnitude that the movements executed by a particle in two consecutive time intervals τ are to be considered as mutually independent.

Suppose to have n suspended particles in a liquid. In a time interval τ, the x coordinate of a single particle will increase by Δ, with Δ different (positive or negative) for each particle. To each value of Δ a certain probability-law will hold.

Assume that *dn* is the number of particles that experience in τ a displacement between Δ and $\Delta + d\Delta$:

$$dn = n\phi(\Delta)d\Delta$$

where

$$\int_{-\infty}^{+\infty} \phi(\Delta)d\Delta = 1$$

and ϕ only differs from zero for very small values of Δ and fulfils the condition

$$\phi(\Delta) = \phi(-\Delta)$$

The idea here is to resolve the dependence of D on the probability function ϕ; still holds the assumption that the number of particles per unit volume (υ) is dependent on x and t.

By writing the number of particles like $\upsilon = f(x,t)$, it will be calculated the distribution of particles at time $t + \tau$ from the distribution at time t.

It is found:

$$f(x,t+\tau)dx = dx\int_{-\infty}^{+\infty} f(x+\Delta)\phi(\Delta)d\Delta \qquad \text{Eq. III}$$

Eq. III is called *Chapman-Kolmogorov equation* and describes the probability for a particle to be in the position x at time $t + \tau$ is equal to the sum of the probabilities of all possible displacements Δ from position $x + \Delta$, multiplied for the probability of being in position $x + \Delta$ at time t.

Eq. III is crucial because is based on the independence of the displacement Δ of any previous history of the motion. To estimate the position of a particle at a time t', or better to calculate the probability of the position of the particle at time t', it is only necessary to know the position at the initial time t.

The aforementioned postulate is known as *Markov postulate* base (central dynamic equation) of all Markov processes.

Being τ very small, it is possible to write: $f(x,t+\tau) = f(x,t) + \tau\dfrac{\partial f}{\partial t}$

Further, $f(x + \Delta, t)$ is expanded in powers of Δ:

$$f(x+\Delta,t) = f(x,t) + \Delta\frac{\partial f(x,t)}{\partial x} + \frac{\Delta^2}{2!}\frac{\partial^2 f(x,t)}{\partial x^2} \qquad \text{Eq. IV}$$

From eq. III and IV:

$$f(x,t) + \tau\frac{\partial f(x,t)}{\partial t} =$$

$$f(x,t)\int_{-\infty}^{+\infty}\phi(\Delta)d\Delta + \frac{\partial f(x,t)}{\partial x}\int_{-\infty}^{+\infty}\Delta\phi(\Delta)d\Delta + \frac{\partial^2 f(x,t)}{\partial x^2}\int_{-\infty}^{+\infty}\frac{\Delta^2}{2!}\phi(\Delta)d\Delta \qquad \text{Eq. V}$$

Eq. V is as well known as *Kramers-Moyal expansion.*

The second, fourth etc. terms of eq. V vanish (ϕ is an even function), while the first, third etc. terms each is very small compared with the previous.

Because of the property of ϕ ($\int_{-\infty}^{+\infty}\phi(\Delta)d\Delta = 1$), eq V can be written as:

$$\frac{\partial f(x,t)}{\partial t} = \frac{1}{\tau}\frac{\partial^2 f(x,t)}{\partial x^2}\int_{-\infty}^{+\infty}\frac{\Delta^2}{2!}\phi(\Delta)d\Delta$$

by defining: $D = \frac{1}{\tau}\int_{-\infty}^{+\infty}\frac{\Delta^2}{2!}\phi(\Delta)d\Delta$

it is found:

$$\frac{\partial f(x,t)}{\partial t} = D\frac{\partial^2 f(x,t)}{\partial x^2} \qquad \text{Eq. VI}$$

This equation is well known as the differential equation for diffusion. It can be solved with the method of integral transform, which uses space Fourier transform of f(x,t) and its inverse.

Let us define:

$$F(k,t) = \int_{-\infty}^{+\infty} f(x,t)e^{-ikx}dx \qquad \text{and} \qquad f(x,t) = \frac{1}{2\pi}\int_{-\infty}^{+\infty} F(k,t)e^{ikx}dx$$

it is:

$$\frac{\partial f(x,t)}{\partial t} = \int_{-\infty}^{+\infty}\frac{\partial F}{\partial t}e^{ikx}dk$$

and

$$\frac{\partial^2 f}{\partial x^2} = \int_{-\infty}^{+\infty} F(k,t)\frac{\partial^2 e^{ikx}}{\partial x^2}dk = \int_{-\infty}^{+\infty} F(k,t)\left(-k^2\right)e^{ikx}dk$$

Remembering that $\frac{\partial f}{\partial t} = D\frac{\partial^2 f}{\partial x^2}$ (Eq. VI), it is then found:

$$\int_{-\infty}^{+\infty}\frac{\partial F}{\partial t}e^{ikx}dk = -k^2 D\int_{-\infty}^{+\infty}F(k,t)e^{ikx}dk$$

and the solution is:

$$\frac{\partial F}{\partial t} = -k^2 DF$$

Solution of the differential equation is:

$$F(k,t) = F(k,0)e^{-k^2 Dt}$$

and from the initial condition: $f(x,t=0)=\delta(x)\rightarrow F(k,0)=1$

It is now possible to calculate f(x,t):

$$f(x,t) = \frac{1}{2\pi}\int_{-\infty}^{+\infty}e^{-\left(k^2 Dt - ikx\right)}dk$$

$$= \frac{1}{2\pi}\int_{-\infty}^{+\infty}e^{-Dt\left(k^2 - i\frac{kx}{Dt}\right)}dk$$

One can write

$$e^{-Dt\left(k^2 - i\frac{kx}{Dt}\right)} = e^{-\frac{x^2}{4Dt}}e^{-Dt\left(k-i\frac{x}{2Dt}\right)^2}$$

and obtain

$$f(x,t) = \frac{1}{2\pi}e^{-\frac{x^2}{4Dt}}\int_{-\infty}^{+\infty}e^{-Dt\left(k-i\frac{x}{2Dt}\right)^2}dk = \frac{1}{2\pi}e^{-\frac{x^2}{4Dt}}\sqrt{\frac{\pi}{Dt}} = \frac{e^{-\frac{x^2}{4Dt}}}{\sqrt{4\pi Dt}}$$

The function f(x,t) expresses the probability to find a particle in position x at time t, and therefore to estimate the probable distribution of displacement at any time t' > t. It is significant to notice how the constants in the exponent are related to the coefficient of diffusion. It enables to calculate the displacement Δ_x in the x-direction which a particle experiences on an average or, more accurately expressed, the square root of the arithmetic mean of squares of displacements in the direction of the x-axis:

$$\Delta_x = \sqrt{\langle x^2\rangle} = \sqrt{2Dt}$$

The mean square of displacement is thus linearly proportional with time.

1. Einstein A. *Ann. Phys.* **1905,** 17, 549-560.

Appendix 2

To further verify the experimental procedure, two control measurements have been performed. The main point under discussion here concerns the value of the photobleaching steps and whether the mean value has been measured with adequate accuracy.

Two are the factor that here are discussed and that surely might influence the amplitude of bleaching steps. The first deals with the occurrence of a "double" step, in which two dye molecules photobleach at the same time. The seconds concerns the excitation profile.

As mentioned before, double bleaching events might occur: first because it is a stochastic process, and second because the bleaching rate depends on the power density of the excitation light. The experimental conditions might result not ideally for this kind of experiment and accuracy.

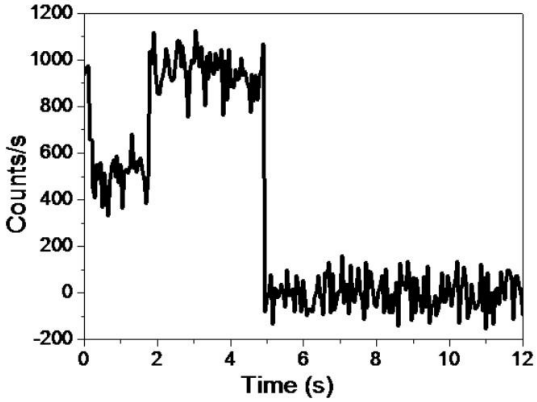

Figure 1: Time dependence of the emission intensity from a spot. The trace shows a two step photobleaching event where two emitters bleach at the same time. The amplitude of this double step is twice the mean value of measure mean value for a single step.

Figure 1 presents the time dependence of the intensity of an imaged spot. The trace clearly shows the spot consisting of two fluorescent molecules and that the final bleaching step consists of the simultaneously bleaching of both the dyes. Though not common in the time traces measured, still "double" steps are present as reported by Figure 1. The amplitude of the final step in the figure is about two times bigger than the mean value evaluated and presented by the distribution of

Figure 4.7. Still steps of such amplitude occur with poor rate (see inset of Figure 4.7); ~2% of the total amount of the analyzed steps present this amplitude.

Second point of discussion is about the excitation profile. The emission intensity of a molecule is strictly dependent on the excitation intensity. To higher excitation intensity correspond higher fluorescent emission. Therefore the amplitude of a photobleaching step might depend also on the excitation intensity illuminating the fluorescent molecule. The laser emission of the laser source used here is assumed to be very stable, thus the only parameter to affect the excitation intensity is the excitation profile on the sample.

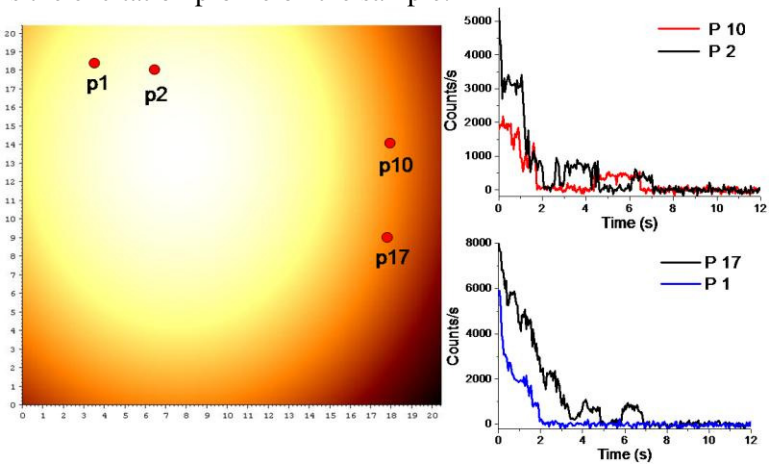

Figure 2: Typical Gaussian profile of the excitation laser light intensity on the sample and positions of four different dyes imaged. The graphs on the right shows the time dependence of the emission intensity corresponding to the spots which position is marked in the figure. Even if molecules are positioned differently with respect the laser profile, the amplitude of single photobleaching steps from all four the time traces result comparable.

The image presented in Figure 2 shows the laser excitation Gaussian profile on the sample at the time of the experiment and the position of four different bright spots. The different colors of the profile indicate difference in the intensity of the excitation. The time traces of the four spots, which positions are marked with respect the profile, are presented on the right. The fluorescent signals have been normalized according to the background (excitation) intensity in order to have zero signal when the emitters are completely photobleached.

Each time trace shows the amplitude of the last photobleaching step to be comparable. Even if the four fluorescent spots are illuminated by light with different intensity, still this difference is too small to generate a substantial variation in the emission of a single molecule represented by the final steps. From this it is possible to assume approximately that a rather homogeneous illumination of the sample has been accomplished, even though a quantitative characterization of the excitation profile is required for the next series of experiments.

Summary

Optical microscopy is among the oldest techniques developed and implemented for modern science; the first microscope dating back to the end of the sixteenth century. Throughout 5 centuries, scientists have greatly benefitted from the remarkable possibilities offered by the observation of nature at small scales in a number of disciplines ranging from biology to medicine and from condensed matter physics to optics. The first observation of the complex structure of biological systems and of its fundamental constituent, the cell, together with the very first experiments concerning the corpuscular nature of matter, i.e. the observation of Brownian motion, are surely among the most remarkable results unfolded by the use of optical microscopes. The quest to increase sensitivity and resolution towards smaller and smaller scales, provoked by the demand to gain a much more detailed understanding of the microscopic world, has over the years led to a boost of the capabilities of microscopic techniques, which is continuing even today.

Five centuries of theoretical understanding and technological improvements have provided modern scientist the possibility to study matter at the single molecule level. The single molecule and single particle microscopy techniques developed in the last 20 years and subject of this dissertation, has extended the applications of optical microscopies to new fields such as nanotechnology and material science. Modern single molecule microscopy has provided, and still does, scientists with a powerful tool in the quest of investigating matter at the smallest length scales. How to achieve single molecule sensitivity, how the light behaves when emitted by a single molecule, and how the imaging process occurs are largely discussed in this dissertation together with a number of examples where the technique is applied to the investigation of diverse systems and conditions.

Chapter 2 is mainly devoted to the introduction of fluorescence microscopy and to a technical description of the set up and its parts (excitation source, optical elements, detector etc.). Also, it is used to introduce and characterize the software analysis of the collected images required to obtain a meaningful interpretation of the results.

Chapter 3 and chapter 4 deal with specific issues concerning respectively nanotechnology and biology. Chapter 3 introduces and discusses the concept of self-propulsion in micro- (10^{-6} m) and nano-structures (10^{-9} m), a subject which the interest of several research groups driven by the wish to control matter and matter transport at the nanoscale. Even though already studied and achieved in micro-

sized objects, the propulsion in a liquid environment promoted by catalytic reactions is strongly challenged, if not prevented, at the nano-scale due to the massive influence that the Brownian force exerts on the objects. By the use of a single particle tracking approach, it is possible to follow the motion of diffusive nano-particles on which the chemical reactions occur and thus unravel deviations from the pure Brownian motion caused by the catalytic activity. Results have shown the motion of particles to strictly obey the Brownian diffusion law. It is speculated that the homogeneous release of the reaction products (oxygen and water molecules), either due to the geometry or the functionalization of the nano-objects, prevents the generation of a net driving force.

Chapter 4 addresses a debated issue concerning the so-called SecYEG protein conducting channel. In any living cell the secretion and insertion of protein outside or into the cell membrane is achieved through protein conducting channels. The understanding of the working principles and configurations are of great relevance in today's biology. The central question of this chapter is the elucidation of the number of protein molecules which constitute a functional conducting channel. This issue has been addressed using a sequential bleaching technique, which forms an elegant method to simply 'count' the number of proteins in a single channel.

Finally, the fifth chapter discusses the issues and features behind the image formation process in a fluorescent micoscope. It represents an overview of how the light (photons) emitted by the light source is collected by the lens of the objective and, once caught by the detector, transformed into electronic images. Particular consideration has been devoted to the case where the light source is smaller than the wavelength of the emitted light (point-like source) alike a single fluorescent molecule. This subject is interesting because a detailed characterization and analysis of the image of a point-like source, the point spread function, can be used to overcome the optical resolution limit imposed by the diffraction of light, and as we show in the case of single molecule emitters, even to extract information on the orientation of the emitting molecule.

Samenvatting

Optische microscopie is van oudsher één van de meest toegepaste wetenschappelijke technieken. Sinds de uitvinding van de eerste microscoop aan het eind van de zestiende eeuw is microscopie daardoor immer doorontwikkeld, hand in hand groeiend en evoluerend met de wetenschap. Gedurende de laatste vijf eeuwen hebben wetenschappers, in diciplines variërend van biologie en geneeskunde tot natuurkunde en optica, enorm kunnen profiteren van de opmerkelijke mogelijkheden die de observatie van de natuur op kleine schaal met zich mee brengt. De eerste observatie van de complexe structuur van biologische systemen en van haar fundamentele bouwsteen, de cel, samen met de eerste experimenten aangaande de corpusculaire aard van materie, ofwel de observatie van Brownse beweging, kunnen zonder meer geschaard worden onder de meest opmerkelijke bevindingen gedaan met optische microscopen. Het streven om de gevoeligheid en resolutie van microscopen richting steeds kleinere lengteschalen te stuwen wordt gedreven door de vraag naar een immer gedetailleerder begrip van de microscopische wereld. Dit heeft in de loop der jaren tot een progressie van de mogelijkheden van microscopische technieken geleid, welke zelfs tot vandaag de dag doorzet.

Vijf eeuwen theoretische en technologische vooruitgang in microscopie hebben de moderne wetenschapper in staat gesteld om materie te bestuderen tot op het enkele-molecuul niveau. De enkele-molecuul en enkele-deeltjes microscopie technieken die de laatste 20 jaar zijn ontwikkeld, het onderwerp van deze dissertatie, hebben de toepassingen van optische microscopie verbreed naar nieuwe onderzoeksvelden, zoals de nanotechnologie en de materiaalwetenschap. Moderne enkele-molecuul microscopie stelt wetenschappers in staat om materie te bestuderen tot op de kleinste lengte schalen. Hoe enkele-molecuul gevoeligheid te bereiken is in een microscoop, hoe licht zich gedraagt wanneer het wordt uitgezonden door een enkel molecuul, en hoe het microscopische beeldvormingsproces plaatsvind zijn enkele kwesties die worden behandeld in deze dissertatie. Daarnaast wordt een aantal voorbeelden behandeld waarin de techniek wordt toegepast in het onderzoek naar diverse systemen in verschillende omstandigheden.

Hoofdstuk 2 is hoofdzakelijk gewijd aan de introductie en beschrijving van de meest gebruikte techniek in dit proefschrift, fluorescentiemicroscopie. Een technische beschrijving van de experimentele opstelling en de bijbehorende onderdelen (excitatiebron, optische elementen, detector, etc.) wordt gegeven,

alsmede een beschrijving van de software analyse van verkregen beelden, welke nodig is om een betekenisvolle interpretatie van de resultaten te kunnen doen.

Hoofdstuk 3 en 4 behandelen specifieke vraagstukken uit respectievelijk de nanotechnologie en de biologie. Hoofdstuk 3 introduceert en behandelt het zelfpropulsie-concept in micro- (10^{-6} m) en nanostructuren (10^{-9} m), een onderwerp waaraan meerdere onderzoeksgroepen werken, met als doel om materie en het transport van materie te kunnen sturen tot op de nanometerschaal. Hoewel zelfpropulsie reeds is bestudeerd en bereikt met objecten op een micrometer schaal, is het een ander verhaal op de nanometer schaal. Zelfpropulsie van nanodeeltjes in een vloeibare omgeving, gedreven door catalytische reacties, wordt sterk gehinderd, zoniet voorkomen door de enorme invloed van de Brownse kracht die wordt uitgeoefend op de deeltjes. Door het tracken van enkele-deeltjes is het mogelijk om de diffusieve beweging van nano-objecten te volgen. Aangezien de catalytische reacties plaatsvinden op het oppervlak van deze objecten, kunnen afwijkingen van puur Browns bewegingsgedrag direct gerelateerd worden aan de catalytische activiteit. Resultaten laten zien dat de nanodeeltjes strikt de Brownse diffusiewet volgen. Beargumenteerd wordt dat de homogene vrijlating van catalytische reactieproducten (zuurstof- en watermoleculen), door de geometrie of de functionalizatie van de nano-objecten, voorkomt dat een netto propulsie kracht ontstaat.

Hoofdstuk 4 snijdt een onopgeloste kwestie aan aangaande het geleidingskanaal van het zogenoemde SecYEG-eiwit. In elke levende cel is worden eiwitten zowel afgescheiden van, als ingevoegd in het celmembraan via eiwitgeleidingskanalen. Het begrijpen van de onderliggende mechanismen en the bijbehorende configuraties is zeer relevant in de moderne biologie. De kwestie die in dit hoofdstuk centraal staat is de opheldering van het aantal eiwitmoleculen dat een functionerend geleidingskanaal vormt. Dit vraagstuk wordt aangepakt door middel van een zogenaamde ‘sequential bleaching’ techniek, welke men in staat stelt om op elegante wijze het aantal eiwitmoleculen in een geleidingskanaal simpelweg te ‘tellen’.

Tenslotte worden in het vijfde hoofdstuk de specifieke details en karakteristieken van het beeldvormingsproces in een fluorescentiemicroscoop besproken. Dit hoofdstuk geeft een inzicht in hoe de photonen uitgezonden door een lichtbron worden verzameld door de lens van het microscoopobjectief, en, eenmaal opgevangen door de detector, hoe ze worden ‘vertaald’ in digitale beelden. De aandacht gaat in het bijzonder uit naar het geval waarin de lichtbron zelf kleiner is dan de golflengte van het uitgezonden licht (een zogenaamde puntvormige lichtbron of puntlichtbron), zoals in een enkel fluorescerend molecuul. Dit is een interessant onderwerp omdat een gedetailleerde karakterisatie en analyse van het beeld van een puntlichtbron, de zogenaamde puntspreidingsfunctie, kan worden gebruikt om de diffractielimiet voor optische resolutie te doorbreken. Bovendien kan men zodoende, zoals we laten zien voor het

geval van enkel-molecuul emissiebronnen, zelfs informatie aangaande de orientatie van de moleculen bemachtigen.

Acknowledgements

I spent more than 5 years in Groningen; first as student, working on my master thesis in the groups of Prof. Paul van Loosdrecht and Prof. Petra Rudolf, and afterwards as PhD candidate. It has been a long time and surely a very crucial period of my life.

Everything has started thanks to the precious opportunity offered me by both Petra and Paul to who I will always be thankful. The first time I entered the Zernike complex and visited the labs I thought: wow, this is a place where you can challenge your curiosity! As a result, I managed to stay around 4 years more. This was possible thanks to Paul, my boss and promotor of this thesis. Dear Paul, I still remember the conversation we had when you offered me the PhD position (and my dressing, clearly inappropriate for a job interview). As person and scientist you focus firstly on the real essence of matters and additionally on how they are presented or look like. Four and something years after that conversation, I here present my PhD thesis.

Some of the outcomes of my four years research are presented in the thesis and testify the fruitful collaboration I experienced, and greatly benefitted, with both my promotors Prof. Paul van Loosdrecht and Dr. Maxim Pchenichnikov. Dear Paul and Maxim, I am in debt with you to have shown and taught me a consistent and rigorous approach of doing scientific research. I feel privileged to have had the possibility of working with talented, curious, and consistent scientists. I largely experienced how much a partnership is affected by detailed and scrupulous planning, daily discussion, and a positive, but also critical, approach. I am aware that I still have a lot to learn, but the significant steps I have done mainly reflect your supervision.

I am also sincerely grateful to the members of my reading committee, Professors Johan Hofkens, Antoine van Oijen, and Jeff de Hosson. Thank you for the time you have dedicated to the manuscript which has surely improved by your evaluation and remarks. A special thank goes to Prof. Hofkens for the month I have spent working in his group at KU Leuven and for the fruitful discussions we had when visiting Groningen. I would like also to thank Prof. van Oijen for the numerous discussions boosting further the outcome of chapter 5. For me it is a pity you joined Groningen University only in 2010, but surely the present and future students will greatly benefit from your presence.

I am sincerely and deeply grateful to Dr. Victor Krasnikov who introduced me to modern fluorescence microscopy. Everything about basic microscopy I know is based on the vast and solid background you provided me. I enjoyed very much

your daily “in-field” supervision and our friendly chats. Surely I missed you after you left the group to join Antoine’s group. I am sure he and his collaborators have gained a lot with you and wish you to experience the same. Moreover, I owe you a great deal more. Being a smoker I know that once I will have to quit; thanks Victor to have shown me several times how to do it.

The Zernike Institute is a very international environment and I have appreciated and enjoyed the diversity and multicultural constituents of the Optical Condensed Matter Physics group. During the years I had the lucky chance to co-work and spend time with many colleagues that I would like to thank. A special place is reserved to the group’s technicians Ben Hesp and Foppe de Haan and in the first years Arjen Kamp. Ben, sharing the lab with you has been a very useful experience. Not only for the great knowledge and still surprising curiosity you posses for laser physics and technology, but also for showing me the bright side of the Dutch. As Italian, I have been always associated with the stereotype of a talking and singing person. Well, I will use you as example to support my quiet nature. I also will never forget how awesome your moustache was in the 70’s (60’s?).

Foppe, I do not know if in future I will be in the position of looking for or selecting people for a job. Well, if that will happen, consider yourself the first candidate. Whatever the topic, experiment, and problem I presented and discussed with you, surely soon afterwards I was receiving your software solution. Many thanks. It has been always very pleasant and supporting to have your around, particularly during the “hard-core Dutch sessions” at lunch time. Guys, thank you very much for everything, it has been a great pleasure and sincerely wish you all the best.

The first time I arrived in Groningen it was my first journey abroad. I did not just liked being in the Netherlands. I really loved and enjoyed it! This thanks to the numerous people I had the fortune to meet. It is with great pleasure that I approach this thanking session. Let’s start with my paranymphs, Tatiana and Fabrizio.

Dear Tati, we know each other since the very beginning of the Groningen period and I will always associate my good time here to you. You always have been a great friend both taking good care of me and, at the same time, challenging my health. Those who do not understand this point, they just never have been to a Tati-organizer Spanish community party. You are always organizing something with as many friends as possible. You have been the very special glue keeping together the broad international community of Groningen. I am proud of our friendship and I care it very much.

Fabbri`! What to say? On these days I am living with you, Sara and the kids for the third time in 5 years. Sincerely, I cannot come with any better example of very good and deep friendship than opening your own home. You guys have done it three times for me. It is difficult to explain how welcome I always felt, and truly part of an extended family. I have a special place in my heart for your two kids Giuseppe and Emma. I guess that if a four year old boy and a two year old girl calls your name 300 times in a single day that expresses feelings. Each single moment

spent with Sara and Bellicapelli is special, precious, and often funny. Un abbraccio e un grazie anche agli Evangelista de Roma: Franca, Vittorio e Francesca (abbellaaa, quando vuoi sono pronto per un massaggio).

Today, I call friends some of the people I met. The very first one, Daniele, was three days late. Only years later I discovered that his concept of "fashionable late" was three hours and I could finally get offended. The scientist responsible for the discovery of the Faustone, Daniele, not only helped me as colleague but mostly as friend. It was always a challenge to spend time with you and for that I thank my lucky star. Good luck with whatever your mind will suggest you. Fai il bravo. A special hug goes to Paolo, the bravest and most faithful person I ever met; wish you to change the world.

Alessio also played a very important role in my Groningen time. Though histrionic and fabulous dancer, he has decided to dedicate his life to science shadowing his outstanding sense of fashion and elegance. Though dangerous, I wish to have more dinners with you in future. Good luck and many kisses to Kristina.

Together with the people from the south I am glad to have had great time also with Tom. He has been for a long time my counterpart example, or example to imitate. I envy your scrupulously organized life, but also I am glad that Nuria is around you to screw up as much as possible your plans. I like Nuria for several reasons and I clearly see why you two match so well. Wish you all the best beers the US can provide. Ah!...almost forgotten…CHICKEN WIIIINSS!!

Within the Spanish community a mention of honour is reserved to Santi. You entered my heart far before singing Happy Birthday dressed in "white and blond" at my surprise party. I miss our time together in Groningen and anywhere else we have been. Stephanie take good care of him (and Santi of your "tedeschina"), and a generous slide of prosciutto crudo will always be waiting for you. When in Piacenza, you made me very proud.

Mariajose, among all the Spanish you look the most quiet, making of you the craziest. Time together has been always nice and funny, hopefully we will have more. A big hug goes to the beautiful Lumi wishing you to shine more and more.

Eleeeeee, probabilmente stai dormendo ora…ti mando un bacio gigante e un abbraccio.

To my good friend Dima and to Yulia, I miss you guys. I sincerely hope to visit you soon in Orlando. Dima you have been a very nice and intense friend to spend time with. I enjoyed very much our chatting and experience exchange on literature, music, movies, life, past and future, food, and vodka. Yulia is beautiful and among the most valuable persons I know, wish you to treasure your life together.

How to not mention the Dr. Bonny's family? Dear Cate, Francesco and Rosa though we met quite late, our dinners already entered in my "must do" list.

Un grande abbraccio anche per Marianna, la soul voice di Groningen e master dei golurgiones.

Un saluto e un abbraccio anche a Fabrizio, Milena e al nuovo arrivato Zeno. Gallo, ho sempre invidiato e invidio tuttora l' entusiasmo con cui affronti ogni esperienza, ti auguro di non perderlo mai. Cara Mina, aaahhhh se solo il gallo non fosse' cosi' sexy…un bacione gigante alla mia Mina favorita! Potete immaginare quanto io sia contento dell' arrivo di Zeno, vi auguro ogni bene. Mina stai pronta, se Zeno assomiglia a suo padre, sara' sempre in lotta con ragni e termosifoni.

I hate lists, but a kind voice is suggesting me I cannot write acknowledgements longer than the thesis itself. Therefore, I have to speed up. My apologies to all the friends following, if you are here it is because I have special memories with each of you. Here we go: Andrea, Andrija, Anton and Adriana, Arjen, Bas, Carol, the beautiful Jania and Cecile with Sofia and Anika, Damiano (sorry…Lord Galvan), Dimitry, Dimitrios (sexiest Professor in Greece), Jia, Gloria (my fantastic student, un bacio and good luck), Giulio e Carolina, Iljas, Itzel and Stefano, Jens, Jerome, my good friend Jesus (God bless you), a big kiss to Johanne, Kanat (my associate to a very noisy group), Luca (ricordati, dalle nostre parti teniamo sempre la schiena dritta), Manooolooo, Marcella, Maria Jesus, Milena, Mirian, Monika (ragazza!), Pablo, Primoz, Roberto and Michela, Ryota (Pokemon), Simon and Simone with Zoe and Finn, Simone (sono a dieta…ho bisogno di stuzzicare qualcosina con te, spero in Sicilia), the "bless of the world" Tano, and "i fantastici montanari" Tony and Tania.

The great time I had in Groningen did not shadow the attachment to my beloved Piacenza and the persons in there.

Un profondo grazie va alla mia famiglia: mamma, papa' e Michele. Se le esperienze hanno formato la persona che sono, gli strumenti con cui affrontarle vengono da voi. Anche se vivere lontani rattrista, il vostro supporto per ogni mia decisione non si e' mai affievolito. Grazie. Michele in bocca al lupo, costruire una vita in Italia e' dura al griorno d' oggi. Sono sicuro pero' che tu e Sara farete del vostro meglio e le soddisfazioni presto arriveranno. In ogni caso, puoi sempre contare su tuo fratello.

Un abbraccio va anche agli amici che sempre trovo quando torno, e che spero sempre di trovare. Penso al testone del Salva, che sempre mi coinvolge nelle sue innumerevoli attivita'e che mi tiene "affettuosamente" aggiornato sui menu' delle varie sagre. Un bacio gigante a Cristiana e al Teo; Cri mi raccomando col Salva sii paziente con i suoi hobby, gli rimane solo quello.

Un abbraccio agli amici di sempre Giangio, Gando e Simo. Giovani mi mancate. Da quando sono partito siete diventati tutti papa', ormai sono l' unico rimasto ancora senza prole. Un bacio e un abbraccio alle vostre famiglie: a Silvia e Alice, a Chiara e Emma, e a Sara con Tommaso e Matilde.

I will close my long acknowledgements with the most special thank to my Dorota. Pisolino, Groningen is just the beginning of our adventure together, I am excited by the journey is still in front of us. Remember; every time you smile you make me happy.

Filippo, July 2011, Groningen